Mathematisches Forschungsinstitut Oberwolfach

Report No. 18/2010

DOI: 10.4171/OWR/2010/18

Mathematics and Algorithms in Tomography

Organised by
Martin Burger, Münster
Alfred Louis, Saarbrücken
Todd Quinto, Medford

April 11th – April 17th, 2010

Abstract. This is the eighth Oberwolfach conference on the mathematics of tomography. Modalities represented at the workshop included X-ray tomography, sonar, radar, seismic imaging, ultrasound, electron microscopy, impedance imaging, photoacoustic tomography, elastography, vector tomography, and texture analysis.

Mathematics Subject Classification (2000): 65R32, 44A12, 92C55.

Introduction by the Organisers

This workshop included 46 researchers and graduate students from Europe, North America, and Asia. The participants represented a broad range of areas from pure mathematics to numerical analysis to medicine and industry. This interplay between pure mathematics and applications is one of the appeals of the field.

The first Oberwolfach tomography conference in 1980 helped define this young field, and the subsequent Oberwolfach workshops have reflected the growing breadth of the area. Modalities represented at this eighth conference include X-ray tomography, sonar, radar, seismic imaging, ultrasound, electron microscopy, impedance imaging, photoacoustic tomography, elastography, vector tomography, and texture analysis.

Frank Natterer, one of the pioneers in the field, started the conference by applying the Kaczmarz method to wave equation imaging in ultrasound. Ivana Jovanovic discussed ideas and algorithms in ultrasound, and Barbara Kaltenbacher analyzed convergence of Newton-Kaczmarz algorithms.

Local and limited data problems have been studied since the beginning of the field. Rolf Clackdoyle presented methods for two-dimensional region-of-interest

CT, and Samuli Siltanen presented his algorithm for x-ray tomography with very sparse data. Frederic Noo gave a reconstruction method for helical cone beam CT.

Esther Klann described a Mumford-Shah type level-set method to reconstruct and segment from SPECT/CT data, and Oliver Dorn spoke on reconstruction using level set methods.

Alexander Katsevich discussed his motion compensation algorithms for 2-D X-ray CT. Mohammad Dawood gave a motion correction method in 3D PET and CT, and Bernd Fischer described a motion correction algorithm for SPECT data.

Holger Kohr described his work using the approximate inverse in electron microscopy, and Todd Quinto analyzed a curvilinear Radon transform for large-field electron microscopy. Thomas Schuster presented work on vector tomography including diffraction and using an X-ray transform over geodesics.

Several types of tomography are modeled by circular or spherical integrals. Victor Palamodov developed a circular Radon transform for texture analysis on crystalline materials. Malte Spiess and Martin Riplinger spoke on an reconstruction method for stereology. Andreas Rieder presented a local reconstruction algorithm for spherical mean data, and Maarten de Hoop gave a multi-scale approach for seismology, and he showed reconstructions of the earth's crust.

Guillaume Bal described his work on inverse transport and photoacoustics and John Schotland presented related results on inverse transport with large data sets. Leonid Kunyansky discussed his algorithm in acousto-electric tomography, and Otmar Scherzer described his work to correct for attenuation in photoacoustic tomography. Aref Lakhal provided an imaging method for Maxwell's equation.

Martin Hanke described his algorithm for backscattering data in impedance tomography, and Bastian Harrach gave his linearization method for impedance tomography. Peter Maass presented his work on impedance tomography with sparsity constraints.

Ming Jiang gave a phase unwrapping algorithm in phase contrast imaging, SAR, and MRI. Joyce McLaughlin discussed recent advances and challenges for elastography imaging. Pierre Sabatier discussed the meaning of mathematical ideas, such as uniqueness, closeness, and well-posedness, in physical inverse problems.

Summing up, tomography is a lively branch of science with an inexhaustible supply of mathematical problems. Every new imaging modality poses new mathematical questions, and this conference can be viewed as a snapshot of this lively field.

We thank Prof. Dr. Greuel and the staff of the Mathematiches Forschungsinstitut Oberwolfach for creating a stimulating environment to do serious mathematics. For seven participants, that hospitality extended for several days beyond the end of the conference when European airspace was closed by an ash cloud from an Icelandic volcano. Those participants are grateful to the MFO staff for making the time pleasant and productive. The organizers thank the MFO for their support of young mathematicians through E.U. and U.S. National Science Foundation grants.

Workshop: Mathematics and Algorithms in Tomography

Table of Contents

Abstracts

Kaczmarz' Method in Wave Equation Imaging

Frank Natterer

We consider the inverse problem of the wave equation for a special geometry, well suited for applications to medicine and seismic imaging. The object to be reconstructed lies between two parallel horizontal lines in R^2. The sources are sitting on the top plane. In the transmission mode the receivers are on the bottom line, while in the reflection mode the receivers are also on the top line. From the measurements $g(r,t) = (R_s(f))(r,t) = u(r,t), 0 < t < T$ of the pressure field u at the receivers r for each source s we want to determine the speed of sound $c(x)$ for each point x between the parallel lines. We assume that u satisfies the wave equation with the speed of sound $c = c_0/sqrt(1+f)$ with c_0 the background speed, i.e. we want to determine the function f.

We model the source at point s in the top line by the boundary condition

$$\frac{\partial u}{\partial x_2}(x,t) = q(t)p(x-s). \tag{1}$$

q is the source pulse. The frequency content of q is of the utmost importance. We assume that the Fourier transform $\hat{q}$ of q is significantly non-zero between ω_{min} and ω_{max}. Then it can be shown [1] that, in the Born approximation, the Fourier transform $\hat{f}$ is determined by the data in the union of the circles of radius $k_{max} = \omega_{max}/c_0$ around the points $(\pm k_{max}, 0)$ in transmission mode and outside the circles W with radius $k_{min} = \omega_{min}/c_0$ around $(\pm k_{min}, 0)$ in the reflection mode. In particular it is clear that if q doesn't have low frequencies, i.e. if $\omega_{min} > 0$, low frequency features of f cannot be recovered in reflection mode.

The Kaczmarz method is an iterative method with update

$$f \leftarrow f + \alpha(R_s'(f))^*(g - R_s(f)). \tag{2}$$

The adjoint operator $(R_s(f))^*$ can be evaluated by time reversal, i.e. by solving the wave equation backwards in time, with the residual $g - R_s(f)$ as boundary values at the receivers.

In the talk we study the performance of the Kaczmarz method. In the transmission mode all we have to do to get convergence is to make sure that the initial approximation f_0 satisfies the condition

$$|\int (f - f_0)ds| \leq \lambda \tag{3}$$

where $\lambda = 2\pi/k_{max}$ is the smallest wavelength contained in the pulse q. An early reference to results of this type is [2]. If this condition is not satisfied one can get convergence by filtering out the high frequencies from the data and doing a preliminary reconstruction.

In the reflection mode we in addition have a condition on the lowest frequency ω_{min} in q. This condition is obtained by securing stability in the analytic continuation process that fills the missing circles W in the Fourier plane. It is shown that this stability is governed by the factor $1/(1-\rho)$ where ρ is the largest eigenvalue of the integral operator with kernel $K(x-y)$,

$$K(x) = \frac{1}{\pi} cos(k_{min} x_1) \frac{J_1(k_{min}|x|)}{k_{min}|x|}, \tag{4}$$

in the space $L_2(|x| < r)$, $|x| < r$ being the support of f. ρ obviously depends on rk_{min} only, which is just the object diameter expressed in wavelengths. Typical values for ρ are 0.588 and 0.968 for $rk_{min} = \pi/2, \pi$, respectively. This means that only objects whose size corresponds to a typical wavelength can be recovered. We show by numerical examples that the Kaczmarz method in fact recovers objects of this size.

References

[1] Natterer, F.: Ultrasound tomography with fixed arrays of transducers, Proceedings of the Interdisciplinary Workshop on Mathematical Methods in Biomedical Imaging and Intensity-Modulated Radiation Therapy (IMRT), Pisa, Italy, October 2007.

[2] Mora, P.: Inversion = migration + tomography, Geophysics 54,1575-1586 (1989).

Newton type Kaczmarz Methods

Barbara Kaltenbacher

(joint work with Martin Burger, Hans Baumeister, Antonio Leitão)

Many problems in tomography can be formulated as a system of nonlinear operator equations

$$F_i(x) = y_i\,, \quad i = 0, \dots, N-1\,,$$

with possibly noisy data satisfying

$$\|y_i^\delta - y_i\| \le \delta\,, \quad i = 0, \dots, N-1\,,$$

where, e.g. x is a coefficient in a PDE, and $\mathbf{F}(x) = (F_0(x), \dots, F_{N-1}(x)) \dots$ the discrete Dirichlet-to Neumann map. Kaczmarz methods (closely related to the well-known algebraic reconstruction technique) perform a cyclic iteration over these subproblems, see, e.g., [7], [10] One of the key advantages over this successive instead of simultaneous kind of iterative solution strategy is that storage and computational treatment is only required for several smaller subproblems $F_i(x) = y_i$ instead of one large problem $\mathbf{F}(x) = \mathbf{y}$. Moreover, Kaczmarz methods are particularly easy to implement especially if the F_i are similar, thus in many tomographic problems. After a short review on convergence results for gradient type (Landweber) Kazcmarz methods ([9], [4]), we dwell on cyclic Newton type iterative schemes. In the context of ill-posedness and regularization, manly two approaches can be found in the single operator case: The Levenberg-Marquardt method (LM, [5], [11]) and the Iteratively Regularized Gauss Newton Method

(IRGNM, [1], [8], [6]). For both of them the convergence analysis can to some extent be carried over to the respective Kaczmarz version:

The LM-Kaczmarz method reads as

$$x^\delta_{k+1} \;=\; x^\delta_k + (F'_{[k]}(x^\delta_k)^* F'_{[k]}(x^\delta_k) + \alpha_k I)^{-1} F'_{[k]}(x^\delta_k)^* (y^\delta_{[k]} - F_{[k]}(x^\delta_k))$$

where

$$[k] := k \mathrm{mod} N$$

and requires a proper selection of the regularization parameter α_k in each step. Adopting the inexact Newton choice for the single equation case according to [5], one can prove monotone decay of the error and square summability of the residuals, however, convergence possibly gets lost. By simply setting $\alpha_k \equiv \alpha$ constant, convergence can be show. For the practically relevant situation of noisy data, a loping strategy from [4] can be applied and, together with the discrepancy principle as an overall stopping rule, yields convergence as the noise level tends to zero, see [2]. As in the single equation case, closeness of the strating value to a solution as well as restrictions on the nonlinearity are needed such as the following analog of the Scherzer condition

$$\|F_i(\tilde{x}) - F_i(x) - F'_i(x)(\tilde{x} - x)\| \le \eta \|F_i(\tilde{x}) - F_i(x)\|\,, \quad \forall i \in \{0, \dots, N-1\}, x \in \mathcal{B}_\rho(x_0)\,.$$

For the IRGNM-Kazcmarz method

$$x^\delta_{k+1} = x_{0,[k]} - G_{\alpha_k}(F'_{[k]}(x^\delta_k))(F_{[k]}(x^\delta_k) - y^\delta_{[k]} - F'_{[k]}(x^\delta_k)(x^\delta_k - x_{0,[k]}))$$

the simple a priori choice $\alpha_k = \alpha_0 q^k$, $q \in (0,1)$ yields convergence provided the initial guesses satisfy $x_{0,i} - x^* \in \mathcal{N}(F'_i(x^*))^\perp$. The latter condition appears to be the price one has to pay for some additional freedom that the IRGNM-Kazcmarz method offers as far as the nonlinearity of the forward operator is concerned. Namely, in place of the Scherzer condition, the analysis works with local range invariance of each of the $F'_i(x)$, which turns out to be realistic for several tomography type problems such as reconstruction from Dirichlet-Neumann pairs, reconstruction from multiple sources SPECT, or ultrasound tomography: These can be written as the composition of a linear ill-posed with a nonlinear well-posed operator (with Lipschitz continuous derivative) and therefore satisfy local range invariance, see [3].

Future research will be devoted to an analysis of Kaczmarz methods in Banach spaces, motivated by the fact that in tomography often natural choices of the preimage and image space do not have Hilbert space structure,

References

[1] A.B. Bakushinskii, *The Problem of the convergence of the iteratively regularized Gauss–Newton method*, Comput.Math.Math.Phys. 32 (1992), 1353–1359.

[2] J. Baumeister, B. Kaltenbacher, and A.Leitão, *On Levenberg-Marquardt-Kaczmarz iterative methods for solving systems of nonlinear ill-posed equations*, Inverse problems and imaging (IPI), to appear, 2010.

[3] M. Burger and B. Kaltenbacher, *Regularizing Newton-Kaczmarz methods for nonlinear ill-posed problems*, SIAM J.Numer.Anal., **44** (2006), 153-182.

[4] M. Haltmeier, A. Leitão, and O. Scherzer *Kaczmarz methods for regularizing nonlinear ill-posed equations I: convergence analysis*, Inverse Problems and Imaging **1** (2007), 289-298.
[5] M. Hanke, *A regularization Levenberg–Marquardt scheme, with applications to inverse groundwater filtration problems*, Inverse Problems 13 (1997), 79–95.
[6] T. Hohage: *Regularization of exponentially ill-posed problems*, Numer. Funct. Anal. Optim. **21** (2000), 439–464.
[7] S. Kaczmarz, Approximate solution of systems of linear equations, Internat. J. Control, 57 (1993), 12691271,
[8] B. Kaltenbacher, A. Neubauer, O. Scherzer: *Iterative Regularization Methods for Nonlinear Ill-Posed Problems*. Walter de Gruyter, Berlin – New York, 2008.
[9] R. Kowar, O. Scherzer, *Convergence analysis of a Landweber-Kaczmarz method for solving nonlinear ill-posed problems*, in: S. Romanov, S.I. Kabanikhin, Y.E. Anikonov, A.L. Bukhgein, *Ill-Posed and Inverse Problems*, VSP Publishers, Zeist, 2002.
[10] F. Natterer: Algorithms in Tomography, in: Duff, I.S. - Watson, G.A. (eds.): The State of the Art in Numerical Analysis. Clarendon Press 1997.
[11] A. Rieder, *On the regularization of nonlinear ill-posed problems via inexact Newton methods*, Inverse Problems 15 (1999), 309-327.

A novel method for fast and high-quality reconstructions in Electron Tomography

Holger Kohr

In Electon Tomography (ET), a specimen is exposed to high-energy electrons (modeled as plane waves) which are scattered by the electrostatic potential of the object, pass the optical system of the microscope and are finally detected by a digital camera. In the most general setting, this process can be described as scalar potential scattering, followed by a series of transformations and propagations of the scattered wavefield. In the case of biological applications covered here, the contrast of a typical electrostatic potential is low enough such that the problem can be linearized on the one hand by applying the Born approximation to the scattered wave, and on the other by linearizing the measured intensity at the detector. By replacing the circular wavefronts in the propagation steps by a parabolic appoximation, one acquires the linear forward model

$$g_\omega = \mathcal{D}^M \mathcal{C}_\sigma \mathcal{P}_\omega f$$

for the formation of a single image g_ω [1]. The quantities and operators appearing in this equation are as follows:

Phase contrast function $f : \mathbb{R}^3 \to \mathbb{R}$:
Represents the phase modulation of an incoming wave by the specimen. In order to achieve uniqueness, the amplitude contrast function is supposed to be the σ-fold multiple of the real part [1]. For the tested datasets, the value of $\sigma = 0.2$ was found to be an appropriate choice.

X-ray transform $\mathcal{P}_\omega : L^2(\mathbb{R}^3) \to L^2(\omega^\perp)$:
For a fixed direction $\omega \in \mathcal{S}^2$, $\mathcal{P}_\omega$ is defined as

$$\mathcal{P}_\omega f(\eta) = \int_{\mathbb{R}} f(t\omega + \eta)\,\mathrm{d}t, \quad \eta \in \omega^\perp.$$

In the current application, this operator can be regarded as a projection of the object to the normal plane $\omega^\perp$, every point of which acts as a secondary source of a circular wave.

Convolution $\mathcal{C}_\sigma : L^2(\omega^\perp) \to L^2(\omega^\perp)$:

The propagation of the aforementioned secondary waves and the transformation introduced by the optics of the microscope are gathered in the convolution

$$\mathcal{C}_\sigma u(\eta) = \int_{\omega^\perp} K_\sigma(\eta - \xi)\, u(\xi)\, \mathrm{d}\xi,$$

where the Fourier transform of K_σ, the so-called *charge transfer function*, is an oscillating and exponentially decaying function [2].

Dilation $\mathcal{D}^M : L^2(\omega^\perp) \to L^2(\omega^\perp)$:

The actual purpose of the optics is a magnification of the projection image. Mathematically, this operation is described by the M-fold dilation

$$\mathcal{D}^M u(\eta) = M^{-1}\, u(M^{-1}\eta).$$

In the case of single-axis tilting, the optical axis ω varies on the partial great circle

$$\mathcal{S}^2_* := \big\{ \big(0, \sin\theta, \cos\theta\big) \,\big|\, \theta \in [-\theta_0, \theta_0] \,\big\}.$$

This leads to the description of a full measurement series as a function given on the **tangent bundle**

$$\mathscr{T} := \big\{ (\omega, \eta) \,\big|\, \omega \in \mathcal{S}^2_*\,,\ \eta \in \omega^\perp \,\big\}.$$

By defining the X-ray transform $\mathcal{P}_\omega : L^2(\Omega) \to L^2(\omega^\perp)$ with variable direction as

$$\mathcal{P} f(\omega, \eta) := \int_{\mathbb{R}} f(t\omega + \eta)\, \mathrm{d}t, \quad \omega \in \mathcal{S}^2_*,\ \eta \in \omega^\perp,$$

the inverse problem addressed in this context can be expressed as the following task:

Reconstruct the function values $f(x)$ from the dataset g modeled by

$$g(\omega, \eta) = \mathcal{D}^M \mathcal{C}_\sigma \mathcal{P} f(\omega, \eta) := \mathcal{A}_\sigma f(\omega, \eta).$$

The standard algorithm to solve this inverse problem in ET is the so-called *weighted backprojection* (WBP) which is a modification of the filtered backprojection accounting for some attenuation [5]. The method presented here is based on the **Approximate Inverse** approach [3] which consists in the computation of a smoothed version

$$f_\gamma(x) = \langle f,\, E_\gamma(x, \cdot) \rangle_{L^2(\mathbb{R}^3)} = \int_{\mathbb{R}^3} f(y) E_\gamma(x, y)\, \mathrm{d}y$$

with the help of a solution $\Psi_\gamma : \mathbb{R}^3 \to L^2(\mathscr{T})$ of the auxiliary equation

$$\mathcal{A}^*_\sigma \Psi_\gamma(x) = E_\gamma(x, \cdot).$$

The function E_γ is called **mollifier**, whereas Ψ_γ is usually refeered to as **reconstruction kernel**. The application of a mollifier *of convolution type* $E_\gamma(x, y) =$

$e_\gamma(x-y)$, the pointwise solution of the auxiliary equation can be reduced to the solution of

$$\mathcal{A}_\sigma^* \psi_\gamma = e_\gamma,$$

since the reconstruction kernel inherits the convolution structure:

$$\Psi_\gamma(x)(\omega,\eta) = \psi_\gamma(MP_{\omega^\perp}x - \eta).$$

For a separated mollifier $e_\gamma(x) = e_\gamma^1(x_1)\,\tilde{e}_\gamma(\tilde{x}),\ \tilde{x} = (x_2, x_3)$, it can be shown that an approximation to the reconstruction kernel is given by

$$\mathcal{F}_2\psi_\gamma(\omega,\xi) = \frac{M}{2\sqrt{2\pi}}\,\underbrace{T_\sigma^\dagger(M\xi)}\,\underbrace{\mathcal{F}_1 e_\gamma^1(M\xi_1)}\,\underbrace{|M\tilde{\xi}|\mathcal{F}_2\,\widetilde{e}_\gamma(M\tilde{\xi})}$$

in Fourier space, where the subscript of the Fourier transform $\mathcal{F}$ denotes its dimensionality. The first underbraced factor is responsible for the deconvolution step and depends on both image coordinates, whereas the other two factors exhibit the same separated structure as the mollifier. Apparently, only the $\tilde{\xi}$ direction is affected by the X-ray transform, which is indicated by the ramp filter.
The actual reconstruction formula for the approximation f_γ is given by

$$f_\gamma(x) = \int_{\mathcal{S}_*^2} (g * \psi_\gamma)(\omega, MP_{\omega^\perp}x)\,\mathrm{d}\omega,$$

which is clearly of filtered backprojection type. The major difference between other FBP type methods and this one is the inversion of the convolution, which requires a smoothing not only in the direction $\tilde{\xi}$ where the X-ray transform acts, but also in the perpendicular direction ξ_1, due to the singular term $T_\sigma^\dagger$ depending on both coordinates.
Numerical experiments with measured data show that the presented method is clearly superior to the standard WBP in terms of both noise suppression and richness of detail (Figure 1).

References

[1] D. Fanelli and O. Öktem. Electron tomography: a short overview with an emphasis on the absorption potential model for the forward problem. *Inverse Problems*, 24(1):013001, 2008.

[2] P. W. Hawkes and E. Kasper. *Principles of electron optics. Volume 3: Wave Optics*. Academic Press, 1994.

[3] A. K. Louis and P. Maass. A mollifier method for linear operator equations of the first kind. *Inverse Problems*, 6:427–440, 1990.

[4] O. Medalia et al. Organization of actin networks in intact filopodia. *Current Biology*, 17(1):79–84, 2007.

[5] M. Radermacher. Weighted back-projection methods. In J. Frank, editor, *Electron Tomography - Methods for Three-Dimensional Visualization of Structures in the Cell*. Springer, 2nd edition, 2006.

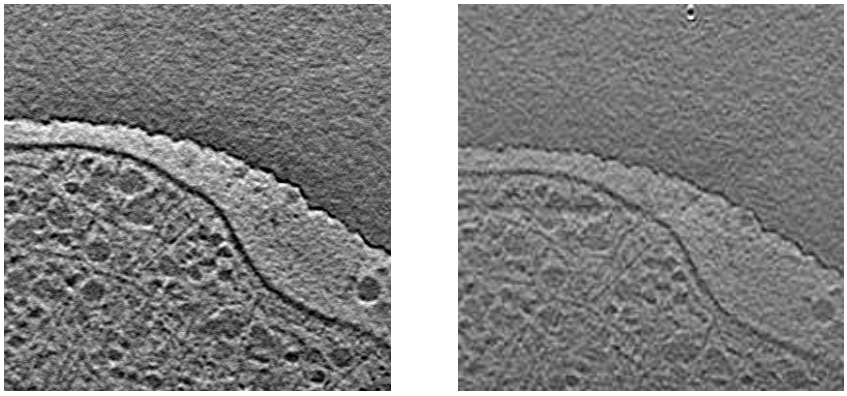

FIGURE 1. Slice through the reconstruction of a phase contrast function. The reconstructed volume contains the exterior region of a cell, where the small string-like *actin filaments* are of special interest. Left image: reconstruction computed by the approximate inverse with Gaussian mollifier and $\gamma = 7 \cdot 10^{-10}$. Right image: the same slice in the WBP reconstruction. The noise level in the left image is substantially lower than in the right one, while the details are preserved. Courtesy of Ohad Medalia, Martinsried [4].

2D vector field tomography taking refraction into account

THOMAS SCHUSTER
(joint work with Tim Pfitzenreiter)

The aim of 2D vector field tomography is the reconstruction of the velocity field $\boldsymbol{u}(x) = \boldsymbol{u}(x_1, x_2)$ of a moving fluid in a bounded, convex domain $\Omega \subset \mathbb{R}^2$ from ultrasound time-of-flight measurements. We assume that Ω has an inhomogeneous background given by a variable sound velocity $c(x)$ for $x \in \Omega$ and that $c = c_0$ is constant in the exterior $\mathbb{R}^2 \backslash \Omega$. The time a signal needs for travelling from a source point $a \in \partial\Omega$ to a detector $b \in \partial\Omega$ is given as

$$t(a,b) = \int_{L(a,b)} \frac{\mathrm{d}\sigma(x)}{c(x) + \langle \boldsymbol{u}(x), \tau_L \rangle},$$

where $L(a,b)$ denotes the line connecting a and b, τ_L is the vector of direction of $L(a,b)$ and $\mathrm{d}\sigma$ means the segment of length along $L(a,b)$. A linearization yields

$$t(a,b) = \int_{L(a,b)} \frac{1}{c(x)} - \frac{\langle \boldsymbol{u}(x), \tau_L \rangle}{c^2(x)} \, \mathrm{d}\sigma(x) + \text{h.o.t.} \tag{1}$$

which is a good approximation when $|\boldsymbol{u}|/c \ll 1$, a reasonable assumption in many applications. Denoting by $n(x) = c_0/c(x)$ the index of refraction, then from (1)

follows that

$$t(a,b) + t(b,a) = \frac{2}{c_0} \int_{L(a,b)} n(x)\, \mathrm{d}\sigma(x) = \frac{2}{c_0} \mathfrak{R}[n](a,b) \tag{2}$$

$$t(a,b) - t(b,a) = -\int_{L(a,b)} \frac{\langle \boldsymbol{u}(x), \tau_L \rangle}{c^2(x)}\, \mathrm{d}\sigma(x) = -\frac{1}{c_0^2} \mathfrak{D}[n^2 \boldsymbol{u}](a,b) \tag{3}$$

Here $\mathfrak{R}[f](a,b)$ denotes the 2D Radon transform of a scalar function f along the line $L(a,b)$ and $\mathfrak{D}[\boldsymbol{f}](a,b)$ is the 2D Doppler transform

$$\mathfrak{D}[\boldsymbol{u}](a,b) = \int_{L(a,b)} \langle \boldsymbol{u}(x), \tau_L \rangle\, \mathrm{d}\sigma(x)\,.$$

It is known, compare e.g. Norton [2], that only $\operatorname{curl} \boldsymbol{u}$ can be recovered from $\mathfrak{D}[\boldsymbol{u}]$. The idea to do this is first computing $n(x)$ from (2) by inverting $\mathfrak{R}$ followed by reconstructing $\operatorname{curl} \boldsymbol{u}$ from (3) by filtered backprojection, see e.g. Schuster [4]. Doing so we would completely neglect any refraction of the ultrasound beams. But if the index of refraction $n(x)$ siginificantly differs from 1 depending on x, then refraction can not be neglected. According to Fermat's principle the ultrasound beams follow geodesic lines of the Riemannian metric

$$\mathrm{d}s^2 = n^2(x)(\mathrm{d}x_1^2 + \mathrm{d}x_2^2)\,. \tag{4}$$

Thus if the index of refraction $n(x)$ is assumed to be known from (2), then Fermat's principle inspires to consider the longitudinal ray transform on the Riemannian manifold $\mathcal{M} = (\Omega, \mathrm{d}s)$

$$\mathfrak{I}[\boldsymbol{u}](\varphi, s) = \int_0^{\tau_{\varphi,s}} \langle \boldsymbol{u}(\gamma_{\varphi,s}(t)), \dot{\gamma}_{\varphi,s}(t) \rangle\, \mathrm{d}t\,, \qquad \varphi \in [0, 2\pi]\,,\ s \in \mathbb{R}\,.$$

Here, $\gamma_{\varphi,s} : [0, \tau_{\varphi,s}] \to \Omega$ is a parametrization of the geodesic curve of the Riemannian metric (4) satisfying $\gamma_{\varphi,s}(0) = a = r\omega(\alpha)$ with $r \geq \operatorname{diam}(\Omega)/2$, $\dot{\gamma}_{\varphi,s}(0) = \omega(\varphi)^\perp$, where $\omega(\varphi) = (\cos\varphi, \sin\varphi)^t \in S^1$, $s = \operatorname{dist}(\{a + t\omega(\varphi)^\perp : t \in \mathbb{R}\}, 0)$ and $\tau_{\varphi,s}$ is chosen such that $\gamma_{\varphi,s}(\tau_{\varphi,s}) = b$. The transversal ray transform for vector fields on $\mathcal{M}$ is given as

$$\mathfrak{I}^\perp[\boldsymbol{u}](\varphi, s) = \int_0^{\tau_{\varphi,s}} \langle \boldsymbol{u}(\gamma_{\varphi,s}(t)), \dot{\gamma}^\perp_{\varphi,s}(t) \rangle\, \mathrm{d}t\,, \qquad \varphi \in [0, 2\pi]\,,\ s \in \mathbb{R}\,.$$

and is necessary to get the divergence of $\boldsymbol{u}$. The parametrization is illustrated in Figure 1 for $\Omega = \{x \in \mathbb{R}^2 : |x| < 1\}$. We assume that the metric (4) being simple and dissipative and that there are no caustics. In that case the matrix $(\partial_t \gamma_{\varphi,s}(t), \partial_s \gamma_{\varphi,s}(t))$ is regular and there exists a real phase function $\phi : \Omega \times (\mathbb{R}^2 \backslash \{0\}) \to \mathbb{R}$, that is a $\mathcal{C}^\infty$-function satisfying $\phi(x, \lambda\theta) = \lambda\phi(x,\theta)$, $\nabla_x \phi(x,\theta) \neq 0$ and

$$h(x,\theta) := \det\Big(\frac{\partial^2 \phi}{\partial x \partial \theta}(x,\theta)\Big) > 0$$

such that

$$x = \gamma_{\varphi,s}(t) \quad \Leftrightarrow \quad \phi(\gamma_{\varphi,s}(t), \omega(\varphi)) = s\,.$$

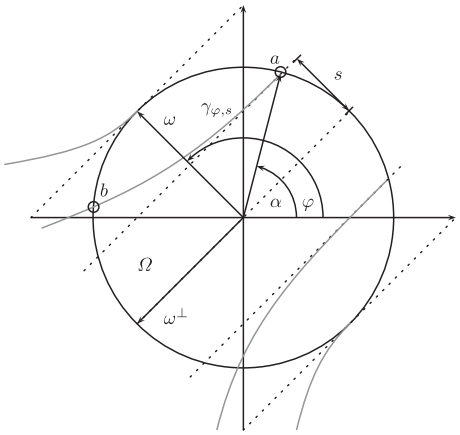

FIGURE 1. Definition of the parameters for $\mathfrak{I}[\boldsymbol{u}](\varphi, s)$; the geodesics $\gamma_{\varphi,s}$ are depicted in grayscale.

In case of ds being the Euclidean metric, that means $n(x) = 1$, the geodesic curves are straight lines and $\phi(x, \theta) = \langle x, \theta \rangle_2$. With the help of phase functions the generalized Radon transform along geodesics of (4) can simply defined as

$$\mathfrak{R}_a[f](\varphi, s) = \int_{\phi(x,\omega(\varphi))=s} f(x) a(x, \omega(\varphi)) \, \mathrm{d}x \,,$$

where $f \in L^2(\mathcal{M})$ and $a \in L^2(\mathcal{M} \times S^1)$. Associated with $\mathfrak{R}_a$ is the weighted dual Radon transform

$$\mathfrak{R}_b^*[w](x) = \int_0^{2\pi} b(x, \omega(\varphi)) w(\varphi, s)_{|_{s=\phi(x,\omega(\varphi))}} \, \mathrm{d}\varphi$$

for $b \in L^2(\mathcal{M} \times S^1)$, $w \in L^2([0, 2\pi] \times \mathbb{R})$. The following theorem was proven by Beylkin in [1] and is fundamental for our inversion method.

Theorem: (Beylkin 1984 [1])
Let $U(s) \in \mathcal{C}^\infty(\mathbb{R})$ with $U(s) = U(-s)$ and $|\partial_s^k U(s)| \leq C(k)(1+s^2)^{(m-k)/2}$, $k \in \mathbb{N}$. Further let F be a Fourier integral operator

$$F[f](y) := \frac{1}{(2\pi)^2} \int_{\mathbb{R}^2} \int_{\Omega \subset \mathbb{R}^2} \mathrm{e}^{\mathrm{i}[\Phi(x,\theta) - \Phi(y,\theta)]} A(x, y, \theta) f(x) \, \mathrm{d}^2 x \, \mathrm{d}^2 \theta$$

with phase function

$$\Phi(\cdot, \theta) := \|\theta\|_2 \, \phi(\cdot, \arctan(\theta_1/\theta_2))$$

and amplitude $A(x, y, \omega) := b(y, \omega) a(x, \omega) U(\|\omega\|_2)$, where $b(y, \omega) \in \mathcal{C}^\infty(\Omega \times S^1)$ with $b(y, \omega) = b(y, -\omega)$. Then, $\mathfrak{R}_b^*(K *_s \mathfrak{R}_a)$ is a Fourier integral operator F, that

is

$$\mathfrak{R}_b^*(K *_s \mathfrak{R}_a)[f] = \frac{1}{(2\pi)^2} \int_{\mathbb{R}^2} \int_{\Omega \subset \mathbb{R}^2} \mathrm{e}^{\mathrm{i}[\Phi(x,\omega)-\Phi(y,\omega)]} A(x,y,\omega) f(x)\, \mathrm{d}^2x\, \mathrm{d}^2\omega$$

$$=: F[f]\,, \qquad f \in L^2(\Omega)\,, \tag{5}$$

where

$$K(s) = \frac{1}{2(2\pi)^2} \int_{-\infty}^{\infty} |r|\, U(r) \mathrm{e}^{\mathrm{i}\, rs}\, \mathrm{d}r$$

Moreover if particularly

$$b(y,\omega) = \frac{h(y,\omega)}{a(y,\omega)}$$

and $U(\|\omega\|) = 1$ for all $\omega \in S^1$, then the Fourier integral operator $\mathfrak{R}_b^*(K *_s \mathfrak{R}_a)$ has a representation

$$\mathfrak{R}_b^*(K *_s \mathfrak{R}_a) = F = \mathrm{id} + T\,, \tag{6}$$

where $T : L^2(\Omega) \to L^2_{\mathrm{loc}}(\Omega)$ is a compact operator with an asymptotic expansion of the form

$$T = \sum_{l=1}^{\infty} \sum_{m=0}^{l} T_l^m\,. \tag{7}$$

The next ingredient of our reconstruction scheme is the following connection of the longitudinal and transversal ray transform for vector fields on $\mathcal{M}$ and the attenuated Radon transform $\mathfrak{R}_a$. The proof relies on Stoke's theorem and can be found in [3].

Theorem: Let $\Omega \subset \mathbb{R}^2$ be an open, bounded and convex domain, $\mathcal{M} = (\Omega, g)$ be a Riemannian manifold with metric tensor $g_{ij} = n^2(x)\delta_{ij}$ and $\boldsymbol{u} = (v^1, v^2)^{\mathrm{T}} \in \mathcal{C}^1(\Omega)^2$ be a vector field with $\boldsymbol{u} = 0$ on $\mathbb{R}^2 \backslash \Omega$. Furthermore assume that $\{\gamma_{\varphi,s} : [\tau_{\varphi,s}, 0] \to \mathcal{M} : s \in [-r, r]\,,\ \varphi \in [0, 2\pi]\}$ is a family of geodesic curves corresponding to the metric tensor g on $\mathcal{M}$ such that the Jacobian

$$J(s,\tau) := (\partial_s \gamma_{\varphi,s}(\tau), \partial_\tau \gamma_{\varphi,s}(\tau))$$

exists and is continuous on $[-r, r] \times [0, 2\pi]$, where $r := \mathrm{diam}(\Omega)/2$. Then,

$$\frac{\partial}{\partial s} \mathfrak{I}[\boldsymbol{u}](s,\varphi) = \mathfrak{R}_a[(\mathrm{curl}\, \boldsymbol{u})](s,\varphi)$$

$$\frac{\partial}{\partial s} \mathfrak{I}^{\perp}[\boldsymbol{u}](s,\varphi) = \mathfrak{R}_a[(\mathrm{div}\, \boldsymbol{u})](s,\varphi)$$

with $s \in \mathbb{R}$, $a = |\det J|$ and $\varphi \in [0, 2\pi]$ holds.

Neglecting the compact operator T in the identity (6) we obtain an asymptotic inversion method of filtered backprojection type to recover $\mathrm{curl}\, \boldsymbol{u}$ and $\mathrm{div}\, \boldsymbol{u}$ from $\mathfrak{I}[\boldsymbol{u}]$ and $\mathfrak{I}^{\perp}[\boldsymbol{u}]$, respectively.

Corollary: Neglecting the compact operator T in the identity $\mathfrak{R}_b^*(K *_s \mathfrak{R}_a) = \mathrm{id} + T$ the asymptotic reconstruction formulas read

$$\operatorname{curl} \boldsymbol{u} = \mathfrak{R}_b^* \left(K *_s \frac{\partial}{\partial s} \mathfrak{J}[\boldsymbol{u}] \right) \tag{8}$$

$$\operatorname{div} \boldsymbol{u} = \mathfrak{R}_b^* \left(K *_s \frac{\partial}{\partial s} \mathfrak{J}^{\perp}[\boldsymbol{u}] \right) . \tag{9}$$

References

[1] G. Beylkin, *The inversion and application of the generalized Radon transform*, Commun. Pure Appl. Math., **37** (1984), 579–599.

[2] S.J. Norton, *Tomographic reconstruction of 2-D vector fields: application to flow imaging*, Geophys. J., **97** (1988), 161–168.

[3] T. Pfitzenreiter and T. Schuster, *Tomographic reconstruction of the curl and the divergence of 2D vector fields taking refractions into account*, SIAM J. Imag. Sci., (2010), submitted.

[4] T. Schuster, *An efficient mollifier method for three-dimensional vector tomography: convergence analysis and implementation*, Inverse Problems, **17** (2001), 739–766.

Inverse Problem of Acousto-Optic Imaging

John C. Schotland

(joint work with Guillaume Bal)

The acousto-optic effect is a phenomenon in which the optical properties of a material medium are modified due to interaction with acoustic radiation. Brillouin scattering from density fluctuations in a fluid [1] or the ultrasonic modulation of multiply-scattered light in a random medium [2] are familiar examples of this effect. It is well known that the scattered optical field carries information about the medium. This principle has been exploited to develop a hybrid imaging modality, known as acousto-optic imaging (AOI), which combines the spectroscopic sensitivity of optical methods with the spatial resolution of ultrasonic imaging [3, 4, 5, 6, 7, 8, 9, 10, 11, 12, 13, 14, 15, 16, 17]. AOI holds great promise as a tool to probe hidden structure inside of highly-scattering media, such as clouds, paint and biological tissue—a problem which is of both fundamental interest and considerable applied importance [18]. For instance, in biomedical applications, optical methods provides unique capabilities to assess physiological function including blood volume and tissue oxygenation [19, 20, 21]. At the same time, such methods have the molecular selectivity to map gene expression and other markers of bio-molecular activity.

In a typical AOI experiment, a highly-scattering medium is illuminated by a coherent optical source and the resulting speckle pattern is registered by a detector. A focused ultrasound beam is then introduced and the speckle modulation is recorded as the beam's focus is scanned throughout the medium. Since the scatterers in the medium are displaced by the acoustic wave, the scattered light undergoes a frequency shift which permits the localization of the resulting so-called tagged photons to the volume containing the focus. The intensity images that are

obtained in this manner convey information about the medium. However, they are not tomographic, nor are they quantitatively related to the optical properties of the medium.

In this talk we consider the inverse scattering problem that arises in AOI. We show that it is possible to reconstruct tomographic images of the optical properties of a medium from *incoherent* measurements of multiply-scattered light that is modulated by a standing acoustic wave. The principle advantages of the proposed method compared to conventional methods for imaging with diffuse light are two fold. (i) The resolution of reconstructed images is, in principle, much higher than in diffuse optical tomography (DOT). In particular, the inverse problem of AOI is well-posed and the image resolution is controlled by the acoustic wavelength. In contrast, the inverse scattering problem for diffuse waves is severely ill-posed, which leads to the relatively low resolution of DOT [22, 23]. Physically, the improvement in resolution in AOI can be understood to be a consequence of controlling an internal degree of freedom of the scattering medium (the density of scatterers) by means of an external wave field. (ii) Neither interferometric measurements of tagged photons nor the use of a focused acoustic wave field is required. This considerably simplifies the experimental realization of the method.

References

[1] M. Born and E. Wolf, *Principles of Optics* (Cambridge University Press, Cambridge, 1999)
[2] W. Leutz and G. Maret, Physica B **204**, 14 (1995)
[3] F.A. Marks, H.W. Tomlinson and G.W. Brooksby, Proc. SPIE **1888**, 500 (1993)
[4] M. Kempe, M. Larionov, D. Zaslavsky and A.Z. Genack, J. Opt. Soc. Am. 14, 1151 (1997)
[5] E. Granot, A. Lev, Z. Kotler, B.G. Sfez and H. Taitelbaum, J. Opt. Soc. Am. A **18**, 1962 (2001)
[6] L.H. Wang, S.L. Jacques and X. Zhao, Opt. Lett. **20**, 629 (1995)
[7] L.H. Wang and Q. Shen, Opt. Lett. **23**, 561 (1998)
[8] L.-H.V. Wang and G. Ku, Opt. Lett. **23**, 975 (1998)
[9] G. Yao, S. Jiao and L.-H.V. Wang, Opt. Lett. **25** 734 (2000)
[10] J. Li and L.-H.V. Wang, Appl. Opt. **41**, 2079 (2002)
[11] J. Li, G. Ku and L.-H.V. Wang, Appl. Opt. **41** 6030 (2002)
[12] S. Leveque, A.C. Boccara, M. Lebec and H. Saint-Jalmes, Opt. Lett. **24**, 181 (1999)
[13] S. Leveque-Fort, J. Selb, L. Pottier and A.C. Boccara, Opt. Comm. **196**, 127 (2001)
[14] M. Atlan, B.C. Forget, F. Ramaz, A.C. Boccara and M. Gross, Opt. Lett. **30**, 1360 (2005)
[15] M. Gross, M. Lesaffre, F. Ramaz, P. Delaye, G. Roosen and A.C. Boccara, Eur. Phys. J. E **28**, 173
[16] A. Lev, Z. Kotler and B.G. Sfez, Opt. Lett. **25** 378 (2000)
[17] A. Lev and B.G. Sfez, Opt. Lett. **27**, 473 (2002)
[18] M. C. W. van Rossum and Th. M. Nieuwenhuizen, Rev. Mod. Phys. **71**, 313 (1999)
[19] V. Ntziachristos, J. Ripoll, L. V. Wang and R. Weissleder, Nat. Biotechnol. **23**, 313 (2005)
[20] J. Ripoll, R. Schulz and V. Ntziachristos, Phys. Rev. Lett. **91**, 103901 (2003)
[21] J. Ripoll and V. Ntziachristos, Phys. Rev. Lett. **96**, 173903 (2006)
[22] S. R. Arridge, Inverse Probl. **15**, R41 (1999)
[23] G. Bal, Inverse Probl. **25**, 053001 (2009)

Models for Optical Tomography and Photoacoustics

Guillaume Bal

Abstract

Imaging optical properties of tissues is useful because of the large optical contrast that exists between healthy and unhealthy tissues. However, photons undergo multiple scattering in the regimes of interest and as a consequence, optical tomography suffers from a rather poor spatial resolution. Photoacoustics is a novel hybrid modality which allows us to combine the large contrast of optical waves with the good resolution properties of ultrasounds. This note summarizes results obtained recently by the author and his colleagues in optical tomography and quantitative photoacoustics. We refer the reader to [1, 2, 3] for the details.

1. Inverse Transport and Optical Tomography

Propagation of photons in tissues is accurately modeled by the following transport equation:

$$\begin{aligned} & v\cdot\nabla_x u+\sigma(x)u=\int_V k(x,v',v)u(x,v')dv', && (x,v)\in X\times V \\ & u_{|\Gamma_-}(x,v)=g(x,v) && (x,v)\in\Gamma_-. \end{aligned} \tag{1}$$

Here, $u(x,v)$ is the density of photons at position $x\in X\subset\mathbb{R}^d$ (with $d=3$ in practice) and with direction $v\in V=S^{d-1}$ and $g(x,v)$ models the density of particles entering the domain. The sets of incoming conditions Γ_- and outgoing conditions Γ_+ are defined by

$$\Gamma_\pm=\{(x,v)\in\partial X\times V,\ \text{s.t.}\ \pm v\cdot\nu(x)>0\}, \tag{2}$$

where $\nu(x)$ is the outgoing normal vector to X at $x\in\partial X$.

The optical parameters $\sigma(x)$ and $k(x,v',v)$ model the interaction of the propagating particles with the underlying structure. The parameter $\sigma(x)$ models the total absorption of particles caused either by *true*, intrinsic, absorption or by scattering of particles into other directions. The scattering coefficient $k(x,v',v)$ indicates the amount of particles scattering from a direction v' into a direction v at position x. In most inverse problems considered in this paper, σ and k are the unknown parameters that need to be reconstructed from available measurements. The measurements considered here are measurements collected at the boundary ∂X of the domain of interest. The measurements are therefore functionals of the incoming density of particles $u_{|\Gamma_-}(x,v)$ and outgoing density of particles $u_{|\Gamma_+}(x,v)$. While $u_{|\Gamma_-}(x,v)=g(x,v)$ is prescribed, $u_{|\Gamma_+}(x,v)$ is obtained by solving (1). The relationship between both quantities is the so-called *albedo* operator defined by

$$\mathcal{A}:=\mathcal{A}[\sigma,k]: u_{|\Gamma_-}(x,v)\mapsto \mathcal{A}u_{|\Gamma_-}(x,v)=u_{|\Gamma_+}(x,v). \tag{3}$$

In the presence of full measurements of $\mathcal{A}=\mathcal{A}[\sigma,k]$, the optical coefficients σ and k can uniquely and stably be reconstructed. This is based on a decomposition of $\mathcal{A}$ into singular components. The first component is the ballistic component, obtained

by solving the above transport equation with $k \equiv 0$. The second component is the single scattering component, which is the part of $u_{|\Gamma_+}$ that is linear in k. Such components can be extracted from measurement of $\mathcal{A}$ by singularity analysis and allow us to reconstruct both optical parameters stably. We refer the reader to the review paper [1] and its references for the detail and the long history of this classical inverse problem.

The main difficulty in optical tomography is that: (i) the ballistic part is typically too weak in practice to be extracted from available measurements; and (ii) often only angularly averaged measurements such as e.g. the current $J(x) := \int_V u_{|\Gamma_+}(x,v)v \cdot \nu(x)dv$ are available. In such measurements, the singularities of the albedo operator are not captured. As in most inverse problems where singularities do not propagate, the inverse transport problem becomes severely ill-posed. This is the situation encountered in most applications of optical tomography and the main theoretical reason why good (millimeter) resolution typically cannot be achieved; see [1] and the references cited there again for the details.

2. Photoacoustics and Inverse Problems with Internal Data

In spite of its limited resolution, optical tomography is still useful as the optical coefficients (primarily the absorption coefficient) exhibit large contrasts between healthy and unhealthy tissues. A very promising modality to observe the large optical contrast while obtaining good resolution is offered by photoacoustics.

Photoacoustic imaging is a recent medical imaging technique combining the large contrast between healthy and unhealthy tissues of their optical parameters with the high spatial resolution of acoustic (ultrasonic) waves. Electromagnetic radiation (photons), sent through a domain of interest, generates heating and thus a thermal expansion of the underlying tissues. The resulting mechanical displacement of the tissues generates acoustic waves, which then propagate through the medium and are recorded by an array of detectors (ultrasound transducers). A first step in the inversion thus consists in reconstructing the amount of heating by solving an inverse source problem for a wave equation. This inversion is relatively simple when the sound speed is constant and full measurements are available. It becomes much more challenging when only partial measurements are available and the sound speed is not constant. Here, we assume this first step done (see the references cited in [2] for details).

In a second step, called quantitative photoacoustics, we wish to reconstruct the optical parameters from the reconstructed source of heating. We define

$$\sigma_s(x,v) = \int_{S^{d-1}} k(x,v,v')dv', \qquad \sigma_a(x,v) = \sigma(x) - \sigma_s(x,v). \tag{4}$$

The available internal information is now given by the new measurement operator

$$\begin{aligned} A = A[\sigma,k]: \quad L^1(\Gamma_-, d\xi) &\to L^1(X) \\ g(x,v) &\mapsto A\phi(x) = H(x) := \int_{S^{n-1}} \sigma_a(x,v)u(x,v)dv. \end{aligned} \tag{5}$$

Here, we recognize $H(x)$ as the source of heating, which is proportional to the spatial density of photons and to the absorption coefficient.

Note that the data $H(x)$ are now internal data. This however does not mean that detectors are placed inside the domain, which would be intrusive. Rather, this means that a first inverse problem (a well-posed inverse source problem for the wave equation) has been solved accurately.

Although the available data are angularly averaged, they now are internal and the optical coefficients can be reconstructed stably from such measurements, at least their spatial structure. It is shown in [2] that $\sigma_a(x,v)$ and $\sigma_s(x,v)$ can be uniquely and stably reconstructed from knowledge of A. The full anisotropy in the scattering coefficient $k(x,v',v)$ however does not seem to be amenable to stable reconstructions. What we show in [2] is that some degree of anisotropy can be reconstructed stably. For instance, when $k(x,v',v)$ is modeled by a Henyey-Greenstein kernel, then the (scalar) degree of anisotropy can be reconstructed uniquely and stably; see [2] for the details.

The above results show that photoacoustic measurements indeed allow us to perform stable reconstructions. However, the aforementioned results require the full operator A, which corresponds to a continuum (hence an infinite number) of boundary illuminations $g(x,v)$ of the domain of interest. Assuming that σ_a and σ_s depend only on the spatial variable x, it remains an interesting question to understand how many measurements $H(x)$ (corresponding to equally many illuminations $g(x,v)$) would be necessary. We do not know how to answer this question for the transport equation. However, some results have been obtained for the diffusion approximation to transport. When k in the transport equation becomes large, i.e., when photons interact very often with the underlying structure, the transport equation is well approximated by a diffusion equation; see e.g. [1].

The propagation of radiation in scattering media is then modeled by the following diffusion equation:

$$\begin{aligned} &-\nabla\cdot D(x)\nabla u+\sigma_a(x)u=0, \qquad x\in X,\\ &u(x)=g(x) \qquad\quad x\ \in\partial X. \end{aligned} \tag{6}$$

Our results in [3] show that under appropriate regularity measurements, there is an open set of illuminations g_1 and g_2 such that availability of the data $H_1=\sigma_a(x)u_1(x)$ and $H_2=\sigma_a(x)u_2(x)$, with $u_{1,2}$ solution of (6) with g replaced by $g_{1,2}$, uniquely determines both coefficients $\sigma_a(x)$ and $D(x)$. Moreover, the reconstruction is stable and under additional geometric constraints, we find that for $k\geq 3$,

$$\|D-\tilde{D}\|_{C^k(X)}+\|\sigma_a-\tilde{\sigma}_a\|_{C^k(X)}\leq C\|H-\tilde{H}\|_{(C^{k+1}(X))^{2n}}. \tag{7}$$

Here, $H=(H_1,H_2)$ corresponds to two measurements and $\tilde{H}$ corresponds to measurements performed with σ_a and D replaced by $\tilde{\sigma}_a$ and $\tilde{D}$, respectively. This shows that two well-chosen measurements are indeed sufficient to reconstruct two coefficients. Moreover, we observe that the reconstruction is stable in the sense given in (7). In this mathematical framework, photoacoustics indeed displays good

resolution properties and corresponds to a well-posed (mildly ill-posed) inverse problem, unlike optical tomography which is a severely ill-posed inverse problem.

References

[1] G. Bal, *Inverse transport theory and applications*, Inverse Problems, 25 (2009), p. 053001.
[2] G. Bal, A. Jollivet, and V. Jugnon, *Inverse transport theory of Photoacoustics*, Inverse Problems, 26 (2010), p. 025011.
[3] G. Bal and G. Uhlmann, *Inverse diffusion theory for photoacoustics*, to appear in Inverse Problems, (2010).

An accurate approximate algorithm for motion compensation in two-dimensional tomography

Alexander Katsevich

Reconstruction of objects which change during data acquisition is an important challenge facing modern computed tomography (CT). The prime example is cardiac CT, where one needs to reconstruct the beating heart. Another example is the reduction of artifacts related to the patient's breathing. It appears that the most promising approach to the reconstruction of dynamic objects is based on incorporating a motion model into the reconstruction algorithm (see e.g. [2, 3, 4, 5, 6]). This approach is commonly referred to as motion compensation. Since all available data are used by motion compensation algorithms (as opposed to gating approaches, which use only the data least contaminated by noise), they have the potential to provide the best image quality with the least x-ray dose. Typically these algorithms are of iterative nature, but some progress has been achieved towards noniterative reconstruction [2, 7, 8]. As is common in literature on motion compensation, we assume throughout the paper that motion is known. In practice this is frequently not the case, so one has to deal with the motion estimation problem (which is not considered here).

Mathematically, the problem of motion compensation is equivalent to inverting the generalized Radon transform (RT) R_ϵ, where one integrates the unknown function f over a family of curves. Here ϵ is a parameter, which controls how far R_ϵ is from the classical RT R that integrates along straight lines. Thus, we will assume in what follows that $R_\epsilon \to R$ as $\epsilon \to 0$. In [1] it was shown how to invert R_ϵ modulo a smoothing pseudo-differential operator (PDO). A similar result was obtained recently in [9]. In [9] a function f_{pl} is proposed such that, analogously to [1], $f - f_{pl}$ is smoother than f in the scale of Sobolev spaces. The main novel point is that computation of f_{pl} can be done efficiently using a Filtered Backprojection (FBP) algorithm. While these results are useful when one wants to recover singularities of the unknown function f, there are no estimates on how small the smooth error term is. In particular, such inversion formulas cannot be used for finding pointwise values of f.

Alternative results are in [11] and [10]. It is shown in [11] that by selecting the appropriate dual Radon transform R^* and singular convolution operator K one has: $\mathcal{E}_\epsilon := R^*KR_\epsilon - \mathrm{Id}$ is a PDO of order -1, and the norm of $\mathcal{E}_\epsilon : L^2_0(U) \to L^2_{loc}(U)$

goes to zero if $\epsilon \to 0$. Here U is an open set containing the support of f, and Id is the identity operator. Even though the error term is smoother than f, it does not have to be small in a norm stronger than that of $L^2(U)$.

Assuming that the manifold of curves is sufficiently close to the family of straight lines (i.e., when $\epsilon \to 0$), the following results are established in [10]: $A_\epsilon := R^{-1}R_\epsilon$ is a zero-order Fourier Integral operator, $A_\epsilon^T A_\epsilon = \mathrm{Id} + \mathcal{E}_\epsilon$, and the norm of $\mathcal{E}_\epsilon : L^2(\mathbb{R}^2) \to L^2(\mathbb{R}^2)$ is less then one. Here $R = R_{\epsilon=0}$ is the classical RT. This implies, in particular, that the approximate inversion formula for the generalized RT is $R_\epsilon^{-1} \approx A_\epsilon^T R^{-1}$, and the error term is small in the L^2-norm. Notice that applying the operator $A_\epsilon^T R^{-1}$ is computationally cumbersome, and the error term is as smooth as the original function.

In this talk we propose two approximate inversion formulas for R_ϵ in the cases of parallel beam and fan beam geometries. As before, let $\mathcal{E}_\epsilon$ be the operator which gives the error term $\mathcal{E}_\epsilon f$ of the inversion formula. In both cases (parallel beam and fan beam) we establish the following result: for any integer $m \geq 0$ the operator $\mathcal{E}_\epsilon : H_0^m \to H_0^{m+1}$ is bounded and $||\mathcal{E}_\epsilon|| \to 0$ as $\epsilon \to 0$. Thus the error term is guaranteed to be smoother than f in the Sobolev scale. Also, if $\epsilon > 0$ is small, the stronger norm of the error term is small as well. An additional benefit is that the formulas can be easily implemented numerically.

In the second part of the talk we propose a motion-compensated local tomography function for cone beam CT. We study its main properties, including the location and strength of the non-local artifacts. As opposed to cone beam local tomography in the static case, it is not possible here to find the direction of differentiation, which reduces the strength of the artifact by one order in the scale of Sobolev spaces.

References

[1] A. S. Denisyuk, *Inversion of the generalized Radon transform*, in book: *Applied problems of Radon transform* (S. Gindikin, editor), Amer. Math. Soc., Amer. Math. Soc. Translations Series 2, Providence, RI, **162** (1994), 19–32.

[2] S. Rit, D. Sarrut, and L. Desbat, *Comparison of Analytic and Algebraic Methods for Motion-Compensated Cone-Beam CT Reconstruction of the Thorax*, IEEE Transactions on Medical Imaging **28** (2009), 1513–1525.

[3] A. A. Isola, A. Ziegler, T. Koehler, W. J. Niessen, and M. Grass, *Motion-compensated iterative cone-beam CT image reconstruction with adapted blobs as basis functions*, Physics in Medicine and Biology **53** (2008), 6777–6797.

[4] U. van Stevendaal, C. Lorenz, J. von Berg, and M. Grass, *Motion-Compensated Reconstruction in Helical Cardiac CT*, in book: *Proceedings of the IXth International Conference on Fully 3D Reconstruction in Radiology and Nuclear Medicine. Lindau, Germany. July 9 - 13, 2007* (M. Kachelriess and F. Beekman, editors), (2007), 437–440.

[5] C. Blondel, R. Vaillant, G. Malandain, and N. Ayache, *3D tomographic reconstruction of coronary arteries using a precomputed 4D motion field*, Physics in Medicine and Biology **49** (2004), 2197–2208.

[6] J. Pack and F. Noo, *Dynamic computed tomography with known motion field*, in book: *Proc. Medical Imaging 2004: Image Processing* (J. M. Fitzpatrick and M. Sonka, editors), Proceedings SPIE-5370 (2004), 2097–2104.

[7] K. Taguchi and H. Kudo, *Motion compensated fan-beam reconstruction for nonrigid transformation*, IEEE Transactions on Medical Imaging **28** (2008), 907–917.

[8] L. Desbat, S. Roux, and P. Grangeat, *Compensation of some time dependent deformations in tomography*, IEEE Transactions on Medical Imaging **26** (2007), 261–269.
[9] A. Katsevich, *An approach to motion compensation in tomography*, in book: *Biomedical Mathematics: Promising Directions in Imaging, Therapy Planning and Inverse Problems* (Y. Censor, M. Jiang, and G. Wang, editors), Medical Physics Publishing, Madison, Wisconsin, 2009.
[10] D. A. Popov, *The Generalized Radon Transform on the Plane, the Inverse Transform, and the Cavalieri Conditions*, Functional Analysis and Its Applications **35** (2001), 270–283.
[11] G. Beylkin, *The inversion problem and applications of the generalized Radon transform*, Comm. Pure and Appl. Math. **37** (1984), 270–283.

Texture analysis and Funk transform in the rotation group

Victor Palamodov

Reconstruction of a function on the group $\mathbf{SO}(3)$ from data of circular integrals is the mathematical model for the quantitative texture analysis of polycrystalline materials by means of X-ray or neutron diffraction data, see [6]. The integrand is called in this context "orientation distribution function" (ODF) and the mean of integrals over a union of two orthogonal circles - "pole density function" (PDF). A numerical data of PDF is obtained from X-ray diffraction experiments. The problem of texture analysis is to extract information on ODF from knowledge of PDF. Several methods of reconstruction (the even part of) an ODF from data of PDF are known since sixties: expansion in spherical harmonics [3],[6] a Funk-type inversion formula [1],[4],[5], backprojection inversion [7] and inversion by singular integral operator [8]. In fact only even Fourier coefficients of ODF can be reconstructed from PDF. These methods work also for reconstruction of a function in the group from data of its circle integrals instead of PDF, but anyway they were applied only to the complete 4D data. The complete data is however not technically attainable and redundant.

We describe explicit methods that allow to reconstruct a function from some nonredundant samplings of circle integrals. We discuss the range conditions for the Funk transform. The classical group $\mathbf{SO}(3)$ possesses a natural invariant metric and is isometric as a Riemannian manifold to the projective space $\mathbb{RP}_3$. Therefore there are many closed geodesics in $\mathbf{SO}(3)$ (projective lines) and many toitally geodesic 2-manifolds which are projective planes. The variety of circles is parametrized by two unit 3-vectors $\mathbf{h}, \mathbf{y} \in \mathbf{S}^2$. The manifold Σ is isomorphic to $\mathbf{S}^2 \times \mathbf{S}^2/\mathbb{Z}_2$ since $\mathbf{C}(-\mathbf{h}, -\mathbf{y}) = \mathbf{C}(\mathbf{h}, \mathbf{y})$. A circle $\mathbf{C}(\mathbf{h}, \mathbf{y})$ is the set of rotations g such that $g\mathbf{h} = \mathbf{y}$. Any circle is a projective line and has a natural angular parametrization $0 \le \varphi < 2\pi$. For a continuous function f in $\mathbf{SO}(3)$ the Funk transform is defined as the function

$$Mf(\mathbf{C}) = \int_{\mathbf{C}} f \mathrm{d}\varphi$$

in the manifold Σ. We describe two analytic methods of reconstruction of a function f from nonredundant data of integrals Mf on a 3D subvariety $Z \subset \Sigma$.

Theorem 1. *Let* Γ *be an arbitrary noncontractible plane curve in* $\mathbf{SO}(3)$. *Any square integrable function* f *in the group can be explicitly reconstructed from known integrals* $Mf(\mathbf{C}(\mathbf{h},g\mathbf{h}))$ *for* $\mathbf{h} \in \mathbf{S}^2$, $g \in \Gamma$.

Theorem 2. *Let* Γ *be an arbitrary noncontractible curve in* $\mathbf{SO}(3)$. *Any continuous function* f *can be explicitly recovered from data of integrals* $Mf(\mathbf{C}(\mathbf{h}, -g\mathbf{h}))$ *for* $\mathbf{h} \in \mathbf{S}^2$, $g \in \Gamma$.

There is apparent symmetry between these results. The reconstructions can be considered as solutions of a boundary value for the John-type equation (cf. [2]) which expresses a range condition of the Funk operator M. This boundary value problem is in fact a Goursat-type problem since the manifold Z of circles $\mathbf{C}(\mathbf{h},g\mathbf{h})$ as in Theorem 1 is characteristic with respect to the John-type operator. The same true also for the manifold $Z' = \{\mathbf{C}(\mathbf{h}, -g\mathbf{h})\}$ as in Theorem 2.

References

[1] Funk P. 1915 Über eine geometrische Anwendung der Abelschen Integralgleichung. *Mathematische Annalen* **77**(1) 129–135

[2] John F 1938 The ultrahyperbolic differential equation with 4 independent variables *Duke Math. J.* **4** 300-322

[3] Roe R 1965 Description of crystallite orientation in polycrystalline materials: III. General solution to pole figure inversion *J. Appl. Phys.* **36** 2024–31

[4] Matthies S 1979 On the reciprocity of the orientation distribution function of texture sampled from pole figures (ghost phenomeha). *Physica Status Solidi B* **92** K135-K138

[5] Esling C, Bunge H-J and Muller J 1981 An inversion formula expressing the texture function in terms of angular distribution functions *J. Physique* **42** 161–165

[6] Bunge H 1982 *Texture Analysis in Materials Science. Mathematical Methods.* Butterworths: London, Boston

[7] Bernstein S and Schaeben H 2005 A one-dimensional Radon transform on SO(3) and its application to texture goniometry *Mathematical Methods in the Applied Sciences* **28** 1269–1289

[8] Ivanova T and Savëlova T 2007 A new inversion formula for solving an inverse diffraction problem. (Russian) *Zh. Vychisl. Mat. Mat. Fiz.* **47** 16–20; english translation in *Comput. Math. Math. Phys.* **47** 14–18

A Mumford-Shah level set approach for tomography

Esther Klann

(joint work with Ronny Ramlau, Wolfgang Ring)

Abstract. In this article, a Mumford-Shah based approach for tomography is presented. We consider simultaneous reconstruction and segmentation of activity and density distribution from hybrid SPECT/CT data as well as the reconstruction of the singularity set from limited tomography data. The functions are modelled as piecewise constant with respect to a set of contours. Shape sensitivity analysis is used to find a descent direction for the cost functional which leads to an update formula for the contour in a level set framework.

1. The Mumford-Shah functional for inverse problems

Tomography, a widely used technique in medical imaging, is known to be an inverse and ill-posed problem and therefore requires a regularization. In recent years [2, 3], we have investigated methods for the simultaneous reconstruction and segmentation of a function f from tomographic data $A(f)$ by generalizing the ideas of Mumford and Shah [1]. The segmentation is represented by a geometrical variable Γ that describes the singularity set of the function f. The simultaneous reconstruction and segmentation is gained as minimizer of the Mumford-Shah like functional

$$J^{\mathrm{MS}}(f,\Gamma) = \|A(f) - y^\delta\|_Y^2 + \alpha|\Gamma| + \beta\mathcal{P}(f)\ . \tag{1}$$

The first term measures the data fit, the second term is a regularization on the length of the segmenting contour and the third term realizes additional properties of f that might also be necessary in order to guarantuee stability of the functional reconstruction in (1). As inner organs (liver, lung) and also bones have closed surfaces as boundaries and approximately constant density, it is reasonable to restrict the reconstructions to piecewise constant functions. With these assumptions, the third term in (1) can be neglected.

Let Γ denote a finite collection of pairwise disjoint, closed, bounded curves, and $\{\Omega_i^\Gamma\}_{i=1}^{n(\Gamma)}$ denote the set of all bounded connected components of $\mathbb{R}^2 \setminus \Gamma$. We define the space of piecewise constant functions with respect to a geometry Γ, i.e., any finite collection of pairwise disjoint, closed, bounded curves, as

$$PC(\Gamma) = \Big\{ \sum_{i=1}^{n(\Gamma)} \alpha_i \, \chi_{\Omega_i^\Gamma} \ : \ \alpha_i \in \mathbb{R} \Big\} \subset L^2(D)$$

where χ_Ω denotes the characteristic function of the set Ω.

2. Minimization Algorithm

An algorithm for the minimization of the functional (1) which updates both variables Γ and f independently is difficult to formulate. This is mainly due to the fact that the geometry Γ defines the domain of definition for the functional variable f and thus does not allow to treat f and Γ as independent. We therefore choose a reduced formulation where we alternately fix the geometric variable and minimize with respect to the functional variable and vice versa, see [2, 3] for details.

Step 1: Choose an initial estimate Γ_0.
Step 2: Fix Γ and solve the optimality system $\partial_f J(f(\Gamma),\Gamma)\cdot\delta f = 0$.
Step 3: Find a descent direction F such that

$$dJ(\Gamma;F) = \partial_f J(f(\Gamma),\Gamma) f'(\Gamma;F) + d_\Gamma J(f(\Gamma),\Gamma;F) < 0.$$

Step 4: Update Γ by moving it in the chosen descent direction.
Step 5: Repeat Steps 2-4; check for optimality; introduce new components.

Remark: In Step 1, an inital estimate can be gained from the backprojection of the given data. In Step 2, for $f \in \mathrm{PC}(\Gamma)$ we have to solve a low-dimensional (linear

or non-linear depends on the operator) system of equations for the coefficients α_i. In Step 3, the derivative of J with respect to Γ is computed using techniques from shape sensitivity analysis [4, 5, 2]. According to Step 2, we have $dJ(\Gamma; F) = d_\Gamma J(f(\Gamma)\Gamma; F)$. In Step 4, the update of the geometry is done using a level-set formulation [6, 7]. In Step 5, we repeat Steps 2 to 4 and check for optimality by computating the shape and functional derivatives. A heuristic method is used to enhance the segmentation by introducing new components.

3. SPECT/CT and limited tomography

3.1. **SPECT/CT.** We assume that we have two (noisy) data sets y^δ and z^δ of activity f and density μ from an integrated SPECT/CT scanner. With R and A denoting the Radon and the attenuated Radon transform, it is $z^\delta \sim R\mu$ and $y^\delta \sim A(f, \mu)$.

With the Mumford-Shah approach, we find simultaneously the singularity sets Γ^f, Γ^μ and the functions $f \in PC(\Gamma^f)$ and $\mu \in PC(\Gamma^\mu)$ such that the given data y^δ and z^δ are fitted best possible in a least-squares sense. The functional (1) for the SPECT/CT problem is [3]

$$(2)\quad J(f, \mu, \Gamma^f, \Gamma^\mu) = \|A(f, \mu) - y_d\|^2_{L^2(\mathbb{R}\times S^1)} + \beta\|R\mu - z_d\|^2_{L^2(\mathbb{R}\times S^1)} + \alpha(|\Gamma^f| + |\Gamma^\mu|).$$

The realization of Step 3 of the minimization algorithm (descent direction for the geometry update) requires the implementation of the adjoints of the Frechet derivative of the attenuated Radon transform $A(\cdot, \cdot)$ as well as the evaluation of several boundary integrals.

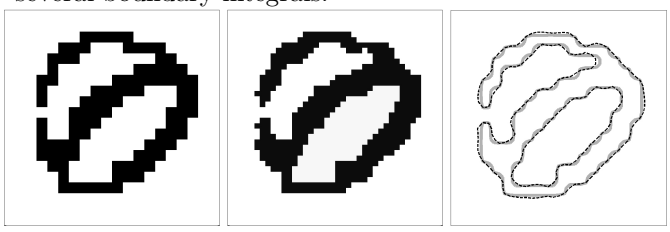

Figure 1: Left to right: Heart phantom (gap in the blood flow). Reconstruction from SPECT/CT data with 10% noise. Contours: original (gray, solid) and reconstructed (black, dashed).

3.2. **Limited Angle Tomography (joint work with Todd Quinto).** Singularities of an object can be detected from limited angle tomographic data when one has measurements over a line perpendicular to the singularity (e.g., tangent to a part of the boundary of the object) [8]. We adapted the Mumford-Shah functional (1) to limited angle data. We generated an ellipsoid test phantom containing two narrow rectangles, one in horizontal and one in vertical direction, two squares, two triangles and a circle. Measurements are taken over a range of $\pm 60°$ from the vertical axis. Figure 2 shows results from first test computations from full (left) and limited data (right). From the limited data reconstruction one can see that all singularities (boundaries) in vertical orientation are detected well. For the horizontally oriented rectangle the narrow sides are also reconstructed well, reconstruction of boundaries oriented exclusively horizontal is impossible [8].

The work was supported by FWF-projects P19029-N18 and P19496-N18.

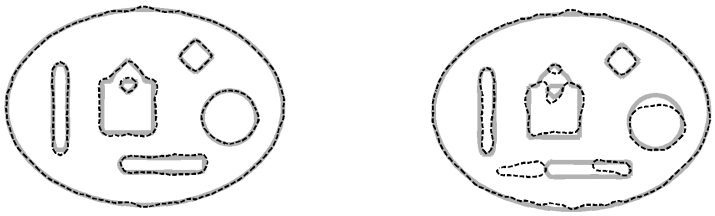

FIGURE 2. Test phantom: original contours (gray, solid) and reconstructed contours (black, dashed) Left: reconstruction from full Radon data. Right: reconstruction from limited angle tomographic data (measurements are missing over the horizontal line $\pm 30°$).

REFERENCES

[1] D. Mumford and J. Shah, Optimal approximations by piecewise smooth functions and associated variational problems., Comm. Pure Appl. Math., **42(5)**, 577-685, 1989.

[2] R. Ramlau and W. Ring, *A Mumford–Shah level-set approach for the inversion and segmentation of X-ray tomography data*, J. Comput. Phys., **221(2)**, 539-557, 2007.

[3] E. Klann, R. Ramlau and W. Ring. *A Mumford-Shah level-set approach for the inversion and segmentation of SPECT/CT data*, RICAM Reports, 2009-06, 2009.

[4] J. Sokołowski and J-P. Zolesio, *Introduction to shape optimization*, Springer (1992).

[5] M.C. Delfour and J-P. Zolésio, *Shapes and geometries: Analysis, differential calculus and optimization*, SIAM(2001).

[6] S. Osher and J.A. Sethian, *Fronts propagating with curvature-dependent speed: Algorithms based on Hamilton-Jacobi formulations*, J. Comput. Phys., **79(1)**, 1988.

[7] S. Osher and R. Fedkiw, *Level set methods and dynamic implicit surfaces*, Springer(2003).

[8] E.T. Quinto, *Singularities of the X-ray transform and limited data tomography in* $\mathbb{R}^2$ *and* $\mathbb{R}^{3*}$, SIAM J. Appl. Math., **24(5)**:1215–1225, 1993.

Computing Complex Frequency Dependent Shear Moduli

JOYCE R. MCLAUGHLIN

(joint work with Kui Lin)

Introduction: Shear stiffness imaging of tissue is a rapidly evolving medical imaging technology where the goal is to image shear biomechanical properties to identify disease, such as cancer or fibrosis, where tissue stiffness changes occur. The starting point for the associated inverse problems is movies of displacement throughout a region of tissue. These movies are made by processing a sequence of B-scans or a sequence of MR data sets acquired while the tissue is moving as a result of mechanical excitation.

Section 2: The Mathematical Model: Tissue is viscoelastic and gives a 3D response to mechanical excitation. In the experiments considered here the displacement amplitude is on the order of tens of microns. We assume a linear solid model governs

the response; that $\mathbf{u}\,(\mathbf{x},t)$ satisfies

$$\rho\,\mathbf{u}_{tt} \;=\; \nabla(\lambda\nabla\cdot\mathbf{u}) \;+\; \nabla\cdot[\mu_0\boldsymbol{\epsilon} \;+\; \int_0^t \sum_{\alpha=1}^{n} e^{-(t-s)/\tau_\alpha}\,\frac{\partial}{\partial s}\,(\mu_\alpha\boldsymbol{\epsilon})ds] \tag{2.1}$$

where $\boldsymbol{\epsilon} \;=\; \nabla\mathbf{u} \;+\; (\nabla\mathbf{u})^T$, λ is the bulk modulus, ρ the density per unit volume, which is assumed to be constant, μ_0 a spring constant and μ_α, τ_α the spring constants and relaxation constants, $\alpha = 1,\ldots,n$, associated with Maxwell elements which are in parallel with the single spring.

The experiment is often designed so that one displacement component is larger than the others; furthermore often only one component of data is acquired. In this case, by necessity, we eliminate the bulk modulus term as well as the $(\nabla\mathbf{u})^T$ term in the strain, $\boldsymbol{\epsilon}$. The three equations in (2.1) then decouple. The decoupled equation for the component u that is measured is then, for the purposes of this paper, Fourier Transformed in time to obtain $\hat{u}(\mathbf{x},\omega)$. At any given frequency, ω, then, $\hat{u}(\mathbf{x},\omega)$ is assumed to satisfy

$$\nabla\cdot(\tilde{\mu}\,\nabla\hat{u}) \;+\; \omega^2\hat{u} \;=\; 0 \tag{2.2}$$

where $\tilde{\mu}$ is complex valued and

$$\tilde{\mu} \;=\; \tilde{\mu_1} \;+\; i\tilde{\mu_2} = \left[\mu_0 \;+\; \sum_{\alpha=1}^{n} \frac{i\omega\mu_\alpha\tau_\alpha}{1+i\omega\tau_\alpha}\right]/\rho.$$

For the forward problem we are given $\mu_0, \mu_\alpha, \tau_\alpha, \alpha = 1,\ldots,n, \rho$ and we find u; for the inverse problem we are given $\hat{u}(\mathbf{x},\omega)$ and we recover $\tilde{\mu} \;=\; \tilde{\mu_1} \;+\; i\tilde{\mu_2}$.

To recover $\tilde{\mu}$ in (2.2), since (2.2) is a first order partial differential equation we will need $\tilde{\mu}$ for at least some values on the boundary of the region of interest. In general these boundary values are not measured so some approximate values must be selected. Our approximation, when these values are needed, will be

$$\hat{\mu} \;=\; -\omega^2\hat{u}/\nabla\hat{u}.$$

This choice is exact when $\tilde{\mu}$ is constant and is justified by the bound given in [1] when $\hat{\mu}$ is real; the same bound can be shown to be valid when $\hat{\mu}$ is complex valued.

Section 3: The Inverse Problem: In this problem we are given complex, time Fourier Transformed, data which is displacement $\hat{u}(\mathbf{x},\omega)$ when $\mathbf{x}\in\Omega\subset R^2$. The unknown $\tilde{\mu} = \mu/\rho$ satisfies

$$\nabla\cdot(\tilde{\mu}\nabla\hat{u}) \;+\; \omega^2\hat{u} \;=\; 0 \qquad \mathbf{x}\in\Omega, \tag{3.1}$$

where $\hat{u}$ is the given data. We assume that $\tilde{\mu}$ is known for any $\mathbf{x}\in\partial\Omega$ where boundary data is needed. In practice we use the approximation given in Section

2. We rewrite (3.1) as

$$\tilde{\mu}_x \ + \ \tilde{a}\tilde{\mu}_y \ + \ \tilde{b}\tilde{\mu} \ + \ \tilde{c} \ = \ 0 \quad \text{where} \quad \tilde{a} = \frac{\hat{u}_y}{\hat{u}_x},\ \tilde{b} = \frac{\Delta\hat{u}}{\hat{u}_x},\ \tilde{c} = \frac{\omega^2\hat{u}}{\hat{u}_x} \tag{3.2}$$

where now the first order p.d.e. is in standard form. If we have measurements $\hat{u}^1$ and $\hat{u}^2$, from two independent experiments, we make a non-linear combination of (3.1) for each $\hat{u}_1, \hat{u}_2$ to obtain

$$0 = \frac{1}{|\ \hat{u}_x^1\ |^2 \ + \ |\ \hat{u}_x^2\ |^2}\ [\tilde{\bar{u}}_x^1\ (\nabla\cdot(\tilde{\mu}\nabla\hat{u}^1) + \omega^2\hat{u}^1) + \tilde{\bar{u}}_x^2(\nabla\cdot\tilde{\mu}\nabla\hat{u}^2) + \omega^2\hat{u}^2]$$

$$= \tilde{\mu}_x \ + \ \tilde{\tilde{a}}\tilde{\mu}_y \ + \ \tilde{\tilde{b}}\tilde{\mu} \ + \ \tilde{\tilde{c}} \tag{3.3}$$

where $\tilde{\tilde{a}}, \tilde{\tilde{b}}, \tilde{\tilde{c}}$ can be straight forwardly calculated.

In each case we arrive at a similar form for the first order p.d.e. At the same time, since the coefficients in the first order p.d.e.'s (3.2) and (3.3) are different, the stability properties due to errors in the boundary conditions may be different.

Three different examples show that the stability can be improved by changing the marching direction or using two well chosen distinct data sets, $\hat{u}^1, \hat{u}^2$. Stability is governed by the signs of the imaginary part of a , see [2], and the real part of b .

Section 4: Methods and Images: Our true value of $\tilde{\mu} \ = \ \tilde{\mu}_1 \ + \ i\ \tilde{\mu}_2$ is given pictorially in Figure 1. Our solutions $\hat{u}^1, \hat{u}^2$ are computed synthetically and are generated by sources at opposite sides of the image plane.

Our recoveries are given in Figures 2-3. These recoveries are generated using a finite difference explicit/implicit method that we prove always controls the exponential error growth that can occur due to the sign of Ima. Our experience is that we can reduce the instability that can occur due to the Reb by changing the marching direction or using multiple data sets.

The recovery is best when we use two data sets and this recovery is a significant improvement over the image obtained when our marching direction is in the direction away from the source.

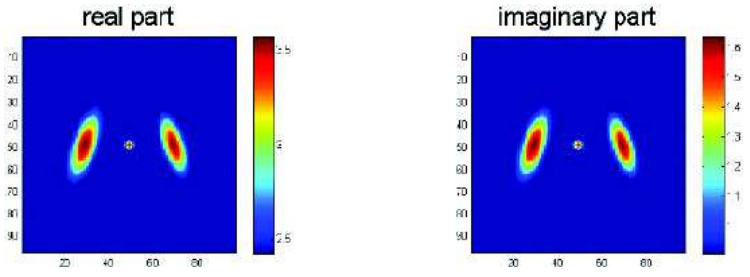

FIGURE 1. Exact complex valued $\tilde{\mu}$.

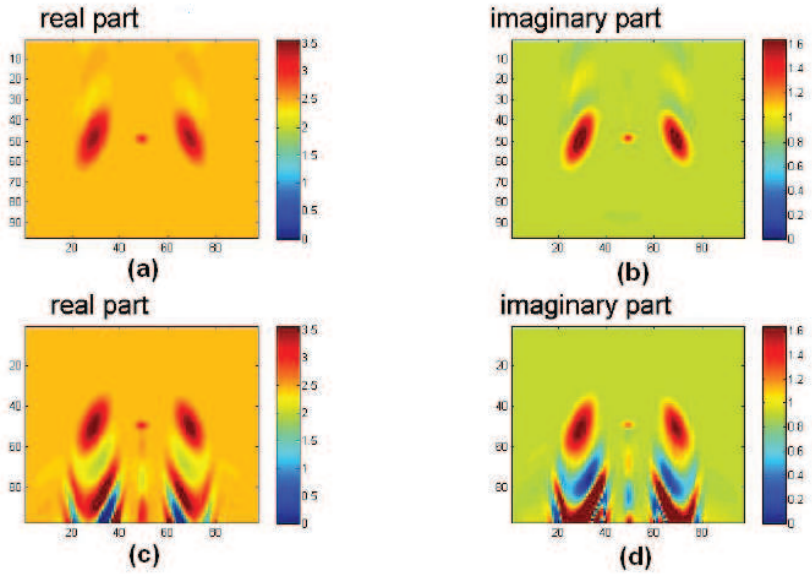

FIGURE 2. Recovery of $\tilde{\mu}$ using (3.2) where in (a), (b) ((c), (d)) the marching direction is toward (away from) the source.

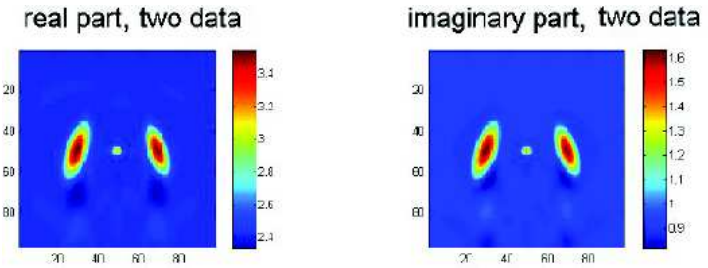

FIGURE 3. Recovery of $\tilde{\mu}$ using (3.3) with two displacements.

REFERENCES

[1] Lin, K., and McLaughlin, J., "An error estimate on the direct inversion model in shear stiffness imaging," *Inverse Problems*, vol. 25(7), July, 2009.

[2] McLaughlin, J., N. Zhang, A. Manducca, "Calculating tissue shear modulus and pressure by 2D Log-Elastographic methods", to appear in *Inverse Problems*.

Comparing and Combining Two Methods of Two-Dimensional Region-of-Interest Reconstruction

Rolf Clackdoyle
(joint work with Catherine Mennessier, Michel Defrise, Dilip Ghosh Roy)

1. Region-of-Interest Reconstruction

In classical (two-dimensional) tomography, the forward model is the Radon transform (or X-ray transform). We use p for the Radon transform of f, so $p(\phi, s) = \int f(r\alpha + s\beta)dr$ for $(\phi, s) \in [0, \pi) \times [-\infty, \infty]$, where $\alpha = (\cos\phi, \sin\phi)$ and $\beta = (-\sin\phi, \cos\phi)$. In practice, the support of f is known, or at least known to be contained within some fixed volume, so $p(\phi, s)$ only needs to be measured for the lines that pass through this volume, since the other values are zero. In this situation the Radon inversion formula can be applied. In the popular filtered-backprojection (FBP) format the inversion takes the following form.

$$f(x) = \int_0^\pi p^*(\phi, x \cdot \beta)\, d\phi, \qquad \text{where } p^*(\phi, s) = \frac{1}{2\pi} \int p(\phi, s') h'_\epsilon(s - s')\, ds'$$

and where h'_ϵ, defined below, is a regular function that approximates the ramp-filter kernel [1]. All equations are understood to be taken in the limit as $\epsilon \to 0$.

$$h'_\epsilon(s) = \begin{cases} \dfrac{-1}{\pi s^2} & \text{if } |s| \geq \epsilon \\ \\ \dfrac{1}{\pi \epsilon^2} & \text{if } |s| < \epsilon \end{cases} \qquad h_\epsilon(s) = \begin{cases} \dfrac{1}{\pi s} & \text{if } |s| \geq \epsilon \\ \\ \dfrac{s}{\pi \epsilon^2} & \text{if } |s| < \epsilon \end{cases}$$

The expression for h_ϵ on the right is a regular approximation to the Hilbert transform kernel, compatible with the ramp-filter kernel h'_ϵ (recalling that ramp-filtering is the composition of the derivative with the Hilbert transform). In region-of-interest (ROI) reconstruction, the Hilbert transform plays a major role.

The two-dimensional (2D) ROI reconstruction problem can be stated as follows. If $p(\phi, s)$ is known for all (ϕ, s) in a proper subset of $[0, \pi) \times [-\infty, \infty]$, what is the maximal ROI that can stably reconstructed? There have been a number of recent (since 2002) results published on this problem, and virtually all of the analytic results are based either on the principles of the virtual fanbeam (VFB) method or the method of differentiated backprojection with Hilbert filtering (DBP-H). In this work we fix a specific ROI problem, and we use it to examine the difference between the VFB and DBP-H approaches.

The support of f is an ellipse centered at the origin, with major axis of $2a = 40$ cm aligned with the x_1-axis, and minor axis $2b = 20$ cm. The measured data corresponds to the set of all lines that pass through the field-of-view (FOV) of the scanner, which is a circle with the same center as the ellipse, and with diameter $2r = 30$ cm. For the purposes of this work an ROI consisting of (a neighborhood of) the single point $x^* = (x_1, x_2) = (3, 5)$ suffices.

2. The VFB Method

The idea behind the VFB method is that parallel projections that are not truncated can be treated in the usual fashion (FBP equation (1)), and truncated projections are handled by finding a virtual fanbeam projection to supply the Hilbert transform of the parallel projection. See [2], [3], [4] for detailed descriptions.

We refer here to the VFB method as method A for short, and write $f_A(x)$ for the reconstruction formula according to the VFB approach. Note that $f_A(x)$ is just a VFB formula applied to the specific ROI problem identified above, and it is one of many possible VFB formulas for this problem.

$$\begin{aligned} f_A(x) &= \int_0^\pi p^*(\phi, x\cdot\beta)\, d\phi \\ p^*(\phi,s) &= \frac{1}{2\pi}\begin{cases} \int p(\phi,s')h'_\epsilon(s-s')ds' & \text{if } \phi\in[0,\pi]\backslash[\phi_c,\overline{\phi}_c] \\ (\partial/\partial s)\, p_H(\phi,s) & \text{if } \phi\in[\phi_c,\overline{\phi}_c] \end{cases} \end{aligned}$$

Here $\phi_c = \arctan\sqrt{(r^2-b^2)/(a^2-r^2)}$ and $\overline{\phi}_c = \pi - \phi_c$ indicate the transition angles between truncated and non-truncated projections. The Hilbert transform of the projection $p(\phi,\cdot)$ is given by

$$p_H(\phi,s) = g_H(v_{\phi,s},\phi) = \int_\pi^{2\pi} g(v_{\phi,s},\phi')h_\epsilon(\sin(\phi-\phi'))d\phi'$$

with virtual fanbeam projection $g(v_{\phi,s},\phi') = p(\phi', v_{\phi,s}\cdot\beta')$ and virtual vertex $v_{\phi,s} = s\beta + \sqrt{r^2-s^2}\alpha$.

3. The DBP-H Method

We refer to the DBP-H approach as method B. The idea is to identify and treat just one line segment that traverses the object and is completely measured; see [5], [6], [7], [8]. In our specific problem we use the segment S joining the points $[x_1,-R]$ to $[x_1,R]$ where $R=14$ (and recalling that $x_1=3$). Because all lines intersecting this line segment are measured, we can form the backprojection of the derivative of the projection data,

$$b(x) = \int_{\pi/2}^{3\pi/2} p'(\phi, x\cdot\beta)\, d\phi \qquad x\in S$$

where $p'(\phi,s) = (\partial/\partial s)p(\phi,s)$. The reconstructed image f_B is found by applying a finite Hilbert inverse [9] along the line segment S, with constant K found from $f(x_1,y)=0$ where $(x_1,y)=(3,13)$.

$$\begin{aligned} f_B(x) &= \frac{1}{2\pi\sqrt{R^2-x_2^2}}\left(K - \int_{-R}^{R}\sqrt{R^2-t^2}\; b(x_1,t)\; h_\epsilon(x_2-t)\; dt\right), \quad x\in S \\ K &= \int_{-R}^{R}\sqrt{R^2-t^2}\; b(x_1,t)\; h_\epsilon(y-t)\; dt \end{aligned}$$

4. Comparing the Two Methods

The mathematical formulations of the VFB and DBP-H methods are so different that it is difficult to establish the connections between them. By putting both in the form of an inner product with the data, the 'weight functions' of the inner products can be compared. So $f_A(x) =< w_A, p >= \int\int w_A(\phi, s)\, p(\phi, s)\, d\phi ds$ and similarly for $f_B(x)$. Here the weight $w_A(\phi, s)$ indicates the contribution of the line-integral $p(\phi, s)$ to the reconstruction. Note that w_A depends on x; here w_A and w_B are the weight functions for the point $x^* = (3, 5)$.

It can be shown [10] that the VFB weight function for this geometry is

$$w_A(\phi, s) = \frac{1}{2\pi} h'_\epsilon(x \cdot \beta - s)\chi_\phi^{NT} + w^V(\phi, s)\chi_{\phi,s}^V$$

The details of the full expression are given in [10]. Briefly, the characteristic function χ_ϕ^{NT} is equal to 1 for the non-truncated projections, and zero otherwise. The other characteristic function $\chi_{\phi,s}^V$ is equal to 1 for any line intersecting the virtual fanbeam trajectory, an arc on the circle of radius r whose endpoints are defined in terms of the x^*, ϕ_c, and $\overline{\phi}_c$; and zero otherwise. The weighting behavior associated with the virtual fanbeam projections is given in a complicated expression for w^V.

For the DBP-H case, the weight function takes the form

$$w_B(\phi, s) = w^{DBP-H}(\phi, s)\chi^B(\phi, s)$$

where the explicit expression for $w^{DBP-H}(\phi, s)$ can be found in [10], and $\chi^B(\phi, s)$ is equal to 1 if the line (ϕ, s) intersects the segment S, and zero otherwise.

A discussion of the features of these two weight functions appears in [10]. Here we only make two remarks concerning the regions where the weight functions are zero (corresponding to sinogram values that make no contribution to the reconstruction of $f(x^*)$). The first remark is that both weight functions are zero for all lines that lie outside the scanner FOV (the truncated measurements, outside the circle of radius r); this is the mechanism by which the methods are able to perform accurate ROI reconstruction. The second remark is that the regions where the weight functions vanish are not the same. Each method discards some of the *measured* values, but the discarded values differ. This second point is important as it shows that these two methods act react differently to noisy data.

5. Combining the Two Methods

If the noise in the measurement data is known then the effect of this noise on the two reconstructions $f_A(x^*)$ and $f_B(x^*)$ can be established. We write $\sigma^2(\phi, s)$ for the variance of the measurement $p(\phi, s)$ and we assume that the measurements are statistically independent. Writing σ_A^2 for the resulting variance in $f_A(x^*)$, we obtain $\sigma_A^2 =< w_A^2, \sigma^2 >$ and similarly for method B. Comparing σ_A^2 to σ_B^2 shows which method reacts better to the measurement noise.

We can go further. We consider a combined reconstruction $f_\lambda = \lambda f_A + (1-\lambda) f_B$ whose corresponding weight function is obviously $w_\lambda = \lambda w_A + (1-\lambda) w_B$. Now the variance σ_λ^2 of $f_\lambda(x^*)$ is $\sigma_\lambda^2 =< w_\lambda^2, \sigma^2 >=< (\lambda w_A + (1-\lambda) w_B)^2, \sigma^2 >$ which is a

quadratic function in λ with positive leading coefficient. The minimum variance $\sigma^2_{\lambda_m}$ is found at $\lambda_m = < w_B^2 - w_A w_B, \sigma^2 > / < (w_A - w_B)^2, \sigma^2 >$ and we easily verify that $\sigma^2_{\lambda_m} < \sigma^2_A$ and $\sigma^2_{\lambda_m} < \sigma^2_B$.

In general, a different λ_m can be computed for each point in the ROI to provide a minimum-variance reconstruction throughout the ROI using different linear combinations of the two methods. Note that only two reconstructions are needed (method A and method B), and these reconstructions are combined pointwise using different values of λ_m. However λ_m depends on $w_A(x)$ and $w_B(x)$ so the weight functions must be calculated for each point.

Numerical examples will be presented at the *Image Formation in X-ray CT* meeting in Salt Lake City in June 2010, see
http://www.ucair.med.utah.edu/CTmeeting/

References

[1] B. K. P. Horn, *Density reconstruction using arbitrary ray-sampling schemes*, Proc. IEEE **66** (1978), 551–562.

[2] F. Noo, M. Defrise, R. Clackdoyle, H. Kudo, *Image reconstruction from fan-beam projections on less than a short-scan*, Phys. Med. Biol. **47** (2002), 2525–2546.

[3] R. Clackdoyle, F. Noo, G. Guo, J. Roberts, *Quantitative reconstruction from truncated projections in classical tomography*, IEEE Trans. Nucl. **51(3)** (2004), 2570–2578.

[4] R. Clackdoyle, F. Noo, M. S. Ould Mohamed, C. Mennessier, *A FBP reconstructionformula for 2D tomography with bilateral truncation*, Conference Record of the 2006 IEEE Nuclear Science Symposium and Medical Imaging Conference. San Diego, (2006), 2895–2899.

[5] I. M. Gel'fand, M. I. Graev, *Crofton's function and inversion formulas in real integral geometry*, Func. Anal. Appl. **25** (1991), 1-5.

[6] F. Noo, R. Clackdoyle, J. D. Pack, *A two-step Hilbert transform method for 2D image reconstruction*, Phys. Med. Biol. **49** (2004), 3903–3923.

[7] T. Zheng, S. Leng, B. E. Nett, G.-H. Chen, *Fan-beam and cone-beam image reconstruction via filtering the backprojection image of differentiated projections data*, Phys. Med. Biol. **49** (2004), 5489–5503.

[8] Y. Zou, X. Pan, E. Y. Sidky, *Image reconstruction in regions-of-interest from truncated projections in a reduced fan-beam scan*, Phys. Med. Biol. **50** (2005), 13-28.

[9] F. G. Tricomi, Integral Equations (New York: Dover), 1957.

[10] R. Clackdoyle, D. N. Ghosh Roy, C. Mennessier, M. S. Ould Mohamed, *Two-Dimensional Region-of-Interest Reconstruction: Analyzing the Difference between Virtual Fanbeam and DBP-Hilbert Reconstructions*, Conference Record of the 2009 IEEE Nuclear Science Symposium and Medical Imaging Conference. Orlando, (2009), 3367-3371.

Reconstruction and Motion Correction in SPECT Imaging – a Combined Approach

Bernd Fischer

(joint work with Hanno Schumacher, Jan Modersitzki)

Due to the long imaging times in SPECT, patient motion is inevitable and constitutes a serious problem for any reconstruction algorithm. The measured inconsistent projection data lead to reconstruction artifacts which can significantly

affect the diagnostic accuracy of SPECT if not corrected. To address this problem a new approach for motion correction is introduced. It is purely based on the measured SPECT data and therefore belongs to the data-driven motion correction algorithm class. However, it does overcome some of the shortcomings of conventional methods. This is mainly due to the innovative idea to combine reconstruction and motion correction in one optimization problem. The scheme allows for the correction of abrupt and gradual patient motion. To demonstrate its performance several test runs are presented.

In Single Photon Emission Computed Tomography (SPECT), the imaging time is typically in the range of 5-30 minutes. Here, patient movement, which has frequently been reported in clinical applications [1], constitutes a serious problem for any reconstruction scheme. The movements cause misalignment of the projection frames, which degrades the reconstructed image and may introduce artifacts. These motion artifacts may significantly affect the diagnostic accuracy [2, 3, 4]. Different methods have been proposed for the correction of motion in SPECT studies. These methods may be divided into two categories.

The first category includes hardware methods, for example the triple scan [5] or dual scan [6] protocol. These methods do produce motion corrected projections and thus may be used in conjunction with any reconstruction method. Unfortunately not all types of motion, for example gradual motion, can be corrected. Other methods in this category rely on the placement of some markers on the patient and use camera or tracking systems to detect or estimate patient motion during the SPECT imaging [7, 8]. Here, in list-mode the position of each detected photon can be corrected directly in conjunction with every reconstruction algorithm. Yet another way is to subdivide the measured data in sets belonging to the same patient position and employing a reconstruction method based on the estimated motion information [9, 10]. The marker-based approaches clearly decrease the motion artifacts for the price of having to place the markers on each patient and the need for additional equipment.

In this note we advocate the employment of a novel method within the second category, the software methods. These approaches are working solely with the measured raw data. Here one distinguishes between projection- and image-space based approaches. One idea is to reconstruct the image followed by a simulation of SPECT-imaging based on the obtained reconstructed data [11, 12]. Next, the measured projections and the computed forward-projections are compared in order to estimate and to correct for patient motion in the projection-space. It should be noted, that due to the projection geometry, this method is not able to compensate for rotational movement. Therefore a method, the so called Data-Driven Motion Correction (DDMC) approach [13, 14], was developed. Here the idea is to estimate the motion and to correct for it within the image-space by applying a registration scheme onto the images obtained by corresponding partial reconstructions. This method can handle full rigid-body motion. Unfortunately it was designed only for SPECT systems with perpendicular camera-heads. Furthermore, the partial reconstructions have to be based on at least 30% of all measured projections as

the success of the registration scheme relies on high quality partial reconstruction images. Consequently, the DDMC method can only correct for abrupt patient motion and can not be employed for gradual motion problems.

In this note, we report on a novel motion correction approach, working solely on the raw data, which does overcome the above mentioned shortcomings. The new scheme, which Combines Reconstruction and Motion Correction in one optimization step is called CRMC and was briefly introduced in [15]. One may find a similar idea within the super-resolution methodology [16], where roughly speaking, the goal is to obtain a "nice image" out of two or more related "bad images". As it turns out, the CRMC approach is able to correct for abrupt and gradual motion. Furthermore, it works successfully with any one-, two-, or triple-head SPECT system. As it is characteristic for inverse problems, the reconstruction process is ill-posed and its formulation and implementation does need special care. To this end we introduce a novel regularization term which overcomes possible problems and works just fine in practice.

References

[1] Wheat, J.M., Currie, G.M., *Incidence and characterization of patient motion in myocardial perfusion SPECT: Part 1.* J Nucl Med Technol **32**(2) (2004) 60–65.

[2] Botvinick, E.H., Zhu, Y.Y., O'Connell, W.J., Dae, M.W., *A quantitative assessment of patient motion and its effect on myocardial perfusion SPECT images.* J Nucl Med **34**(2) (1993) 303–310.

[3] Cooper, J.A., Neumann, P.H., McCandless, B.K., *Effect of patient motion on tomographic myocardial perfusion imaging.* J Nucl Med **33**(8) (1992) 1566–1571.

[4] Friedman, J., Van Train, K., Maddahi, J., Rozanski, A., Prigent, F., Bietendorf, J., Waxman, A., Berman, D.S., *"upward creep" of the heart: A frequent source of false-positive reversible defects during thallium-201 stress-redistribution SPECT.* J Nucl Med **30**(10) (1989) 1718–1722.

[5] Pellot-Barakat, C., Ivanovic, M., Weber, D.A., Herment, A., Shelton, D.K., *Motion detection in triple scan SPECT imaging.* IEEE Trans Nucl Sci **45**(4) (1998) 2238–2244.

[6] Passalaqua, A.M., Narayanaswamy, R., *Patient motion correction of SPECT images: dual scan approach.* IEEE Proc. NSSS'94, Norfolk, VA **3** (1995) 1270–1274.

[7] Bruyant, P., Gennert, M., Speckert, G., Beach, R., Morgenstem, J., Kumar, N., Nadella, S., King, M., *A robust visual tracking system for patient motion detection in SPECT: hardware solutions.* In: IEEE Nuclear Science Symposium Conference Record. Volume 5. (2004) 3094–3097.

[8] Beach, R., Pretorius, H.P., Boening, G., Bruyant, P.P., Feng, B., Fulton, R.R., Gennert, M.A., Nadella, S., King, M.A., *Feasibility of stereo-infrared tracking to monitor patient motion during cardiac spect imaging.* IEEE Trans. Nucl. Sci. **51**(5) (2004) 2693–2698.

[9] Hutton, B.F., Kyme, A.Z., Lau, Y.H., Skerrett, D.W., Fulton, R.R., *A hybrid 3-D reconstruction/registration algorithm for correction of head motion in emission tomography.* IEEE Trans Nucl Sci **49**(1) (2002) 188–194.

[10] Schumacher, H., Fischer, B., *A new flexible reconstruction framework for motion correction in SPECT imaging.* IEEE Trans. Nucl. Sci. **54** (2007) 480–485.

[11] Lee, K.J., Barber, D.C., *Use of forward projection to correct patient motion during SPECT imaging.* Phys Med Biol **43** (1998) 171–187.

[12] Chen, Q.s., Franken, P.R., Defrise, M., Jonckheer, M.H., Deconinck, F., *Detection and correction of patient motion in SPECT imaging.* J Nucl Med Technol **21**(4) (1993) 198–205.

[13] Fulton, R.R., Eberl, S., Meikle, S.R., Hutton, B.F., Braun, M., *A practical 3D tomographic method for correcting patient head motion in clinical SPECT.* IEEE Trans Nucl Sci **46**(3) (1999) 667–672.
[14] Kyme, A.Z., Hutton, B.F., Hatton, R.L., Skerrett, D.W., Barnden, L.R., *Practical aspects of a data-driven motion correction approach for brain SPECT.* IEEE Trans Med Imag **22**(6) (2003) 722–729.
[15] Schumacher, H., Fischer, B., *A new approach for motion correction in spect imaging.* In: Bildverarbeitung für die Medizin. Springer. (2007).
[16] Park, S.C., Park, M.K., Kang, M.G., *Super-resolution image reconstruction: a technical overview.* IEEE Signal Processing Magazine **20**(3) (2003) 21– 36.

2D Phase Unwrapping Problem

Ming Jiang
(joint work with Zhi-Quan Luo, Jin-Jun Xiao)

Phase unwrapping is a classical problem in many applications, such as optical interferometry, x-ray phase contrast imaging and tomography, MRI, and synthetic aperture radar, etc. Phase unwrapping problem is to restore the true phase from the measured phase which are wrapped and corrupted by noise. It is to estimate the true value φ from the following phase wrapping equation

$$\theta(x) = \mathcal{W}[\varphi(x) = [\varphi(x)]^{\mathcal{W}} = \varphi(x) \mod (2\pi), \quad x \in \Omega, \tag{1}$$

where φ is the true phase, $\mathcal{W}$ is the wrapping operator, θ is the wrapped phase in the principal range $(-\pi, \pi]$, Ω is a domain in $\mathbf{R}^n$. The wrapping operator, $\mathcal{W}$, wraps its argument into one principle range, typically, $(-\pi, \pi]$ after 2π modulation. The wrapping process results in discontinuities in the measured phase values. Noise and aliasing are other difficulties for phase unwrapping. Phase unwrapping is essentially ill-posed.

Methods for phase unwrapping depend on how the true phase gradient $\nabla\varphi$ is extracted or estimated from the phase wrapping equation (1) [3]. For $n = 1$, when the Itoh's condition [5]

$$-\pi < \nabla\varphi(x) \leq \pi, \quad x \in \Omega, \tag{2}$$

holds, the following estimate of the derivative of the true phase is utilized

$$\varphi'(x) = \mathcal{W}[\theta'(x)], \quad x \in \Omega. \tag{3}$$

In this case, the true phase can be restored simply by integration,

$$\varphi(x) = \int_{-\infty}^{x} \mathcal{W}[\theta'(t)]\, dt \quad x \in \Omega. \tag{4}$$

For $n \geq 2$, path integration is applied in (4). However, such an integration can be path dependent if there are curves with non-zero residues [3]. The residue of a closed curve C in Ω is defined as

$$\frac{1}{2\pi} \oint_C \nabla\varphi\, dC. \tag{5}$$

Therefore, it leads to non-unique results to restore the true phase by path integration, even if Itoh's condition is valid. To resolve this path dependent issue, branch cut or graph cut methods have been developed [4, 1]. Any path not intersecting the cuts can then be used for path integration.

Another important approach for phase unwrapping is by L^p norm minimization [3]. It is to restore the true phase by minimizing the following functional

$$\int_\Omega \|\nabla\varphi - \nabla\theta\|^p \, dx. \tag{6}$$

for $\varphi \in H_p^1(\Omega)$. $p = 2$ leads to a boundary value problem of the Poissonian equation. Zero residue condition can be incorporated as a constriant. Various regularization techniques and Bayesian frameworks are also reported.

In [8], we consider the 2D phase unwrapping problem and propose *a Maximum a Posteriori* (MAP) framework. Assuming a Gaussian prior for the true phase image, the MAP formulation leads to a quadratic integer minimization problem with the zero residue constraint. When the gradient of the true phase satisfies a relaxed Itoh's condition $\|\nabla\varphi\| < 2\pi$, the MAP formulation is reduced to a binary quadratic minimization problem. The latter can be efficiently solved by semidefinite relaxation (SDR). Numerical results demonstrate that the SDR approach significantly outperforms the methods based on L^1 or L^2 norm minimization.

There are several methods based on partial differential equations (PDE) [7], including some from L^p norm minimization [3]. In this talk, a new phase unwrapping method based on PDE is reported. Our method is based on another estimate of the gradient of the true phase. The phase wrapping equation can be equivalently written as

$$\mathbf{e}^{i\varphi(x)} = \mathbf{e}^{i\theta(x)} = u(x) + iv(x), \quad x \in \Omega, \tag{7}$$

where $u(x) = \cos\theta(x)$ and $v(x) = \sin\theta(x)$ for $x \in \Omega$. Although the wrapped phase usually contains discontinuities, its sine u and cosine v are of the same smoothness as the true phase. Computing gradients at both sides of (7), we obtain

$$i\mathbf{e}^{i\varphi}\nabla\varphi = \nabla u + i\nabla v. \tag{8}$$

It follows that

$$\nabla\varphi = -i\,(u - iv)\,(\nabla u + i\nabla v) = u\nabla v - v\nabla u. \tag{9}$$

Define an operator G as

$$G[\theta] = \cos\theta \cdot \nabla\,[\sin\theta] - \sin\theta \cdot \nabla\,[\cos\theta]\,, \tag{10}$$

which serves as another estimate of the gradient of the true phase, different from the estimate in (3). Computing divergences at both sides of (9), we obtain,

$$\Delta\varphi = u\Delta v - v\Delta u. \tag{11}$$

By (9) again, the outward normal derivative of φ at the boundary Γ of Ω is

$$\frac{\partial\varphi}{\partial n} = u\frac{\partial v}{\partial n} - v\frac{\partial u}{\partial n}. \tag{12}$$

Then the true phase can be restored by solving the following boundary value problem (BVP)

$$\begin{cases} \Delta\varphi = u\Delta v - v\Delta u, & x \in \Omega, \\ \dfrac{\partial\varphi}{\partial n} = u\dfrac{\partial v}{\partial n} - v\dfrac{\partial u}{\partial n}, & x \in \Gamma. \end{cases} \tag{13}$$

The estimate in (9) was reported in [2]. A BVP same as (13) was proposed in [6]. However, a zero Neumann boundary condition was applied in [6].

When smoothness of involved terms holds, it can be proved that solutions of the BVP (13) exist and are subject to arbitrary constant shifts. The BVP (13) is the Euler equation for the following functional

$$K(\varphi) = \frac{1}{2}\int_\Omega \|\nabla\varphi - G[\theta]\|^2\, dx, \tag{14}$$

for $\varphi \in H^1(\Omega)$. Hence, minimizing $K(\varphi)$ for $\varphi \in H^1(\Omega)$ is equivalent to finding a least-squares solution for the first order PDE (9). To confine the solutions from arbitrary constant shifts from solving the BVP (13) or equivalently the variational problem (14), we add another term to K as follows

$$K_\lambda(\varphi) = \frac{1}{2}\int_\Omega \|\nabla\varphi - G[\theta]\|^2\, dx + \frac{\lambda}{2}\int_\Omega \left|\mathbf{e}^{i\varphi} - \mathbf{e}^{i\theta}\right|^2\, dx, \tag{15}$$

to push solutions to be subject to shifts of integer multiples of 2π, provided that λ is small. The following is one representative simulation result of our proposed method.

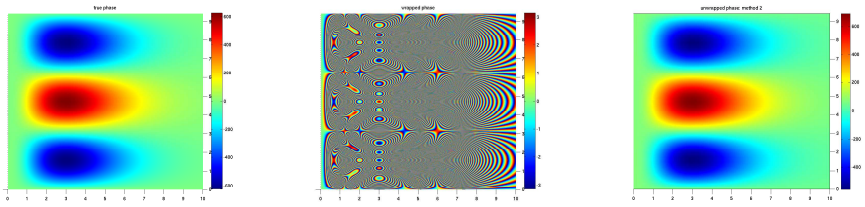

(a) True Phase (b) Wrapped Phase (c) Unwrapped Phase

FIGURE 1. Result obtained by solving the BVP for the functional (15).

REFERENCES

[1] J. M. Bioucas-Dias and G. Valadao. *Phase unwrapping via graph cuts*, IEEE Trans. on Image Processing **16** (2007), 698–709.

[2] G. Fornaro, G. Franceschetti, and R. Lanari. *Interferometric sar phase unwrapping using green's formulation*, IEEE Trans. on Geoscience and Remote Sensing **34** (1996), 720–727.

[3] D. C. Ghiglia and M. D. Pritt. *Two-dimensional phase unwrapping: theory, algorithms, and software*, Wiley, New York, 1998.

[4] R. M. Goldstein, H. A. Zebker, and C. L. Werner. *Satellite radar interferometry - two-dimensional phase unwrapping*, Radio Science, **23** (1988), 713–720.

[5] K. Itoh. *Analysis of the phase unwrapping algorithm*, Applied Optics, textbf21 (1982), 2470.
[6] O. Marklund. *An anisotropic evolution formulation applied in 2-d unwrapping of discontinuous phase surfaces*, IEEE Trans. on Image Processing, **10** (2001), 1700–1711.
[7] S. M. H. Song, S. Napel, N. J. Pelc, and G. H. Glover. *Phase unwrapping of mr phase images using poisson equation*, IEEE Trans. on Image Processing, **4** (1995), 667–676.
[8] J-J. Xiao, Z-Q. Luo, and M. Jiang. *Two-dimensional phase unwrapping using semidefinite relaxation*, IEEE International Conference on Acoustics, Speech, and Signal Processing, (2009), 1105–1108.

Exact shape-reconstruction by one-step linearization in electrical impedance tomography

Bastian Harrach
(joint work with Jin Keun Seo)

The goal of electrical impedance tomography (EIT) is to produce spatial and temporal images of the conductivity within an electrically conducting subject such as the human body from measurements of boundary voltage data resulting from the injection of electrical currents. The mathematical problem behind EIT is how to reconstruct the coefficient $\sigma(x)$ in the elliptic partial differential equation

$$\nabla \cdot \sigma(x) \nabla u(x) = 0, \quad x \in \Omega, \tag{1}$$

from knowledge of all possible Dirichlet and Neumann boundary values, $u|_{\partial\Omega}$ and $\sigma \partial_\nu u|_{\partial\Omega}$ of the solutions. We thereby assume that $\sigma \in L^\infty_+(\Omega)$ where $\Omega \subset \mathbb{R}^n$, with $n \geq 2$, is a bounded domain with smooth boundary $\partial\Omega$ and outer normal ν. Knowing the set of all possible Dirichlet and Neumann boundary values is equivalent to knowing the Neumann-to-Dirichlet operator

$$\Lambda(\sigma): \ g \mapsto u|_{\partial\Omega},$$

where u solves (1). For fixed σ, this is a compact and self-adjoint linear operator from $L^2_\diamond(\partial\Omega)$ to $L^2_\diamond(\partial\Omega)$, where the subscript "$\diamond$" denotes the subspace of functions with vanishing integral mean on $\partial\Omega$.

The most widely used reconstruction algorithms for EIT rely on linearizing the forward mapping $\Lambda: \ \sigma \mapsto \Lambda(\sigma)$ around some reference conductivity σ_0. Then the linear equation

$$\Lambda'(\sigma_0)\kappa = \Lambda(\sigma) - \Lambda(\sigma_0), \tag{2}$$

is solved to obtain an approximation $\kappa \approx \sigma - \sigma_0$. $\Lambda'(\sigma_0)$ denotes the Fréchet-derivative of Λ evaluated at σ_0.

Herein, we report on the crucial question of how close the thus reconstructed κ is to the true conductivity change $\sigma - \sigma_0$. We sketch our recent result [4] that shows that κ and $\sigma - \sigma_0$ have the same (outer) support, no matter how large $\sigma - \sigma_0$ is. The *outer* support "$\mathrm{supp}_{\partial\Omega}$" is, roughly speaking, the support together with all regions that cannot be reached from $\partial\Omega$, cf. [9, 2] for the origins of this concept.

Theorem 1. [4, Corollary 3.5(c)] *Let σ and σ_0 be piecewise-analytic. If there exists an exact piecewise-analytic solution κ of the linearized equation (2) then* $\operatorname{supp}_{\partial\Omega}(\sigma-\sigma_0) = \operatorname{supp}_{\partial\Omega}\kappa$.

Furthermore, for all points on the boundary of $\operatorname{supp}_{\partial\Omega}$ *that have a neighbourhood in* $\operatorname{supp}_{\partial\Omega}$ *in which σ, σ_0 and κ are continuous, it holds that*

$$\frac{\sigma_0}{\sigma}(\sigma-\sigma_0) \leq \kappa \leq \sigma-\sigma_0, \tag{3}$$

where the evaluations are taken from inside $\operatorname{supp}_{\partial\Omega}$.

Sketch of the proof. The proof of the theorem relies on a monotony argument together with the technique of localized potentials derived by one of the authors in [1]. The monotony relation is frequently being used in some form or another in the EIT-literature, cf. [6, 7, 5, 3]. In the sense of quadratic forms on $L^2_\diamond(\partial\Omega)$, it holds that ([4, Lemma 2.1])

$$\Lambda'(\sigma_0)(\sigma-\sigma_0) \leq \Lambda(\sigma)-\Lambda(\sigma_0) \leq \Lambda'(\sigma_0)\left(\frac{\sigma_0}{\sigma}(\sigma-\sigma_0)\right).$$

Using the assumption that $\Lambda'(\sigma_0)\kappa = \Lambda(\sigma)-\Lambda(\sigma_0)$ and writing out the quadratic forms, we deduce that

$$\int_\Omega (\sigma-\sigma_0)|\nabla u_0|^2 \mathrm{d}x \geq \int_\Omega \kappa|\nabla u_0|^2\mathrm{d}x \geq \int_\Omega \frac{\sigma_0}{\sigma}(\sigma-\sigma_0)|\nabla u_0|^2\mathrm{d}x \tag{4}$$

holds for all solutions u_0 of the EIT equation (1) with reference conductivity σ_0.

Hence, in order to obtain a relation between κ and $\sigma-\sigma_0$ we have to control the squares (of gradients of solutions) $|\nabla u_0|^2$, which physically correspond to the electrical energy of the potentials u_0. In [1, Theorem 2.7], one of the authors has shown that these squares can be controlled in quite a general way (the so-called technique of localized potentials). It is possible to make the energy of u_0 arbitrarily large in some subset of Ω, while at the same time making it arbitrarily small in another part. The only restriction is that there must exist a connection between the large energy part and (a part of) the boundary $\partial\Omega$ that does not intersect the small energy part. The left side of figure 1 shows a sketch of what is possible to achieve. There exists a sequence of potentials $u_0^{(k)}$ such that (the L^2-norm of) $\nabla u_0^{(k)}$ tends to infinity in the small circle at the end of the curved domain and, at the same time, $\nabla u_0^{(k)}$ tends to zero outside the curved domain. Note that the curved domain connects the small circle to a part of the boundary.

We can now use these *localized potentials* to deduce the theorem from the monotony relation (4). Assume that $\operatorname{supp}_{\partial\Omega}\kappa$ is not the same as $\operatorname{supp}_{\partial\Omega}(\sigma-\sigma_0)$. Then there must be some part of $\operatorname{supp}_{\partial\Omega}(\sigma-\sigma_0)$ which does not belong to $\operatorname{supp}_{\partial\Omega}\kappa$ (or vice versa) and, since this is the *outer* support, this part can be reached from the boundary. By analyticity arguments, we can assume that $\sigma-\sigma_0$ is either strictly positive or strictly negative there. Now we use a localized potential that is large on this overlapping part but small on all other parts of $\operatorname{supp}_{\partial\Omega}\kappa$ and $\operatorname{supp}_{\partial\Omega}(\sigma-\sigma_0)$, cf. the right side of figure 1, and obtain a contradiction to the monotony relation (4). With the same arguments we can show (3). □

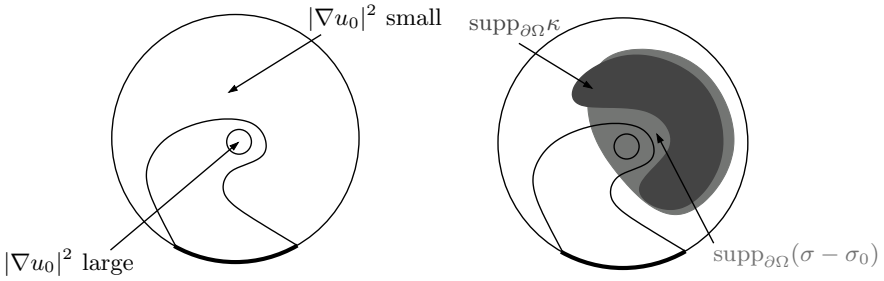

FIGURE 1. Sketch of the use of localized potentials.

Note that the theorem also implies that the Calderón-problem is uniquely solvable for piecewise-analytic conductivities (which is a famous result of Kohn and Vogelius [8]), and that the same arguments also show that the linearized Calderón-problem is uniquely solvable for piecewise-analytic conductivities (which was shown for piecewise polynomials in [10]).

For practical applications, there is a flaw in the formulation of this theorem. It is not clear whether an exact solution of the linearized equation exists. Even if it exists, it does not have to be piecewise analytic, and, even if it exists and it is piecewise-analytic, one would only be able to find an approximate solution in practice.

However, under an additional definiteness condition and taking a slightly more technical approach, the theorem and its proof can be extended to derive a globally convergent method to calculate the outer support by approximately solving (2). The details are given in [4].

REFERENCES

[1] B. Gebauer, *Localized potentials in electrical impedance tomography*, Inverse Probl. Imaging **2** (2008), 251–269.

[2] B. Gebauer and N. Hyvönen, *Factorization method and inclusions of mixed type in an inverse elliptic boundary value problem*, Inverse Probl. Imaging **2** (2008), 355–372.

[3] B. Harrach and J. K. Seo, *Detecting inclusions in electrical impedance tomography without reference measurements*, SIAM J. Appl. Math. **69** (2009), 1662–1681.

[4] B. Harrach and J. K. Seo, *Exact shape-reconstruction by one-step linearization in electrical impedance tomography*, SIAM J. Math. Anal., to appear.

[5] T. Ide, H. Isozaki, S. Nakata, S. Siltanen, and G. Uhlmann, *Probing for electrical inclusions with complex spherical waves*, Comm. Pure Appl. Math. **60** (2007), 1415–1442.

[6] H. Kang, J. K. Seo, and D. Sheen, *The inverse conductivity problem with one measurement: stability and estimation of size*, SIAM J. Math. Anal. **28** (1997), 1389–1405.

[7] A. Kirsch, *The factorization method for a class of inverse elliptic problems*, Math. Nachr. **278** (2005), 258–277.

[8] R. Kohn and M. Vogelius, *Determining conductivity by boundary measurements II. Interior results*, Comm. Pure Appl. Math. **38** (1985), 643–667.

[9] S. Kusiak and J. Sylvester, *The scattering support*, Comm. Pure Appl. Math. **56** (2003), 1525–1548.

[10] A. Lechleiter and A. Rieder, *Newton regularizations for impedance tomography: convergence by local injectivity*, Inverse Problems **24** (2008), 065009 (18pp)

Local SONAR inversion

Andreas Rieder
(joint work with Todd Quinto and Thomas Schuster)

One mathematical model for SONAR is the spherical mean transform that recovers a function in 3D from its means over spheres centered on a plane, (e.g., the surface of the ocean). Indeed, assume the acoustic wave is excited at point $\mathbf{z} \in \mathcal{P} = \{(\mathbf{z}', 0) \colon \mathbf{z}' \in \mathbb{R}^2\}$. Then, the resulting acoustic pressure field $u(t; \mathbf{x})$ in $\mathbf{x} \in \mathbb{R}^3$ (x_3 is the depth coordinate) at time $t \geq 0$ is governed by the acoustic wave equation

$$\Delta_{\mathbf{x}} u - \frac{1}{\nu^2}\, \partial_t^2 u = -\delta(\mathbf{x} - \mathbf{z})\delta(t)$$

where $\nu = \nu(\mathbf{x})$ is the *speed of sound*.

The corresponding inverse problem is to reconstruct ν from the backscattered (reflected) field u_{s} observed on the plane $\mathcal{P}$ for all times $t > 0$. Cohen and Bleistein [1] assumed ν to be a slight perturbation of a constant background velocity c:

$$\frac{1}{\nu^2(\mathbf{x})} = \frac{1 + n(\mathbf{x})}{c^2}$$

with an acoustic profile $n(\mathbf{x})$ whose absolute value being significantly less than 1. Using the fundamental solution of the wave equation with constant sound speed together with a linearization they obtained that

$$\mathbf{R} n\Big(\mathbf{z}', \frac{c\tau}{2}\Big) = -4c^2 \int_0^\tau (\tau - t) u_{\mathrm{s}}(t, \mathbf{z})\, \mathrm{d}t$$

where τ is the observation period and

$$\mathbf{R} f(\mathbf{z}', r) := \frac{1}{4\pi\, r^2} \int\limits_{S^2} f(\mathbf{z}' + r\xi, r\eta) \mathrm{dS}(\xi, \eta)$$

denotes the *spherical mean transform* mapping functions to their means over spheres centered at $(\mathbf{z}', 0)$ with radius $r > 0$.

Obviously, functions being odd with respect to x_3 cannot be recovered as all their spherical means vanish. Therefore, we restrict our investigation to functions in $\mathcal{C}^\infty_{0,\mathrm{even}}(\mathbb{R}^3)$, the space of even, infinitely differentiable functions with compact support. Those functions can be recovered by Klein's [2] inversion formula

$$f = \frac{1}{2\pi} (I \otimes I \otimes H) \sqrt{\Delta}\, \mathbf{R}^*_\partial \mathbf{R} f, \quad f \in \mathcal{C}^\infty_{0,\mathrm{even}}(\mathbb{R}^3),\,^1$$

where Δ is the three-dimensional *Laplacian*,

$$\mathbf{R}^*_\partial g(\mathbf{x}) = \int_{\mathbb{R}^2} \partial_{x_3} g\Big(\mathbf{z}', \sqrt{|\mathbf{z}' - \mathbf{x}'|^2 + x_3^2}\Big) \mathrm{d}\mathbf{z}'$$

is the *backprojection operator*, and H is the *Hilbert transform*.

Klein's formula requires complete data, that is, $\mathbf{R} f$ has to be known on all of $\mathbb{R}^2 \times [0, \infty)$. Obviously, complete data can never be recorded and applying the

[1] By duality the inversion formula may be extended to special classes of distributions.

inversion formula to incomplete data results in the typical artefacts corrupting the inversion.

To overcome these drawbacks we replace the non-local operations H and $\sqrt{\Delta}$ in Klein's formula by I and Δ, respectively. Furthermore, we cut off the data with respect to large radii (so that we can interchange integration and differentiation in $\mathbf{R}^*_{\partial}$). Instead of f we propose to recover Λf from $\mathbf{R}f$ by

$$\Lambda f := \partial_{x_3} \Delta \mathbf{R}^* \Phi \mathbf{R} f$$

where $\mathbf{R}^*$ is as above without derivative ∂_{x_3} and

$$\Phi g(\mathbf{x}, r) = \varphi(r) g(\mathbf{x}, r)$$

with a smooth cutoff function φ being 1 on a compact set around the origin and being 0 for radii larger than, say, a chosen $r_{\max}$.

Lemma: *The operator Λ is pseudodifferential of order 1 with top order symbol*

$$\sigma(\mathbf{x}, \xi) = -\imath\pi \, \varphi\!\left(\frac{x_3}{|\xi_3|} \, |\xi| \right) \operatorname{sgn}(\xi_3) \, |\xi|, \quad \xi \in \mathbb{R}^3, \ x_3 > 0.$$

As such $\Lambda \colon H^s_{\mathrm{c}}(\mathbb{R}^3) \to H^{s-1}_{\mathrm{loc}}(\mathbb{R}^3_{x_3>0})$ is continuous for any $s \in \mathbb{R}$.

The symbol tells us that Λ basically behaves like the differential operator $-\partial_{x_3}$. Thus, f and Λf share the same singularities (to be precise: they share the same singular support).

The numerical evaluation of Λ needs to be stabilized. To this end we follow ideas of the approximate inverse [3]. Instead of computing $\Lambda f(\mathbf{p})$, $\mathbf{p} \in \mathbb{R}^3_{x_3>0}$, directly we like to recover its smoothed version

$$\langle \Lambda f, e_{\mathbf{p},s,k} \rangle_{L^2(\mathbb{R}^3)}$$

where

$$e_{\mathbf{p},s,k}(\mathbf{x}) = \frac{\Gamma(k+5/2)}{\pi^{3/2}\,\Gamma(k+1)\,s^{3+2k}} \begin{cases} (s^2 - d^2)^k & : \ d < s, \\ 0 & : \ d \geq s, \end{cases} \qquad d = |\mathbf{x} - \mathbf{p}|,$$

is a mollifier with $s, k > 0$,

$$\int_{\mathbb{R}^3} e_{\mathbf{p},s,k}(\mathbf{x}) \, \mathrm{d}\mathbf{x} = 1 \quad \text{and} \quad \operatorname{supp} e_{\mathbf{p},s,k} = B_s(\mathbf{p}).$$

The parameter $s > 0$ scales the mollifier and plays the role of a regularization parameter: the larger s the smoother the reconstruction. Note that k is only a design parameter.

In the following theorem we give analytically a reconstruction kernel allowing the computation of $\langle \Lambda f, e_{\mathbf{p},s,k} \rangle_{L^2(\mathbb{R}^3)}$ from the spherical means of f.

Theorem: *We have that*

$$\langle \Lambda f, e_{\mathbf{p},s,k} \rangle_{L^2(\mathbb{R}^3)} = \langle \mathbf{R}f, \psi_{\mathbf{p},s,k} \rangle_{L^2(\mathbb{R}^2 \times [0,\infty[, r^2 \mathrm{d}\mathbf{z}' \mathrm{d}r)}$$

with reconstruction kernel

$$\psi_{\mathbf{p},s,k}(\mathbf{z}',r) = -\varphi(r)\,\frac{C_{k,s}\,k\,p_3\,A^{k-2}}{L}\left[(2k+1)A\left[\frac{1}{Lk}\left(k-2+\frac{B}{2rL}\right)-\frac{1}{r}\right]\right.$$
$$\left.+\,2(k-1)s^2\left[\frac{1}{r}-\frac{1}{L(k-1)}\left(k-3+\frac{B}{2rL}\right)\right]\right]$$

for $r \in [L-s, L+s]$ *where*

$$L = |(\mathbf{z}',0)-\mathbf{p}|, \quad A = s^2-(L-r)^2 \quad \textit{and} \quad B = (r+L)^2-s^2.$$

For $r \notin [L-s, L+s]$*:* $\psi_{\mathbf{p},s,k}(\mathbf{z}',r) = 0$.

First numerical experiments showed that singularities of f, which are in principle visible from the limited data set, can be stably recovered.

References

[1] J. K. Cohen, N. Bleistein *Velocity inversion procedure for acoustic waves*, Geophysics **44** (1979), 1077–1087.

[2] J. Kein, *Mathematical Problems in Synthetic Aperture Radar*, PhD thesis, University of Münster, Germany (2004).

[3] A. K. Louis, *Approximate inverse for linear and some nonlinear problems*, Inverse Problems **12** (1996), 175–190.

Synthetic focusing in Acousto-Electric Tomography

Leonid Kunyansky

(joint work with P. Kuchment)

Electrical Impedance Tomography (EIT) is known as a harmless and inexpensive imaging modality [2]. Unfortunately, it suffers from low resolution and instability (see e.g. [3]). Recently, it was proposed [9] to combine the traditional EIT measurements with simultaneous perturbation of the medium by a focused acoustic beam. Such a technique, called Acousto-Electric Tomography (AET), is based on the recent discovery that tissue conductivity can be changed by application of acoustic pressure [7, 8]. It has been understood [1, 5] that if one could focus the ultrasound on a small spot inside the body, knowledge of this location would have a stabilizing effect on the reconstruction in otherwise highly unstable EIT.

Since perfect focusing of acoustic waves is almost impossible to achieve in practice, we propose an alternative approach where the medium is perturbed by a series of spherical acoustic fronts of varying radii and with centers lying outside of the object. Then the changes in the electric potential corresponding to perfectly focused perturbations are synthesized from the measurements made using realistic (spherical) acoustic waves. As explained below, such a synthesis is achieved by the inversion of the spherical mean Radon transform. Our numerical experiments confirm the efficiency of such "synthetic" focusing and show vast improvement in stability and image resolution as compared to EIT.

Formulation of the problem. The propagation of the electrical currents in a conductive medium is governed by the divergence equation

$$\nabla \cdot \sigma(x) \nabla u(x) = 0, \tag{1}$$

where $\sigma(x)$ is the conductivity and $u(x)$ is the electric potential, $x \in \Omega$. Let us assume that $\sigma - 1$ is compactly supported within region Ω, and that $\sigma(x) = 1$ in the neighborhood of the boundary $\partial\Omega$. We also assume that the currents $\psi(x) = \sigma \frac{\partial}{\partial n} u(x)$ through the boundary are fixed and the values of the resulting potential are measured on the boundary $\partial\Omega$.

The acoustic wave propagating through the object slightly perturbs the conductivity $\sigma(x)$. Following the observations made in [7, 8] we assume that the perturbation is proportional to the local value of the conductivity; thus, the perturbed conductivity $\sigma^{new}(x)$ equals to $\sigma(x)\exp(\eta(x))$ where $|\eta(x)| \ll 1$ and is compactly supported. Let $u^{new}(x) = u(x) + w(x)$ be the potential corresponding to the perturbed conductivity $\sigma^{new}(x)$ and $w(x)$ be the perturbation thereof. Then, by linearizing the problem about the unperturbed solution $u(x)$ we find that $w(x)$ satisfies equation

$$\nabla \cdot \sigma(x) \nabla w(x) = -\sigma(x) \nabla u(x) \cdot \nabla \eta(x)$$

subject to the homogeneous Neumann boundary conditions. Since the values of $u(x)$ and $u^{new}(x)$ are measured on the boundary, the Dirichlet data for $w(x)$ are known.

Perfect focusing. Let us first consider the case of a perfectly focused perturbation $\eta(x)$ that can be approximated by the Dirac δ-function $\delta_y(x) = \delta(x - y)$. Let us denote the corresponding solution by w_{δ_y}. Then

$$\nabla \cdot \sigma(x) \nabla w_{\delta_y}(x) \approx -\sigma(y) \nabla u(y) \cdot \nabla \delta(x - y).$$

Our immediate goal is to reconstruct $\nabla u(y)$ from the values of w_{δ_y} on $\partial\Omega$. To this end we introduce functions $h_1(x)$ and $h_2(x)$ defined on $\partial\Omega$ and orthogonal to a constant, and we define measurement functionals $M_\delta(y, h_j)$ as follows

$$M_\delta(y, h_j) = \int_{\partial\Omega} w_{\delta_{x_0}}(z) h_j(z) dz, \qquad j = 1, 2.$$

One can show that

$$M_\delta(y, h_j) = -\sigma(y) \nabla u(y) \cdot \nabla H_j(y), \qquad j = 1, 2. \tag{2}$$

where functions $H_1(x)$, $H_2(x)$ are the solutions of the divergence equation

$$\nabla \cdot \sigma(x) \nabla H_j(x) = 0, \tag{3}$$

subject to the Neumann boundary conditions $\frac{\partial}{\partial n} H_j(y) = h_j(y)$ on $\partial\Omega$, $j = 1, 2$.

Now, if some initial approximation to $\sigma(y)$ is known (one can start, for example, with initial guess $\sigma(x) = 1$), functions $H_1(x)$, $H_2(x)$ can be computed as solutions to (3), and, for a fixed y, values of $\nabla u(y)$ can be found from the system of two linear equations (2). When $\nabla u(y)$ is reconstructed on a computational grid on Ω

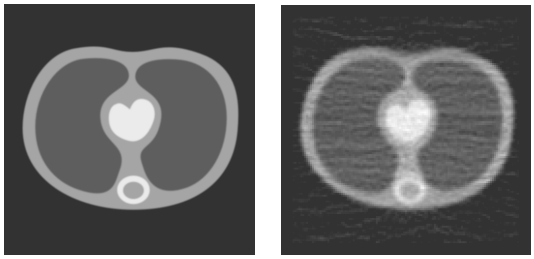

(a) (b)

FIGURE 1. Example of a reconstruction: (a) phantom (b) reconstruction

by repeating the above procedure at all the nodes of the grid, the conductivity can be computed by solving the transport equation

$$\nabla u(y) \cdot \nabla \ln \sigma(y) = -\nabla \cdot \nabla u(y). \tag{4}$$

Once an approximation to $\sigma(x)$ is obtained, one can compute a better approximation to H_j's, and thus to $\sigma(x)$. In our simulations such iterations converged not only for $\sigma(x)$ close to 1, but even when $\sigma(x)$ significantly varied across Ω.

Synthetic focusing. Unfortunately, creating physically a δ-like perturbation within the body of interest is nearly impossible. It is much easier to measure functionals corresponding to time-harmonic waves or propagating spherical fronts with centers lying outside the body. We thus propose to synthesize the measurements $M_\delta(y,h)$ corresponding to δ-perturbations from the data obtained using realistic acoustic waves. Such a synthesis is possible due to the smallness of the acousto-electric effect, which justifies the use of the linearized model of the perturbations.

Suppose perturbation $\eta_{z,r}(x)$ approximates the spherical front of radius r centered at z, i.e. $\eta_{z,r}(x) \approx \delta(r - |z-x|)$. Let us denote the corresponding measurement functional by $M_S(z,r,h)$. Since a spherical front can be represented as a linear combination of delta functions $\delta(y-x)$,

$$\eta_{z,r}(x) \approx \int_{S^1} \delta(z + r\varpi - x) d\varpi = \int_{S^1} \delta(x-y) \mid_{y=z+r\varpi} d\varpi,$$

then, by the linearity of the measurement functional

$$M_S(z,r,h) = \int_{S^1} M_\delta(z + r\varpi, h) d\varpi.$$

In other words, the measured data $M_S(z,r,h)$ are equal to the spherical mean transform of $M_\delta(y,h)$! Therefore, if one measures $M_S(z,r,h)$ for all $z \in S(R,0)$ and all $r \in [0,2R]$, the electric response to the δ-like perturbations $M_\delta(y,h)$ can be reconstructed from $M_S(z,r,h)$ using known 2-D inversion formulas [4, 6].

An example of reconstruction is presented in Figure 1. The measurements were simulated using acoustical perturbations in the form of spherical fronts. There were 320 acoustical sources and 257 fronts of varying radii for each source. The

potential was "measured" on each side of a square domain, at 513 points per side. We added 15% noise (in L^2 norm) to each point value of the potential.

There are considerable differences between our methods and results, and those of [1]. In the latter work, under the assumption of a perfectly focused acoustic perturbation the problem is reduced to a solution of a non-linear equation. The present work uses realistic measurements; then, by exploiting the smallness of acousto-electric effect the problem is solved by a repeated solution of linear transport equation (4).

References

[1] H. Ammari, E. Bonnetier, Y. Capdeboscq, M. Tanter, and M. Fink, *Electrical impedance tomography by elastic deformation*, SIAM J. Appl. Math. **68** (2008), 1557–1573.

[2] D. C. Barber, B. H. Brown, *Applied potential tomography*, J. Phys. E.: Sci. Instrum. **17**(1984), 723–733.

[3] L. Borcea, *Electrical impedance tomography*, Inverse Problems **18** (2002), R99–R136.

[4] D. Finch, M. Haltmeier, and Rakesh, *Inversion of spherical means and the wave equation in even dimensions*, SIAM J. Appl. Math. **68** (2007), 392–412.

[5] P. Kuchment and L. Kunyansky, *Synthetic focusing in ultrasound modulated tomography*, to appear in Inverse Problems and Imaging, (2010).

[6] L. A. Kunyansky, *Explicit inversion formulae for the spherical mean Radon transform*, Inverse Problems **23** (2007), pp. 373–383.

[7] B. Lavandier, J. Jossinet and D. Cathignol, *Quantitative assessment of ultrasound-induced resistance change in saline solution*, Medical & Biological Engineering & Computing **38** (2000), 150–155.

[8] B. Lavandier, J. Jossinet and D. Cathignol, *Experimental measurement of the acousto-electric interaction signal in saline solution*, Ultrasonics **38** (2000), 929–936.

[9] H. Zhang and L. Wang, *Acousto-electric tomography*, Proc. SPIE 5320, (2004),145–149.

Ultrasound Tomography for Breast Cancer Screening: From Theory to Applications

Jovanović, Ivana

(joint work with Martin Vetterli)

One woman in two receives a breast cancer scare in her lifetime. Today's gold standard for breast cancer screening is mammography. It has been shown to reduce the mortality rate by up to 35%. However, mammography involves transmission of x-rays, which is potentially harmful. It is also known that mammography generates many abnormal findings not cancer related, leading to a false positive rate that can be as high as 80%, and a high false negative rate that is up to 50% for women with dense breasts.

Ultrasound tomography is a promising modality for breast cancer screening. The speed of sound propagation and its attenuation could help detect cancer and differentiate benign from cancer masses. Unlike the x-rays, ultrasound is deviated by refraction and distorted by inhomogeneities in tissue. For a long time, the propagation of ultrasound and the non-linear inverse problem that had to be solved were difficult tasks. Today, with enhanced computing power and advances in

transducers technologies, the future of ultrasound tomography is bright and the prospects are showing great promise.

The ultimate goal of this research is to improve the quality of ultrasound imaging in terms of its accuracy and image resolution aimed at creating an easy, safe, non-ionizing, reliable, operator independent and inexpensive method for breast cancer screening.

In this work we examine the inverse problem behind the ultrasound tomography. The subjects related to the signal acquisition (i.e., time-of-flight estimation) and image reconstruction (i.e., inversion) are addressed in more details in the following.

1. Time-of-flight estimation

A number of reconstruction methods in ultrasound tomography rely on a simplified model for sound propagation, the so called ray model. It assumes that the inhomogeneities in the medium are much larger compared to the probing wavelength. In this case, the only information needed to reconstruct the sound speed image are time-of-flight measurements, i.e. the time taken by a sound wave to propagate from a transmitter to a receiver.

To increase the SNR in the received signal and to annihilate the reflections and late arrivals, we propose to use a beamforming technique [1]. This technique allow better time-of-flight estimation even in very inhomogeneous and absorbent tissue and shows to overcome some of the ultrasound artifacts due to the simplified model for sound propagation.

2. Inversion

In [2], we designed a bent-ray tomography reconstruction algorithm. It involves solving a non-linear system of equations. The main difficulty of this kind of algorithms is to ensure the convergence and robustness to noise. To solve this problem we propose a non linear conjugate gradient method. First, the gradient is derived using Fermat's principle. Then, the optimal step is found using the backtracking line search. This approach is guaranteed to converge to a local minimum of the cost function. Moreover, the method has the potential to easily incorporate regularity constraints such as sparsity as a priori information on the model. Although the reconstruction involves solving a non-linear problem, this method has a reasonable complexity.

3. Regularization

The medical images, whether they represent the sound speed, the attenuation or some other parameter, are not random images and they have a certain structure and common features. For example, the variation of the unknown parameter is bounded and the changes are mostly smooth, which gives a possibility to exploit these *a priori* assumptions to regularize the image reconstruction. We propose to use an inverse method based on sparsity. The idea is to find a transform that sparsifies the image. This concept is know as Compressed Sensing [3, 4]. By assuming that the image to be reconstructed is sparse in an appropriate set of

bases the measurements can be used in more efficient way. This can increase the resolution of the image. The preliminary results in [5, 8, 9] show that this approach overcomes the limitations of classical tomography sampling.

Besides the standard image bases like wavelets we also propose to reconstruct images by searching for a sparse image representation in an overcomplete dictionary that is adapted to the properties of ultrasound images [7]. This dictionary is learned from high resolution MRI breast scans using an unsupervised dictionary learning method described in [6]. The proposed dictionary-based regularization method significantly improves the quality of reconstructed breast ultrasound images. It outperforms the wavelet-based reconstruction and the l_2-norm minimization, on both numerical and *in vivo* data.

4. Conclusions and Future Work

It is safe to envision that with the development of more sophisticated acquisition and inversion techniques ultrasound imaging will become a routine and in some cases irreplaceable imaging technique in medicine. The next technological step is the full wave equation inversion method. It will allow to reconstruct breast structure with accuracy higher than that reported for bent ray model and comparable to that provided by MRI. Our preliminary results in [10] are encouraging.

References

[1] I. Jovanović, A. Hormati, O. Roy, and M. Vetterli, "Acoustic Tomography Apparatus and Method," Patent US61/080,358, 2008.

[2] A. Hormati, I. Jovanović, O. Roy, and M. Vetterli, "Robust Ultrasound Travel-time Tomography Using the Bent-Ray Model," in *SPIE Medical Imaging*, 2010.

[3] D. L. Donoho, "Compressed sensing," *IEEE Trans. on Information Theory*, vol. 52, no. 4, 2006.

[4] E. J. Candes, J. Romberg, and T. Tao, "Robust uncertainty principles: exact signal reconstruction from highly incomplete frequency information," *IEEE Trans. on Information Theory*, vol. 52, no. 2, 2006.

[5] M. Lustig, D. Donoho, and J. M. Pauly, "Sparse MRI: The application of compressed sensing for rapid MR imaging," *Magnetic Resonance in Medicine*, vol. 58, no. 6, pp. 1182 – 1195, 2007.

[6] Olshausen B. A. and Field D. J., "Emergence of simple-cell receptive field properties by learning a sparse code for natural images," *Nature*, vol. 381, no. 6583, pp. 607–609, 1996.

[7] I. Tosić, I. Jovanović, P. Frossard, M. Vetterli, and N Durić, "Ultrasound tomography image reconstruction with learned dictionaries," in *IEEE Intern. Conf. on Acous., Speech, and Signal Proces.*, 2010.

[8] I. Jovanović, A. Hormati, L. Sbaiz, and M. Vetterli, "Efficient and Stable Acoustic Tomography Using Sparse Reconstruction Methods," in *19th International Congress on Acoustics*, 2007.

[9] I. Jovanović, L. Sbaiz, and M. Vetterli, "Tomographic approach for parametric estimation of local diffusive sources and application to heat diffusion," in *IEEE International Conference on Image Processing*, 2007.

[10] O. Roy, I. Jovanović, A. Hormati, R. Parhizkar, and M. Vetterli, "Sound Speed Estimation Using Wave-based Ultrasound Tomography: Theory and GPU Implementation," in *Proceedings of the SPIE Medical Imaging*, 2010.

A new reconstruction method for inverse medium scattering for Maxwell's equations

A. Lakhal

We present a new method to solve inverse scattering problems for the full three-dimensional time-harmonic Maxwell's model. The goal here is to determine the electromagnetic properties of an unknown inhomogeneous object using near-field measurements of scattered waves for multiple illuminations at a fixed frequency. Maxwell's equations are equivalently formulated as a coupled system of integro-differential equations for the contrast source. We use the concept of generalized induced source (GIS) to recast the intertwined vector equations in Maxwell' s model into decoupled scalar scattering problems. We apply the localized nonlinear approximation due to Habashy and co-workers. In this framework, we derive a uniqueness result for determining the contrast function and develop a fast reconstruction method based on Kaczmarz' algorithm.

1. Formulation of the problem

We consider electromagnetic scattering in inhomogeneous media for a time-harmonic regime at a fixed frequency $\omega > 0$. In the sequel, we omit the time-dependence $e^{-i\omega t}$, with $i^2 = -1$, in the field notation and only consider the space variable.

In a homogeneous background with dielectric constant $\varepsilon_0 > 0$ and magnetic permeability $\mu_0 > 0$, let a scattering object be laying within a bounded domain $\Omega \subset \mathbb{R}^3$ with smooth boundary $\partial\Omega$. Furthermore, the medium is assumed to be nonmagnetic and isotropic with constitutive properties given as the electric contrast function

$$f := \left(1 - \varepsilon_0^{-1}(\varepsilon(x) + i\frac{\sigma(x)}{\omega})\right).$$

The functions $\varepsilon > 0$ and $\sigma \geq 0$ denote the electric permittivity and the electric conductivity, respectively. They are assumed to be smooth enough with compact support embedded in Ω..

We denote ∇ the nabla operator, $\nabla\times$ the curl operator, $\nabla\cdot$ or **div** the divergence operator. The operatrors $\times$ and $\cdot$ stand for the vector and scalar products in $\mathbb{R}^3$, respectively.

For each experiment, let an incident electromagnetic wave $(\mathbf{E}^{inc}, \mathbf{H}^{inc})$ impinge upon the scattering object and denote $(\mathbf{E}, \mathbf{H})$ the resulting total field. Then, the secondary or scattered fields $\mathbf{E}^s := \mathbf{E} - \mathbf{E}^{inc}$ and $\mathbf{H}^s := \mathbf{H} - \mathbf{H}^{inc}$ have to satisfy in $\mathbb{R}^3$ the time-harmonic Maxwell equations

$$\nabla \times \mathbf{H}^s + i\omega\, \varepsilon_0\, \mathbf{E}^s = \mathbf{J}\,, \tag{1}$$

$$\nabla \times \mathbf{E}^s - i\omega\, \mu_0\, \mathbf{H}^s = 0, \tag{2}$$

and fulfill, uniformly for $x/|x|$, $x \neq 0$, the Silver-Müller radiation condition

$$\lim_{|x|\to\infty} (\mathbf{H}^s \times x - |x|\mathbf{E}^s) = 0. \tag{3}$$

Hence, the scattered field is to behold as radiating from the induced electric current sources given as the volume densities

$$\mathbf{J} := i\varepsilon_0\omega f\mathbf{E}.$$

Let $k = \omega\sqrt{\varepsilon_0\mu_0}$ denote the wavenumber. Using the outgoing Green's function

$$g_k(x,y) = g_k(x-y) := \frac{1}{4\pi}\frac{e^{ik|x-y|}}{|x-y|},\ x \neq y,\ x,y \in \mathbb{R}^3,$$

for the Helmholtz operator $(\Delta + k^2)$ in $\mathbb{R}^3$, one may derive, (see *e.g.* [3]), the integro-differential equation

$$\mathbf{E}(x) = \mathbf{E}^{inc}(x) - k^2 \int_{\mathbb{R}^3} g_k(x,y)\,\mathbf{q}(y)\,dy - \nabla_x \int_{\mathbb{R}^3} g_k(x,y)\,\nabla\cdot\mathbf{q}(y)\,dy, \tag{4}$$

with the equivalent source $\mathbf{q} := f\mathbf{E}$.
Let $\mathcal{C}^n(\mathbb{R}^3)$ denote the set of $n-$ times continuously differentiable functions on $\mathbb{R}^3$ and $\mathcal{C}_0^n(\Omega)$ the set of $n-$ times continuously differentiable functions compactly supported in Ω. The scalar scattering operator A is defined for $q \in C_0(\Omega)$, as

$$Aq(x) := \int_\Omega g_k\,(x,y)\,q(y)\,dy, \quad x \in \mathbb{R}^3.$$

This operator corresponds to the scalar approximation of the Maxwell equations by the Helmholtz equation.

Definition 1.1. *The scattering operator* $\mathbf{T}$ *is defined for* $\mathbf{q} \in \mathcal{C}_0^1(\mathbb{R}^3)^3$ *as*

$$\mathbf{T}\,\mathbf{q}(x) = k^2 \int_{\mathbb{R}^3} g_k(x,y)\ \mathbf{q}(y)\,dy + \nabla_x \int_{\mathbb{R}^3} g_k(x,y)\,\mathbf{div}\,\mathbf{q}(y)\,dy,\ x \in \mathbb{R}^3. \tag{5}$$

To comprehend electric sources of currents and charges we generalized the concept of induced current source in [6]. As a consequence, we recasted the vector inverse source problem for Maxwell's equations into decoupled scalar problems for each component of the field. Indeed, it seems more appropriate to call this concept as generalized inverse source (GIS) rather than as scattering potential used before.

Definition 1.2. *The generalized induced source (GIS) is defined for* $\mathbf{q} \in \mathcal{C}^2(\mathbb{R}^3)^3$ *as*

$$\mathbf{P}\,\mathbf{q} = k^2\,\mathbf{q} + \mathbf{grad}\,(\mathbf{div}\,\mathbf{q}). \tag{6}$$

Lemma 1.3. *Let* Ω *be a bounded domain in* $\mathbb{R}^3$ *with a smooth boundary. It holds*

$$\mathbf{T} = A\,\mathbf{P} \quad on \quad \mathcal{C}_0^2(\Omega)^3. \tag{7}$$

Let $\mathbf{M}_\Gamma$ denote any measurement operator on some set $\Gamma \subset \mathbb{R}^3 \setminus \Omega$. In practice, one may measure the total field $\mathbf{E}(x)$, $x \in \Gamma$ for a given incident field $\mathbf{E}^{inc}$, the measurement operator denotes, abusively in this case, $\mathbf{M}_\Gamma\mathbf{E}^s(x) = \mathbf{E}(x) - \mathbf{E}^{inc}(x)$, $x \in \Gamma$, although $\mathbf{E}^s(x)$ is not directly measurable on Γ.
The inverse scattering is concerned with the problem:

"To the measured data $\mathbf{d}_j = -\mathbf{M}_\Gamma \mathbf{E}_j^s$, determine the contrast function f such that

$$\mathbf{M}_\Gamma \, \mathbf{T}(f \, \mathbf{E}_j) = \mathbf{d}_j$$

holds for all experiments j."
In this inverse problem, we have to overcome three major aspects of difficulty:

(1) The ill-posedness as a typical feature. It is here twofold since the inverse problem is under-determined and ill-conditioned. Since data are afflicted with unavoidable errors related to measurement conditions, we must apply a regularization to obtain a stable solution.
(2) The coupling between the equations modeling electromagnetic scattering, which involve integro-differential operators acting on vector fields with intertwined components. This apparently requires a simultaneous treatement of all equations of the system.
(3) Nonlinearity. Although the operator $\mathbf{T}$ is linear, the dependence of the field $\mathbf{E}_j$ on the contrast function f may be highly nonlinear.

2. Localized nonlinear approximation

Habashy *et. al.* [5], Torres-Verdin and Habashy [10, 11] used the localized nonlinear approximation to obtain significant improvement in comparison with Born- or Rytov-approximation, see [1] and the references therein.
In the vicinity of an observation point $x \in \Omega$, the contribution of the internal fields in the integral $\mathbf{T}(f \, \mathbf{E})(x)$ is amplified due to the singularity of the Green's kernel at x. Therefore, using the approximation $\mathbf{T}(f \, \mathbf{E})(x) \simeq \mathbf{T}(f \, I) \cdot \mathbf{E}(x)$ one may for nonmagnetic media simplify (dmInteq11) into

$$\mathbf{E} = \mathbf{E}^{inc} - \, \mathbf{T}(f \, I) \cdot \mathbf{E} \quad \text{on} \quad \Omega \tag{8}$$

with $I = (\delta_{ij} \, e_i \otimes e_j)_{1 \le i,j \le 3}$ denoting the identity tensor of order 2. It yields

$$\mathbf{E} = \mathbf{E}^{inc} - \mathbf{T}(\eta \, \mathbf{E}^{inc}) \quad \text{on} \quad \Omega \tag{9}$$

for the diagonalised source $\eta \, \mathbf{E}^{inc} := f \, \mathbf{E}$ with $\eta = \eta(f)$ satisfying

$$\eta I = fI - \eta \mathbf{T}(f \, I). \tag{10}$$

The nonlinear character of the inverse medium problem remains, as η depends implicitly on f, in contrast to the full linearization by Born- or Rytov-approximation. The price to compute the seeked contrast function f when we have η, is to solve Equation (10), which is well-posed. In the sequel, we consider linearly polarized transverse plane waves as incident electric field. We denote $x \cdot y = x^T y$ the scalar product of $x, y \in \mathbb{R}^3, |x| = \sqrt{x^T x}$, and $S^2 = \{x \in \mathbb{R}^3, |x| = 1\}$ the unit sphere in $\mathbb{R}^3$.

Lemma 2.1. *Let* $\mathbf{d} = \mathbf{d}_{\alpha,\beta} = -\mathbf{M}_\Gamma \mathbf{E}^s$ *with* $\mathbf{M}_\Gamma \mathbf{E}^s$ *being the scattered electric fields measured on the set* Γ *for transverse incident waves* $\mathbf{E}^{inc}(x) = \beta e^{ik\alpha^T x}$ *with* $(\alpha, \beta) \in S \subset (S^2)^2, \alpha^T \beta = 0$.
If $\mathbf{q} = \eta \, \mathbf{E}^{inc}$ *satisfies*

$$\mathbf{d} = \mathbf{T}(\eta \, \mathbf{E}^{inc}) \quad \textit{on } \Gamma, \tag{11}$$

then η *fulfills*

$$\beta^T \mathbf{d} = A\left(\beta^T \mathbf{E}^{inc}\left(k^2\eta + \beta^T \nabla^2 \eta \beta\right)\right). \tag{12}$$

Hence, we obtain a completely decoupled system of scalar equations.

3. Uniqueness

Under the localized nonlinear approximation, we show that from boundary measurements of the scattered fields for an incident direction α we can uniquely determine a filtered version of η for frequencies on the Ewald sphere with centre $k\alpha$ and radius k.

Theorem 3.1. *Let* $\eta \in \mathcal{C}_0^2(\Omega)$ *and let* η_{2k} *denote the low-pass filtered function with cut-off* $2k$ *of* η, *defined as*

$$\hat{\eta}_{2k}(\xi) = \begin{cases} \hat{\eta}(\xi) & \text{if} \quad |\xi| < 2k \\ 0 & \text{if} \quad |\xi| \geq 2k \end{cases}.$$

If $A_j\,\eta = 0$ *on* $\partial\Omega$ *for all* $j = j(\alpha,\beta)$, $(\alpha,\beta) \in S$, *then* $\eta_{2k} = 0$.

Theorem 3.1 confirms a well known fact that varying the directions of incidence may compensate under-determination.

4. Reconstruction algorithm

In practice, we have a finite number of elements in the set S with a total number $p..$ Let the measurement operator $\mathbf{M}_\Gamma$ be the trace mapping on the boundary $\Gamma = \partial\Omega$ of the bounded domain $\Omega \subset \mathbb{R}^3$. Let $S_p \subset \{(\alpha,\beta) \in (S^2)^2, \alpha^T\beta = 0\}$ be a finite set with p elements. For $j = j(\alpha,\beta) \in \{1,\cdots,p\}$ with $(\alpha,\beta) \in S_p$, let $\mathbf{E}^{inc}(x) = e^{ik\alpha^T x}\beta$, $\mathbf{d} = -\mathbf{M}_\Gamma \mathbf{E}^s$ with $\mathbf{M}_\Gamma \mathbf{E}^s$ being the scattered electric field measured on the set Γ, and

$$A_j\eta = A\left(\beta^T \mathbf{E}_{inc}\left(k^2\eta + \beta^T\nabla^2\eta\beta\right)\right) \quad \text{and} \quad d_j = \beta^T\mathbf{d}. \tag{13}$$

Hence, we first have to solve the system of scalar equations

$$A_j\eta = d_j \text{ on } \Gamma, \text{ for all } j = j(\alpha,\beta), (\alpha,\beta) \in S_p, \tag{14}$$

then compute the contrast function f from η by solving the well-posed equation (10).

The Kaczmarz' algorithm, also called ART-method, is widely used in computer tomography. It is an iterative method to solve over- or underdetermined linear systems of equations, see [8]. It may also be adapted to nonlinear problems, see [9]. In the framework of inverse scattering, Kaczmarz' algorithm was applied by Natterer and Wübbelling in [9] for acoustic waves and by Dorn *et al.* [4], also by Vögeler [12], for electromagnetic imaging in a context of partial differential equations. To solve (14), we apply Kaczmarz' method. For more details as well as numerical tests with simulated and real data we refer to [7].

References

[1] Abubakar A, Habashy M T, Van den Berg P M and Dries Gisolf (2005) The diagonalized contrast source approach: an inversion method beyond the Born approximation *Inverse Problems* **21** 685-702

[2] Dautray R and Lions J-L (1990) *Mathematical Analysis and Numerical Methods for Science and Technology* Vol 3 (Berlin: Springer-Verlag)

[3] Colton D and Kress R (1998) *Inverse Acoustic and Electromagnetic Scattering Theory* 2nd edn (Berlin: Springer)

[4] Dorn O, Bertete-Aguirre H, Berryman J G and Papanicolaou G C (1999) A nonlinear inversion method for 3D electromagnetic imaging using adjoint fields, *Inverse Problems* **15** 1523-1558

[5] Habashy T M, Groom R W and Spies B R (1993) Beyond the Born and Rytov approximation: A nonlinear approach to electromagnetic scattering, *J. Geophys. Res.* **98** 1759-76

[6] Lakhal A and Louis A K (2008) Locating radiating sources for Maxwell's equations using the approximate inverse *Inverse Problems* **24** 045020 (18pp)

[7] Lakhal A: A decoupling-based imaging method for inverse medium scattering for Maxwell's equations 2010 *Inverse Problems* **26** 015007

[8] Natterer F (1986) *The Mathematics of Computerized Tomography,* (Stuttgart: Teubner-Wiley)

[9] Natterer F and Wübbeling F (2001) *Mathematical Methods in Image Reconstruction* (Philadelphia: SIAM)

[10] Torres-Verdin C and Habashy T M (1994) Rapid 2.5-dimensional forward modeling and inversion via a new nonlinear scattering approximation *Radio Sci.* **29** 1051-79

[11] Torres-Verdin C and Habashy T M (1995) A two-step linear inversion of two dimensional electric conductivity *IEEE Trans. Antennas Propag.* **43** 405-15

[12] Vögeler M (2003) Reconstruction of the three-dimensional refractive index in electromagnetic scattering by using a propagation backpropagation method *Inverse Problems* **19** 739-753

Photoacoustic Imaging taking into account Attenuation

Otmar Scherzer

(joint work with Richard Kowar)

The difficult issue of effects of and corrections for the attenuation of acoustic waves in *photoacoustic imaging* has been studied [8, 1, 10, 6], although no complete conclusion on the feasibility of this models has been reached. Mathematical models of attenuation are formulated in the frequency domain, since the attenuation is known to be strongly frequency dependent. Let G_0, G be the Green functions of the wave equation and the attenuated wave equation, respectively. The common *attenuation model* reads as follows:

$$\mathcal{F}G(x,\omega) = \exp\left(-\beta(|x|,\omega)\right)\mathcal{F}G_0(x,\omega)\ . \tag{1}$$

Here $\mathcal{F}$ denotes the Fourier transform with respect to time, ω is the frequency, and x is the space coordinate. The complex function $\beta(|x|,\omega)$ is called the *attenuation coefficient*. Well known models, are *power laws*, Szabo's model [11, 12], and the thermoviscous wave equation (see e.g. [4]), which are characterized by different functions β.

Distinctive features of unattenuated wave propagation (i.e., the solution of the standard wave equation) are *causality* and *finite front wave speed*. It is reasonable to assume that the attenuated wave satisfies these distinctive properties as well.

The standard photoacoustic imaging problem consists in backpropagation of waves $p(s,t)$, where s is an element of the recording surface, to $f(x) = p(x,0)$, where $x \in \Omega$, and Ω is domain of interest, bounded by the measurement surface. Thereby p is considered the solution of the wave equation

$$\frac{\partial^2 p}{\partial t^2}(x,t) = \Delta p\,, \quad x \in \mathbb{R}^3,\ t > 0$$

with initial conditions

$$p(x,0) = f(x)\,, \quad \frac{\partial p}{\partial t}(x,0) = 0\,, \quad x \in \mathbb{R}^3\,.$$

The parameter f is the imaging parameter in photoacoustics. For a series of methods for backpropagation we refer to [7]. If attenuation is taken into account, and equation (1) is considered the basic model for attenuation, then the imaging problem decouples into the standard photoacoustic imaging problem for the wave equation and a deconvolution problem with kernel $\mathcal{F}^{-1}\left(\exp\left(-\beta(|x|,\cdot)\right)\right)(t)$.

[3] state "Power attenuation laws have been used in phenomenological acoustics because of their extreme simplicity as well as their conformity with the physical requirements of causality and dissipativity." However, as it is also been stated in [3], causality and dissipativity restricts the frequency dependence of attenuation in a power-law medium where $A = Const \times |\omega|^\alpha$ to $0 < \alpha < 1$. This can also be deduced in a mathematically rigorous way from a distribution theory [2]. In contrast to previous work the powerful mathematics of distribution theory allows to prove or disprove causality very efficiently.

Power laws with exponent greater than one are of relevance in photoacoustic imaging, since for biological specimens and oils, the power law index has been experimentally identified to be larger than one.

Inversion techniques based on an un-physical model are questionable. We therefore propose using an approximate power law [6]: The philosophy behind this approach is to calculate an attenuation law, which approximates a power law in the frequency spectrum where it has been experimentally validated and it is extended outside of the measured spectrum in such a way that the wave model becomes causal. Based on the results from [6], we developed such approximation models that satisfy the needs of causality and in addition have a finite front wave speeds.

A work, which is concerned with causal attenuated wave equations, which starts modeling at constitutive laws is [9]. There the derived equations are defined via *relaxation* and currently cannot simulate power laws with fractional index.

References

[1] P. Burgholzer, H. Grün, M. Haltmeier, R. Nuster, and G. Paltauf. Compensation of acoustic attenuation for high-resolution photoacoustic imaging with line detectors. volume 6437, page 643724. SPIE, 2007.

[2] R. Dautray and J.-L. Lions. *Mathematical analysis and numerical methods for science and technology. Vol. 2.* Springer-Verlag, Berlin, 1988. Functional and variational methods, With the collaboration of Michel Artola, Marc Authier, Philippe Bénilan, Michel Cessenat, Jean Michel Combes, Hélène Lanchon, Bertrand Mercier, Claude Wild and Claude Zuily, Translated from the French by Ian N. Sneddon.
[3] A. Hanyga and M. Seredyńska. Power-law attenuation in acoustic and isotropic anelastic media. *Geophys. J. Int.*, 155:830–838, 2003.
[4] L. E. Kinsler, A. R. Frey, A. B. Coppens, and J. V. Sanders. *Fundamentals of Acoustics.* Wiley, New York, 2000.
[5] R. Kowar and O. Scherzer. Photoacoustic imaging taking into account attenuation. Technical Report work in progress, 2010.
[6] R. Kowar, O. Scherzer, and X. Bonnefond. Frequency dependent attenuation revisited. Reports of FSP S105 - "Photoacoustic Imaging" 16, University of Innsbruck, Austria, 2009.
[7] P. Kuchment and L. A. Kunyansky. Mathematics of thermoacoustic and photoacoustic tomography. *European J. Appl. Math.*, 19:191–224, 2008.
[8] P. J. La Riviére, J. Zhang, and M. A. Anastasio. Image reconstruction in optoacoustic tomography for dispersive acoustic media. *Opt. Letters*, 31(6):781–783, 2006.
[9] A.I. Nachman, J.F. Smith, and R.C. Waag. An equation for acoustic propagation in inhomogeneous media with relaxation losses. *J. Acoust. Soc. Amer.*, 88(3):1584–1595, 1990.
[10] S.K. Patch and A. Greenleaf. Equations governing waves with attenuation according to power law. Technical report, Department of Physics, University of Wisconsin-Milwaukee, 2006.
[11] T.L. Szabo. Time domain wave equations for lossy media obeying a frequency power law. *J. Acoust. Soc. Amer.*, 96:491–500, 1994.
[12] T.L. Szabo. Causal theories and data for acoustic attenuation obeying a frequency power law. *J. Acoust. Soc. Amer.*, 97:14–24, 1995.

Regularization with sparsity constraints and impedance tomography

Peter Maass
(joint work with Bangti Jin, Taufiquar Khan, Michael Pidcock)

1. Introduction

Sparsity concepts have recently been investigated intensively in several disciplines, including signal processing and statistics. Theoretically, such concepts allow to (exactly) recover signals from far less data than conventional data acquisition rate dictated by Shannon's law [7] if the sparsity assumption is fulfilled. Practically, sparsity arises in many physical signals, hence the approach is of significant importance, and has found applications in biomedical imaging, astronomy, geophysics, bioinformatics, and many others.

The present work outlines our ongoing research on sparsity constraint regularization in electrical impedance tomography (EIT), for details see [11, 10]. In general, the idea of sparsity constraints has been extensively investigated in inverse problems. For instance, the well-posedness and regularizing properties of Tikhonov regularization formulation has been established, and efficient algorithms for solving the optimization problems are developed for both linear and nonlinear inverse problems [6, 2, 5]. However, the application of sparsity regularization to parameter identification problems like EIT remains challenging, and its success requires additional efforts.

We aim at deriving efficient sparse reconstruction algorithms for EIT. We start with the mathematical model. Let Ω be an open bounded domain with boundary Γ. Then the EIT forward problem is given by (c.f. [3])

$$-\nabla \cdot (\sigma \nabla u) = 0 \quad \text{in } \Omega,$$

with a Neumann boundary condition $\sigma \frac{\partial u}{\partial n} = j$, with j being the input current. The resulting potential ϕ is measured on the boundary. We shall denote the forward operators of the Neumann and Dirichlet problems by F_N^σ and F_D^σ, respectively. In practice, several input currents are employed, and the resulting (noisy) potentials are measured. The inverse problem is to estimate the unknown physical conductivity $\sigma^\dagger$ from these noisy potential data.

We shall adopt a Tikhonov type method, i.e. we attempt to minimize

$$J_\alpha(\sigma) = \underbrace{\int_\Omega \sigma |\nabla (F_N^\sigma j - F_D^\sigma \phi)|^2 dx}_{D(\sigma)} + \alpha \sum_k |\langle \delta\sigma, \psi_k \rangle|,$$

where $\delta\sigma = \sigma - \sigma_0$ stands for the inhomogeneity, with σ_0 being the background, and $\{\psi_k\}$ is an orthonormal basis. The scalar parameter α determines the tradeoff between the two terms: the discrepancy term $D(\sigma)$ incorporates the data, whereas the regularization term enforces the a priori knowledge, i.e. away from the background, the conductivity can be sparsely represented in the basis $\{\psi_k\}$. We assume that $\mathrm{supp}(\sigma - \sigma_0) \subset \Omega' \subset\subset \Omega$, and $\lambda \le \sigma \le \lambda^{-1}$ for a fixed $\lambda > 0$.

Next we sketch the proposed sparsity reconstruction algorithm for EIT.

2. Sparse reconstruction algorithm

A standard approach for minimizing ℓ_1 type regularization is iterative soft shrinkage, which was introduced in the pioneering work [6] for minimizing functionals such as

$$\tfrac{1}{2}\|K(x) - y^\delta\|^2 + \alpha \|x\|_{\ell_1},$$

where $K : X \mapsto Y$ is a bounded but nonlinear operator. The algorithm takes the following form: give an initial guess x^0, and the iteration proceeds

$$x^{k+1} = S_\alpha(x^k - \tau K'(x^k)^*(K(x^k) - y^\delta)),$$

where τ is the step size, and S_α is the soft shrinkage operator defined componentwise as below

$$(S_\alpha(x))_i = \begin{cases} (|x_i| - \alpha)\mathrm{sign}(x_i), & \text{if } |x_i| > \alpha, \\ 0, & \text{otherwise.} \end{cases}$$

So basically, the algorithm consists of two steps: one first performs a gradient descent step with step size τ, and then a shrinkage step. The second step promotes the sparsity of the reconstruction. Theoretically, it is known that under appropriate conditions on the operator K and the step size τ, the algorithm will converge to a minimizer of the Tikhonov functional.

Obviously, the application of the algorithm to EIT, i.e. the function J_α, requires suitable differentiability of the discrepancy functional. This is ensured by the following result [10].

Theorem 1. *The discrepancy functional $D(\sigma)$ is Frechét differentiable with respect to $L_p(\Omega')$ for $p > 2Q/(Q-2)$, and the Frechét derivative is given by*

$$D'(\sigma)[\delta\sigma] = \int_\Omega \delta\sigma(|\nabla F_D^\sigma \phi|^2 - |\nabla F_N^\sigma j|^2)dx,$$

where the constant Q depends on Ω, Ω' and λ.

In addition to the above analytic result, we need to choose the gradient and the step size τ carefully. Up to now, the conductivity is a priori only bounded in L_∞ norm, which automatically induces a L_∞ weak $*$ compactness. However, the discrepancy functional $D(\sigma)$ is not L_∞ weak $*$ lower semicontinuous [13]. Numerically, this causes oscillations in reconstructions. In order to remedy the issue, we propose to smooth the gradient as follows

$$-\Delta D_s'(\sigma) + D_s'(\sigma) = D'(\sigma) \quad \text{in } \Omega',$$

together with a homogeneous Dirichlet boundary condition. Upon utilizing the smoothed gradient $D_s'(\sigma)$, we implicitly restrict the admissible solution to a smooth subset, thereby circumventing the problem of insufficient regularity, and also ensure the desired boundary condition [10].

The iterative soft shrinkage with fixed step size resembles the classical steepest descent algorithm, and thus it also suffers from slow convergence. One way to enhance the convergence speed is to adaptively select the step size. Among various existing rules, the one due to Barzilai and Borwein [1] seems particularly attractive due to its easy implementation and theoretical underpinning. We shall employ the rule to select the step size τ_i for each iteration.

Now we can give the complete algorithm, which computes an estimate by iterated soft shrinkage iterations, see [10]. One can also incorporate an outer loop for choosing optimal input currents see [11, 10].

Algorithm 1 Sparse reconstruction algorithm

1: Set $\delta\sigma^0 = 0$
2: **for** $j = 1, \ldots, J$ **do**
3: Compute $\sigma^j = \sigma_0 + \delta\sigma^j$;
4: Compute the gradient $D'(\sigma^j)$;
5: Compute the smoothed gradient $D_s'(\sigma^j)$;
6: Determine the step size τ_j;
7: Update inhomogeneity by $\delta\sigma^{j+1} = \delta\sigma^j - \tau_j D_s'(\sigma^j)$;
8: Threshold $\delta\sigma^{j+1}$ by $S_{\tau_j\alpha}(\delta\sigma^{j+1})$;
9: Check stopping criterion.
10: **end for**
11: **output** approximate minimizer $\delta\sigma$.

3. Numerical results and discussion

Here we present some reconstructions for simulated noisy data. The experimental setup is the same as [10]. In particular, we employ five input currents, which correspond to Isaacson's iteration [9, 11]. Fig. 1 shows the numerical results for homogeneous and discontinuous background. It is observed the inclusions are well separated, and their magnitudes are in excellent agreement with the exact one. Fig. 2 compares the reconstructions with the standard dipole input (opposite) and Isaacson's iteration [11]. The result by the former is far less accurate in terms of magnitude and separation. However, this can be further improved by using newly computed optimal currents, see the right panel. Current investigation concerns the evaluating the method against real data as in [4, 12].

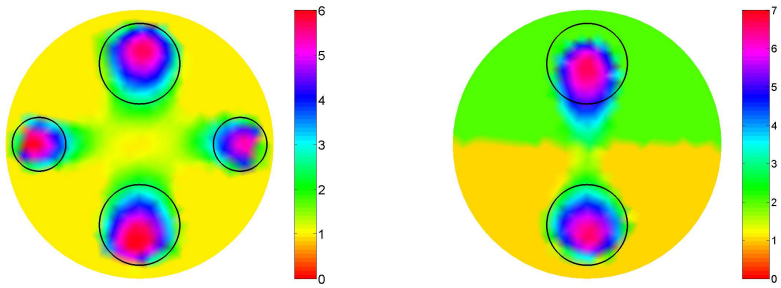

Figure 1. Numerical reconstructions. Left: homogeneous background and Right: discontinuous background.

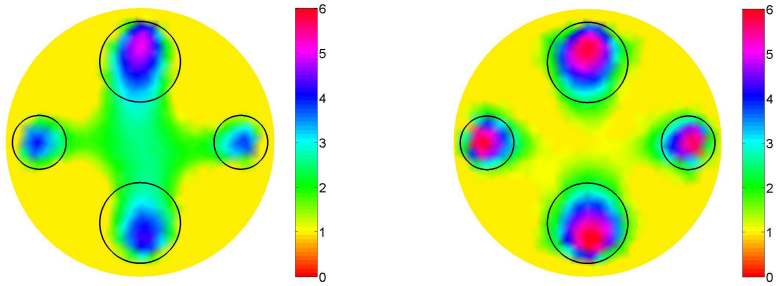

Figure 2. Numerical reconstructions. Left: dipole type input currents, and Right: further enhanced with input currents by Isaacson's iteration.

References

[1] J. Barzilai, J.M. Borwein. *Two-point step size gradient methods*, IMA J. Numer. Anal. **8**(1998) 141–148.

[2] T. Bonesky, K. Bredies, D.A. Lorenz, P. Maass. *A generalized conditional gradient method for nonlinear operator equations with sparsity constraints*, Inverse Problems **23**(2007), 2041–2058.

[3] L. Borcea, *Electrical impedance tomography*, Inverse Problems **18**(2002) R99–R136.

[4] A. Borsic, B.M. Graham, A. Adler, W.R.B. Lionheart, *In vivo impedance imaging with total variation regularization*, IEEE Trans. Med. Imag. **29**(2010), 44–54.

[5] K. Bredies, D.A. Lorenz, P. Maass, *A generalized conditional gradient method and its connection to an iterative shrinkage method* Comput. Optim. Appl. **42**(2009), 173–193.

[6] I. Daubechies, M. Defrise, C. De Mol, *An iterative thresholding algorithm for linear inverse problems with a sparsity constraint*, Comm. Pure Appl. Math. **57**(2004) 1413–1457.

[7] D. Donoho, Compressed Sensing, IEEE Trans. Inform. Theory 52(2006) 1289–1306.

[8] M. Hanke, M. Brühl, Martin, *Recent progress in electrical impedance tomography*, Inverse Problems **19**(2003), S65–S90.

[9] D. Isaacson, *Distinguishability of conductivities by electric current computed tomography*, IEEE Trans. Medical Imaging **5**(1986), 91–95.

[10] B. Jin, T. Khan, P. Maass, *Sparse reconstruction in electrical impedance tomography*, submitted.

[11] B. Jin, T. Khan, P. Maass, M. Pidcock, *Function spaces and optimal currents in impedance tomography*, DFG-Schwerpunktprogramm 1324, Preprint 17, 2009.

[12] K. Karhunen, A. Seppänen, A. Lehikoinen, P.J.M. Monteiro, J.P. Kaipio, *Electrical resistance tomography imaging of concrete*, Cement and Concrete Research **40**(2010), 137–145.

[13] R.V. Kohn, M. Vogelius, *Relaxation of a variational method for impedance computed tomography*, Comm. Pure Appl. Math. **40**(1987) 745–777.

Backscatter data in impedance tomography

Martin Hanke

(joint work with Nuutti Hyvönen, Stefanie Reusswig)

We consider the following experimental setup: A pair of electrodes is attached next to a point on the boundary of a two-dimensional (bounded) object D, and measures the voltage that is required to drive a fixed current through these electrodes; then this same experiment is repeated for every point along the boundary. We want to investigate whether these "backscatter" data suffice to reconstruct one, or several, inclusion(s) within a homogeneous background with constant positive conductivity.

To analyze this problem it is useful to turn to so-called relative data, i.e., to subtract these data from the corresponding measurements for a completely homogeneous object. Using a realistic model for real-life electrical measurements it has been shown in [3] that the corresponding relative data taken near $x_\tau \in \partial D$ are first-order approximations of the quantity

$$b(x_\tau) \;=\; -\frac{\partial}{\partial \tau} w(x_\tau)\,, \tag{1}$$

where $w = u - u_0$ is the relative potential given by the solution u of

$$\nabla \cdot (\sigma \nabla u) \;=\; 0 \quad \text{in } D\,, \qquad \frac{\partial}{\partial \nu} u \;=\; -\delta'_{x_\tau} \quad \text{on } \partial D\,,$$

and u_0 of

$$\Delta u_0 = 0 \quad \text{in } D\,, \qquad \frac{\partial}{\partial \nu} u_0 = -\delta'_{x_\tau} \quad \text{on } \partial D\,,$$

respectively. Here, τ is the arc length parameter of the boundary, ν the outer normal of D, and δ'_{x_τ} the tangential derivative of a delta distribution located in x_τ; physically, this corresponds to a tangential dipole current source at this boundary point. Finally, we assume that σ equals one in $D \setminus \overline{\Omega}$, where $\Omega = \Omega_1 \cup \cdots \cup \Omega_m$, and that Ω_j, $j = 1, \ldots, m$, are simply connected domains (the *inclusions*) which satisfy $\overline{\Omega}_j \subset D$ and $\overline{\Omega}_j \cap \overline{\Omega}_k = \emptyset$ for $j \neq k$. As stated above, we assume that within each Ω_j the conductivity $\sigma = \sigma_j \in \mathbb{R}_0^+ \setminus \{1\}$ is constant.[1]

Our interest is in the following *inverse problem*:

> *Given the full backscatter data $b : \partial D \to \mathbb{R}$ of (1), is it possible to identify and, possibly, reconstruct the inclusion(s) Ω_j, $j = 1, \ldots, m$?*

For a single inclusion this question appears to be fair – a one-dimensional function is given as data, and one aims to reconstruct a single curve in the two-dimensional plane – although it may be necessary to provide full information about the conductivity within the inclusion. In fact, in [5] we could establish the following result.

Theorem 1. *Assume that Ω and $\tilde{\Omega}$ are two simply connected insulating inclusions with C^2 boundaries within the unit disk D, that produce the same backscatter data. Then $\Omega = \tilde{\Omega}$.*

The proof of this theorem makes heavy use of conformal mapping theory. More precisely, the proof employs a conformal map of $D \setminus \overline{\Omega}$ onto a conformally equivalent annulus, and studies the effect of this transformation on the backscatter data. For the annulus, it is easy to see that the backscatter data are constant. Using this transformation one can derive a nonlinear third-order differential equation for the boundary map associated with this conformal transformation, which invokes the given backscatter data and the (unknown) constant backscatter for the corresponding annulus. Due to the necessary periodicity requirements of this boundary map it is possible to prove that the differential equation has a unique solution, and one can also use this as a constructive means to determine the inclusion numerically. As the latter requires analytic continuation, however, this procedure is very susceptible to numerical errors, and this has to be treated properly in a numerical implementation. (This aspect will be part of the forthcoming dissertation of Stefanie Reusswig.)

The particular example of the annulus also shows that a single inclusion can only be determined uniquely from backscatter data, if the conductivity within the inclusion is known. In fact, if D is the unit disk, and Ω is a circular inclusion of

[1] Formally, the case $\sigma_j = 0$, i.e., an insulating inclusion, has to be treated in a slightly different way; however, all results that we refer to extend to this degenerate situation.

radius R with conductivity σ, then the corresponding backscatter is given by

$$\beta_{\sigma,R} = \frac{2}{\pi} \sum_{k=1}^{\infty} k \, \frac{qR^{2k}}{1 - qR^{2k}}, \qquad q = \frac{1-\sigma}{1+\sigma},$$

from which one can determine R, provided that σ is known, but cannot determine σ *and* R. As of today it is not known whether a single inclusion of *known* conductivity $\sigma \neq 0$ is uniquely determined by the backscatter data.

Unfortunately, the techniques from [5] give little to no hint on how to approach the inverse problem, if the inclusion fails to be insulating, or if there is more than one inclusion. However, a side result in [5] shows that if the plane is identified with $\mathbb{C}$, and if Ω is an insulating inclusion (with C^2 boundary) then the backscatter data extend to an analytic function in $D \setminus \overline{\Omega}$. It turns out that this result *can* be extended to several inclusions with varying conductivities, cf. [6]:

Theorem 2. *Let D be the unit disk, and assume that Ω consists of m simply connected components with C^2 boundaries fulfilling the assumptions listed above. Then the backscatter data extend as an analytic function to $D \setminus \overline{\Omega}$ (considered as a subset of the complex plane).*

As the backscatter data are real, this result can be recast in terms of harmonic functions: There is a function $u : D \to \mathbb{R}$, i.e., the real part of the analytic extension of our backscatter data, that satisfies the Laplace equation

$$\Delta u = F \qquad \text{in } D$$

with Cauchy boundary data

$$u = b \quad \text{and} \quad \frac{\partial}{\partial \nu} u = 0 \quad \text{on } \partial D,$$

and the source term F has compact support within $\overline{\Omega}$. Therefore we can attempt to solve our inverse problem by determining suitable sources that are compatible with the given Cauchy data.

One such technique has been developed in [4], by carrying over the concept of convex scattering supports of Kusiak and Sylvester [7] from Helmholtz' to Laplace's equation. It is thus possible to construct numerically a convex set from the given backscatter data, that provably is contained within the convex hull of the given inclusions – assuming exact data *and* arithmetic, of course. Various regularization strategies are possible to deal with noisy data.

In contrast to the method for a single insulating inclusion indicated above, however, this result does not give the full inclusion, but only some approximation of its convex hull. In effect, this may not serve for more than to simply *locate* the inclusion. Moreover, as the reconstruction is connected to the convex hull of the inclusion(s), this method is not suitable to locate *several* inclusions.

On the other hand, several inclusions can be treated by approximating the backscatter data by rational functions (of a complex variable), e.g., by utilizing the concept of Fourier-Padé approximations, cf. Gragg and Johnson [1]. The poles of these rational approximations tend to indicate the locations of the inclusions.

The smaller the inclusions, the better will be these approximations. This will be explored in some forthcoming work [2].

The author appreciates financial support by the Deutsche Forschungsgemeinschaft (DFG) under grant HA 2121/6.

References

[1] W.B. Gragg and G.D. Johnson, *The Laurent-Padé table*, in Information Processing 74, Proceedings IFIP Congress 1974, North-Holland, Amsterdam, 1974, pp. 632–637.

[2] M. Hanke, *Locating several small inclusions in impedance tomography from backscatter data*, in preparation.

[3] M. Hanke, B. Harrach, and N. Hyvönen, *Justification of point electrode models in electrical impedance tomography*, submitted.

[4] M. Hanke, N. Hyvönen, and S. Reusswig, *Convex source support and its application to electric impedance tomography*, SIAM J. Imaging Sci. **1** (2008), 364–378.

[5] M. Hanke, N. Hyvönen, and S. Reusswig, *An inverse backscatter problem for electric impedance tomography*, SIAM J. Math. Anal. **41** (2009), 1948–1966.

[6] M. Hanke, N. Hyvönen, and S. Reusswig, *Convex backscattering support in electric impedance tomography*, Numer. Math., to appear.

[7] S. Kusiak and J. Sylvester, *The scattering support*, Comm. Pure Appl. Math. **56** (2003), 1525–1548.

Wave equation reflection tomography

Maarten de Hoop

Much research in modern, quantitative seismologyis motivated - on the one hand - by the need to understand subsurface structures and processes on a wide range of length scales, and - on the other hand - by the availability of ever growing volumes of high fidelity digital data from modern seismographs networks.

We discuss a description of elastic-wave (inverse) scattering modelling seismic reflection data in terms of Fourier integral operators. Through an extension, we ensure that the (single) scattering operator is microlocally invertible. We represent this extension in terms of a commutative diagram of operators. We formulate wave equation reflection tomography in terms of a range criterion, the range being described by (pseudodifferential) annihilators. We discuss a uniqueness result and present a construction of such annihilators. The presence of scatterers is required, but they remain unknown in the process. Finally, we relate the single scattering operators for different models to one another via a pseudodifferential evolution equation, viz. by using the corresponding propagator. This propagator opens the way for developing nonliner updating strategies.

Inversion algorithms for the spherical Radon and cosine transforms

Martin Riplinger, Malte Spiess
(joint work with Alfred K. Louis, Evgeny Spodarev)

Stationary Poisson processes of cylinders are defined as "locally finite" random sets of cylinders, where a cylinder is the Minkowski sum of a line (called the *direction space*) and a *base*, i.e. a convex set in the space orthogonal to the direction space. In our talk we consider stationary Poisson cylinder processes Φ_d in the most interesting dimensions $d = 2, 3$. Such a process has two essential properties:

- Intensity λ: expected total length of the central lines of cylinders per unit volume,
- Directional distribution α: symmetric probability measure on $\mathcal{S}^{d-1}$, the probability that a typical cylinder has a certain direction space.

For the estimation of the intensity there exist well-working methods (see [9]), whereas the appropriate estimation of the directional distribution is still an open problem. In our talk we present a new numerically stable method to estimate the directional distribution.

We assume that we can estimate the *rose of intersections* $g(\eta)$, which is the intensity of $\Phi^d \cap \eta^\perp$, $\eta \in \mathcal{S}^{d-1}$. For even functions f we define the cosine transform as

$$Cf(\eta) = \int_{\mathcal{S}^{d-1}} |\langle \eta, \xi \rangle| \, f(\xi) \, d\xi, \qquad \eta \in \mathcal{S}^{d-1},$$

where $d\xi$ is the spherical surface area measure. If α is absolutely continuous w.r.t. the spherical surface area measure, i.e. it has a density φ, it can be shown that

$$g(\eta) = \frac{\lambda}{\omega_{d-1}} \, \mathcal{C}\varphi(\eta), \qquad \eta \in \mathcal{S}^{d-1}, \tag{1}$$

where ω_{d-1} denotes the surface area of the $(d-1)$-dimensional unit sphere. This means that the cosine transform maps the density of directional distribution to the intensity of the intersection process of the cylinders with test hyperplanes. Therefore, to estimate the directional distribution, a numerical inversion of the cosine transform from finitely many samples has to be performed. This approach has been investigated e.g. by Kiderlen [2]. But his proposed algorithms only lead to discrete reconstructions, which are concentrated on a finite number of points and hence sometimes look artificial. Continuous reconstructions of the directional distribution, which provide the chance of better model fits, are missing so far in the literature.

The equation (1) has a unique solution for arbitrary dimension d (see [4]). Furthermore there already exist some theoretical inversion formulae:

- $d = 2$: Hilliard [1] (1962), Mecke [5] (1981).
- $d = 3$: Mecke and Nagel [6] (1980).
- $d \geq 3$: Spodarev [10] (2001). (Formulae for absolutely continuous α)
- $d \geq 3$: Rubin [8] (2002). (convolution - backprojection method)

While these formulae form a basis for theoretical considerations, they have to be stabilized for practical use, because of their numerical instability.

To develop numerical inversion algorithms for the cosine transform in the two- and three-dimensional case, we apply the method of the approximate inverse [3]. The idea is to solve the auxiliary problem

$$C\psi_\gamma(x,\,\cdot\,) = e_\gamma(x,\,\cdot\,) \tag{2}$$

for a chosen mollifier e_γ. The cosine transform is self-adjoint with respect to the inner product in L^2. Since the solution of the problem (2) does not depend on the given data g, it can be solved in advance. After this we calculate a smoothed version f_γ of the solution, i.e.

$$f_\gamma(x) := \langle f, e_\gamma(x,\cdot)\rangle_{L^2(\mathcal{S}^d)} = \langle g, \psi_\gamma(x,\cdot)\rangle_{L^2(\mathcal{S}^d)} =: T_\gamma g(x).$$

This leads to very fast algorithms, because we only have to calculate the inner product of our data g with the precalculated reconstruction kernel.

In the two-dimensional case, directional distribution densities correspond to π-periodic functions. One usually considers the sine transform

$$S\varphi(x) = \int_0^\pi |\sin(x-y)|\,\varphi(y)\,dy/\pi, \quad x \in [0,\pi),$$

which is in 2D only a translation of the cosine transform, i.e. $C\varphi(x) = S\varphi(x+\frac{\pi}{2})$. Using a result of [5], the reconstruction kernel can be determined by the equation

$$\psi_\gamma(x,y) = \tfrac{1}{2}e_\gamma(x,y) + \tfrac{1}{2}\tfrac{\partial^2}{\partial y^2}e_\gamma(x,y).$$

In the three-dimensional case we also consider another transform, which is closely related to the cosine transform, namely the spherical Radon transform (also known as Funk transform)

$$Rf(\eta) = \frac{1}{2\pi}\int_{\mathcal{S}^2\cap\eta^\perp} f(\xi)\,d\xi.$$

In order to apply the approximate inverse for both transforms, we have to determine the reconstruction kernel for a given mollifier. Our idea is to consider a mollifier depending only on the geodesic distance between x and y and not on the points themselves. Since both transforms are rotation invariant, it suffices to calculate the reconstruction kernel for one fixed reconstruction point. For this issue we choose the north pole. As an example, we consider the following even mollifier

$$e_\gamma(\varphi,\theta) = \frac{1}{c(\gamma)}\exp\left(-\frac{\sin^2\theta}{\gamma^2}\right), \quad \varphi\in[0,2\pi), \quad \theta\in[0,\pi],$$

which depends only on the polar angle θ. The normalisation factor $c(\gamma)$ is calculated to guarantee

$$\int_{\mathcal{S}^2} e_\gamma(x,y)dy = 1, \quad \gamma > 0.$$

For the spherical Radon transform the corresponding reconstruction kernel is given by

$$\psi_\gamma(\theta) = \frac{1}{c(\gamma)}\left(1 - \frac{\sqrt{\pi}\cos\theta}{\gamma}\exp\left(\frac{-\cos^2\theta}{\gamma^2}\right)\operatorname{erfi}\left(\frac{\cos\theta}{\gamma}\right)\right)$$

and for the cosine transform by

$$\overline{\psi}_\gamma(\theta) = \frac{1}{2\pi\gamma^5 c(\gamma)}\left(\sqrt{\pi}\exp\left(\frac{-\cos^2\theta}{\gamma^2}\right)\operatorname{erfi}\left(\frac{\cos\theta}{\gamma}\right)\cos\theta\cdot T_1 + T_2\right) + (2\pi)^{-1}$$

with

$$T_1 = 3\gamma^2 - 5\gamma^2\cos^2\theta - 2\cos^2\theta + 2\cos^4\theta,$$
$$T_2 = 2\gamma(\cos^2\theta)(1 - \cos^2\theta + 2\gamma^2) - \gamma^2.$$

More details will be available in our forthcoming paper [7].

Finally, we present one numerical example from simulated data. We simulated a Poisson cylinder process in the unit cube with intensity 500 and cylinder radius 0.005, made a voxelized image with resolution 500^3 and estimated the rose of intersections from this image in 400 directions.

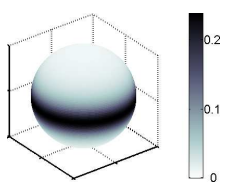

Original density

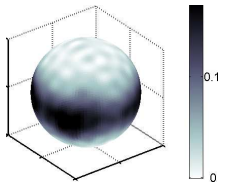

Reconstruction based on 1 realization

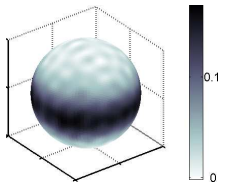

Reconstruction based on an average over 5 realizations

References

[1] J.E. Hilliard, *Specification and measurement of microstructural anisotropy*, Trans. of the Metallurgical Soc. of Aime **224** (1962) 1201–1211

[2] M. Kiderlen, *Estimation of the mean normal measure from flat sections*, Adv. in Appl. Probab. **40** (2008), 31–48.

[3] A.K. Louis, *Approximate inverse for linear and some nonlinear problems*, Inverse Problems **12** (1996), 175–190.

[4] G. Matheron, *Random sets and integral geometry*, *Wiley, New York* (1975)

[5] J. Mecke *Formulas for stationary planar fibre processes III – Intersections with fibre systems*, Math. Operationsforsch. Statist. Ser. Statistik **12** (1981), 201–210

[6] J. Mecke, W. Nagel *Stationäre räumliche Faserprozesse und ihre Schnittzahlrosen*, Elektron. Informationsverarb. Kybernet. **16** (1980),475–483

[7] A.K. Louis, M. Riplinger, M. Spiess, E. Spodarev, *Inversion algorithms for the spherical Radon and cosine transforms*, in preparation

[8] B. Rubin, *Inversion formulas for the spherical Radon transform and the generalized cosine transform*, Adv. in Appl. Math. **29** (2002), 471–497

[9] K. Schladitz, *Estimation of the intensity of stationary flat processes*, Adv. in Appl. Probab. **32** (2000), 114–139

[10] E. Spodarev *On the rose of intersections of stationary flat processes*, Adv. in Appl. Probab. **33** (2001), 584–599

On the Meaning of Mathematical Words in Natural Problems

Pierre C. Sabatier

Giving spaces C, E, and a mapping M is called giving a mathematical model[(1)] for a problem of measurements, C being the set of parameters that may characterize a system to be evaluated, and E being defined so as to contain all possible measurement results. It is also called defining a mathematical direct problem. A method constructing for any element e of E an element c of C such that $e = M(c)$, or, respectively, $e : close - to : M(c)$, is called a solution, or, respectively, a generalised solution of the mathematical inverse problem. Exact mathematical inverse problems are those where an exact function f in a class C_0 should be exactly determined from an exact function g in a class E_0. In "natural inverse problems", i.e. those which appear in natural phenomena, one should always remind that *data are uncertain, uncomplete, contradictory, the model (hence, M), is uncertain*, and a "solution" should reproduce the data through the model within these two ranges of uncertainties, *but cannot be accepted if it has too large variations for small ones of data* ("regularised solutions"): we shall call these requirements the "global uncertainties requirement". Clearly, the definition of solution existence is quite simple both in exact inverse problems and in natural ones. Of course, the definition of exact solution uniqueness is also quite trivial. As for regularised solutions, when they exist, they are never unique, but in some cases, those which are not discarded by physical conditions remain close to each other, in the sense of the topology chosen in C. In these cases, one can talk of a "weak nonuniqueness", and this concept replaces for "natural problems" that of "uniqueness". But it is a difficult concept! I gave already exact examples where nonuniqueness was the rule if C contains all the allowed physical parameters but uniqueness had been restored by shrinking C into C_0 by strong "a priori" informations: I showed that taking into account the model uncertainties (unavoidable in any "natural inverse problem") may then produce acceptable solutions that are quite far from the original one, i.e. a "strong" nonuniqueness. Hence I called the way of "restoring uniqueness" an"artificial restoring of uniqueness", and I advocated against it. Here, I recall and comment two examples, and give a remark on "natural" boundary values.
The simplest (and well known) example is that where the"result" F to be measured is the Fourier transform of the unknown "parameter" f. If F is given in $L^2(\mathbb{R})$, and f is sought in $L^2(\mathbb{R})$, the I.P. is well-posed, Parseval theorem guarantees a strong stability, and the inversion formula is given by the conjugate Fourier transform. But suppose the measurements were done behind a linear filter such that we see $F(\lambda)$ only on $[-b, b]$. The reciprocal images of elements F whose support is outside of it are **invisible** parameters. The nonuniqueness is **removed** if the a priori information on f is such that the values of its image $F(\lambda)$ inside $[-b, b]$ determine those outside - which is the case if f is imposed for instance such an a priori assumption that its image is analytic (e.g. finitely supported or exponentially bounded functions f). But stability problems in the continuation need regularisations and, even so, data errors or noise result in a strong limitation of the

resolving power. Hence we see in this linear problem how instability is related to a neighboring nonuniqueness, and remains if uniqueness is "artificially" restored. A still more resistant nonuniqueness is seen if nonlinearity is introduced, e. g. in the Schrődinger Equation on the line[(2)], with a real potential V:

$$\left[-\frac{d^2}{dx^2} + V(x)\right] g(k,x) = k^2 g(k,x) \tag{1}$$

where k is the wave number. Assuming V in $L_1^1(\mathbb{R})$, we define the "outgoing" and "ingoing" Jost solutions of (1), which go respectively to $exp\,[\pm ikx]$ as $x \to \pm\infty$. For $k \neq 0$, $f^+(k,x)$ and $f^+(-k,x)$ are linearly independent, so that

$$T(k)f^-(k,x) \quad = \quad f^+(-k,x) + R(k)f^+(k,x) \tag{2}$$

$R(k)$, (called the reflection coefficient), is the "measurable" data, $T(k)$ the transmission coefficient, and for real V, the sum of their squared moduli is unity. Equation (1) is also that of the spectrum of $-\frac{d^2}{dx^2} + V$, i.e. the union of $\mathbb{R}$, (continuous spectrum), and, (not for all V), a discrete spectrum $k = i\kappa_1 ... i\kappa_n, ...$, for which(1) has solutions ψ_n in $L^2(\mathbb{R})$. For V "small enough", one can derive the so called (Born) approximation of the mapping $V \to R$ which gives R as a Fourier transform of V: it suggests that knowing R is necessary to construct V, which is true, but also that it is sufficient, which is not, and it also suggests that results of a uniqueness restoration would be similar to those above, which is also wrong. As a matter of fact, it is known for a long time that for reconstructing V, the knowledge of R must be completed by that of parameters associated to the discrete spectrum. Now, recall the example of a one "eigenvalue transparent potential":

$$V_0(x) = -\frac{2\kappa^2}{ch^2\left[\kappa\left(x - x_0\right)\right]} \tag{3}$$

For such a potential, R vanishes, and we can derive exactly the Jost solution f^+. Now, suppose V is truncated ouside of the finite interval $[-a, a]$. We can calculate the new Jost solutions (inside the interval) by projecting on $f^+(k,)$, and $f^+(-k,)$ the free wave functions $exp(ikx)$ and $exp(-ikx)$, and get the new values of $R(k)$ and $T(k)$. For the sake of simplicity, we write $R(k)$ only, and in the simpler case where x_0 vanishes.

$$R(k) = 2iexp(4i\gamma)[\left[\frac{p^2\kappa^2 sin(2(ka+\gamma)}{(p^4 - \kappa^4 exp(4i(ka+\gamma)}\right] \tag{4}$$

where $p^4 = \kappa^4 + 4k^2(k^2+\kappa^2)cosh^4(\kappa a)$, and $cos(2\gamma) = p^{-2}(\kappa^2 + 2k^2 cosh^2(\kappa a)$. It is easy to see that the integral of $|R(k)|^2$is smaller than $4\kappa cosh^{-2}\kappa a$. It follows that if this is a natural inverse problem, a convenient choice of large values for κ

and a can make arbitrarily small, both the error on the model and that on data, which are necessarily known only on a finite interval for k. Hence they would be consistent, up to these uncertainties, with both a zero potential and one given by truncating that of (4), and this one could be made, for small x, arbitrarily large! Now, if we go to solutions of KdV equation which are isospectral evolutions associated with (1), we see that the impossibility of telling (4) from a vanishing potential with a knowledge of R only with errors and on a limited range of k, is related with the well known fact that if we observe, from the coast, a few kilometers of the obviously quiet sea surface during a couple of hours, we may be very suddenly surprised by the surge of a long wave rounding up to the beach (tsunami!).

Remark In boundary values problems, we should determine a function Φ that satisfies a given partial differential equation inside a domain Ω from combinations of its values and the values of its normal derivative on $\partial\Omega$. If it is a natural problem, the boundary contour $\partial\Omega$ is in most case complicated and mathematicians use to model it by smooth or straight lines. Suppose now we have a linear problem, and the "boundary condition" is for instance $\Phi(x) = f(x)$ along $\partial\Omega$. If we knew the solution $S(y, x)$ for the boundary condition $\Phi(x) = \delta(x - y)$, with y in this "delta-function" being any point of the boundary, we get the solution $\Phi(x)$ corresponding to f by integrating $S(y, x)$ along $\partial\Omega$. Now, a very simple remark is directly inspired by old analyses of linear inverse problems: since this is a "natural problem", smoothing the boundary condition may be more justified than smoothing the line where this boundary condition is fixed. Hence why not replacing the "delta-function" by a smoothed one, provided that it has a "good" $\delta - ness$? In a problem of slide-tsunamis, we did it[3] with smoothed "delta-functions", for which the response can be calculated exactly, and its physical meaning is obvious. More generally, I emphasize the importance of suggesting new modellings [4] or solving (inverse) problems approximately, to show "natural features.

References

[1] P.C. Sabatier, Inverse Problems **25** pp.123001–123020 (2009).
[2] K. Chadan and P.C. Sabatier, "Inverse Problems of Quantum Scattering Theory". 2nd ed. Springer(1989)
[3] P.C. Sabatier, Journal of Fluid Mechanics, Vol. **126**, 27–58 (1983)
[4] P.C. Sabatier, "Well-posed Questions.....". in "Inverse Problems of Acoustic and Elastic Waves" F. Santosa et al. Ed. (SIAM, Philadelphia, 1984).

Wavelet-based Bayesian inversion for tomographic problems with sparse data

Samuli Siltanen

We study a new kind of tomographic X-ray imaging, where the patient is radiated as little as possible while recovering enough three-dimensional information for the clinical task at hand. The input can be only five to ten projection images

collected from different directions. Such sparse data often represent limited angle and local tomography configurations and lead to severely ill-posed reconstruction problems. This differs from traditional CT imaging, where a comprehensive data set is collected using a dedicated scanner, and the mildly ill-posed reconstruction problem is solved using the filtered back-projection (FBP) algorithm [8]. We concentrate on situations where a traditional CT scan is impractical due to radiation dose issues or lack of equipment; examples include dental imaging and screening mammography.

The incompleteness of our data violates the assumptions of FBP-type algorithms, and they do not provide acceptable reconstruction quality. During 2000–2009 our Finnish research team developed several new reconstruction algorithms capable of useful 3D X-ray imaging; the results are reviewed here. Some of the methods have already entered commercial products: see for example the dental implant planning device discussed in [1, 5] and demonstrated at http://www.vt-cube.com.

Sparse data dental 3D imaging using Bayesian inversion and total variation prior is studied in [13, 4] using the linear measurement model $m = Ax + \epsilon$ with additive Gaussian errors. The variables m, x and ϵ are vector valued random variables and A is the deterministic system matrix. The Bayesian answer to the inverse problem *given m, estimate x* is the posterior distribution $p(x|m) = Cp_{\rm pr}(x)p_{\rm noise}(m - Ax)$, where C is a normalization constant. Here the prior distribution $p_{\rm pr}(x)$ models all *a priori* information available about the unknown independently of the X-ray measurements. In practice one computes a representative point estimate from the probability density $p(x|m)$, for example maximum a posteriori estimate $x_{\rm MAP}$ or conditional mean estimate $x_{\rm CM}$ defined by

$$p(x_{\rm MAP}|m) = \max p(x|m), \qquad x_{\rm CM} = \int_{\mathbb{R}^M} xp(x|m)\,dx,$$

respectively. The Bayesian reconstructions are better than tomosynthetic images discussed at the time in journals of dental radiology. The visible edges are those predicted by the microlocal analysis of T. Quinto [10].

However, it was found that the Bayesian use of total variation priors is problematic at the high resolution limit [7]. The total variation prior is not *discretization-invariant*, resulting in incompatible convergence of $x_{\rm MAP}$ and $x_{\rm CM}$ when the computational grid is refined. So we started looking for alternative approaches for edge-preserving Bayesian tomography. One technique we introduced is a modified level set method producing nicely localised reconstructions [3], see Figure 1.

In [12] we prove that Besov space priors are discretization-invariant. Moreover, they can be effectively implemented using wavelets, and the space $B^1_{1,1}$ is especially promising for edge-preserving reconstruction algorithms. Numerical results using Besov space priors are reported in [11, 9, 14]; we highlight here the approach using finer scale wavelet functions only in the local tomography region of interest. Namely, our numerical results using $B^{1/2}_{3/2,3/2}$ space prior in [9] compare favorably to Λ-tomography [2], see Figure 2.

In the future we will study dynamic 3D X-ray imaging using a set of X-ray sources and corresponding detectors arranged in fixed positions around the region of interest. The detectors must be capable of recording several images per second (frame rates up to 200 are commercially available at the time of writing). Our previous studies have shown that one can achieve useful reconstructions from data collected from very few (~ 10) angles of view, so with the above set-up we can produce a three-dimensional reconstruction at every instant of time when data was recorded. This kind of imaging is useful for many applications, including cardiac imaging with high enough frame-rate and no need for gating, dynamic angiography following the blood flow accurately in time, removing patient movement artifacts in dental imaging, and small animal imaging allowing the target to move.

Acknowledgements. This research was supported by GE Healthcare Finland, PaloDEx Group, Finnish Technology Agency (TEKES projects 2844/31/02 and 1107/401/00) and the Academy of Finland (Centre of Excellence project 213476).

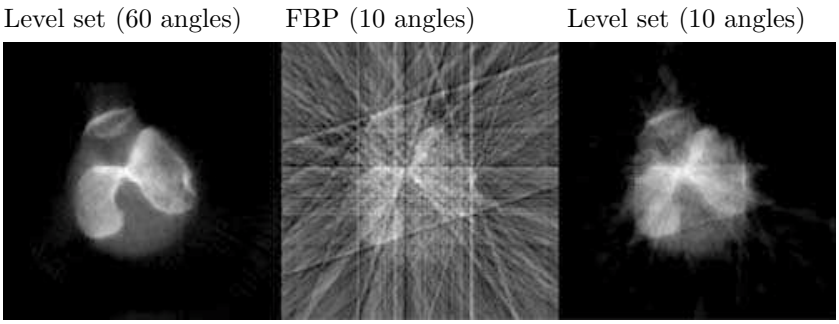

FIGURE 1. Level set reconstruction of a knee specimen. The data was collected using a surgical C-arm X-ray device. Left: level set reconstruction from 60 fan-beam projections covering full angle of view. This image is considered as the ground truth in comparison to reconstructions from sparse data. Middle: the result of applying filtered back-projection to 10 fan-beam projections from full angle. Right: level set reconstruction from the same data than in the middle image. See [3] for more details.

REFERENCES

[1] A. Cederlund, M. Kalke and U. Welander, *Volumetric tomography — a new tomographic technique for panoramic units*, Dentomaxillofac. Radiol., **38** (2009), 104–111.

[2] Faridani A, Ritman E L, and Smith K T 1992 Local tomography. *SIAM J. Appl. Math.* **52**(2) 459–84; Examples of local tomography **52**(4) 1193–1198 (A reorganization of the examples which became disorganized while the article was in press.)

[3] V. Kolehmainen, M. Lassas and S. Siltanen, *Limited data X-ray tomography using nonlinear evolution equations*, SIAM Journal of Scientific Computation, **30** (2008), 1413–1429.

Λ-tomography Wavelet-based Bayesian inversion

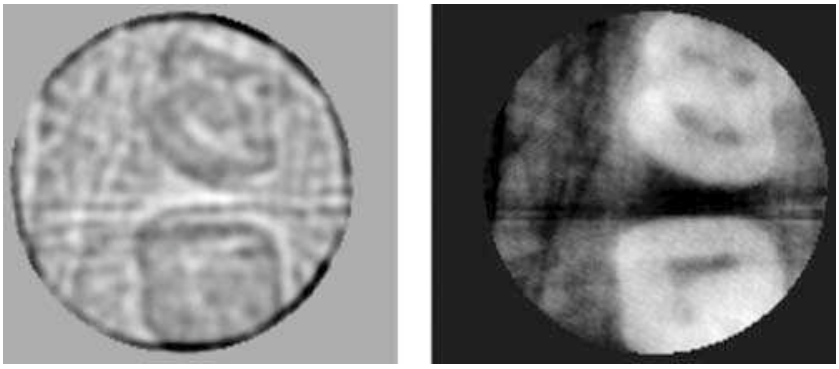

FIGURE 2. Reconstruction of a region of interest inside a dry human mandible. Left: local reconstruction using Λ-tomography. Right: local reconstruction using wavelet-based Bayesian inversion with a Besov space prior. See [9] for more details.

[4] V. Kolehmainen, S. Siltanen, S. Järvenpää, J. P. Kaipio, P. Koistinen, M. Lassas, J. Pirttilä and E. Somersalo, *Statistical inversion for medical x-ray tomography with few radiographs: II. Application to dental radiology*, Phys. Med. Biol., **48** (2003), 1465–1490.

[5] V. Kolehmainen, A. Vanne, S. Siltanen, S. Järvenpää, J. P. Kaipio, M. Lassas and M. Kalke, *Parallelized Bayesian inversion for three-dimensional dental X-ray imaging*, IEEE Transactions on Medical Imaging, **25** (2006), 218–228.

[6] V. Kolehmainen, A. Vanne, S. Siltanen, S. Järvenpää, J. P. Kaipio, M. Lassas and M. Kalke, *Bayesian inversion method for 3D dental X-ray imaging*, Elektrotechnik & Informationstechnik, **124** (2007), 248–253.

[7] Lassas M and Siltanen S 2004, Can one use total variation prior for edge-preserving Bayesian inversion? Inverse Problems 20, pp. 1537-1563.

[8] F. Natterer, "The Mathematics of Computerized Tomography", Wiley & Sons, Chichester, 1986.

[9] K. Niinimäki, S. Siltanen and V. Kolehmainen, *Bayesian multiresolution method for local tomography in dental X-ray imaging*, Physics in Medicine and Biology, **52** (2007), 6663–6678.

[10] E. T. Quinto, *Singularities of the X-Ray Transform and Limited Data Tomography in* $\mathbb{R}^2$ *and* $\mathbb{R}^3$, SIAM J. Math. Anal., **24** (1993), 1215–1225.

[11] M. Rantala, S. Vänskä, S. Järvenpää, M. Kalke, M. Lassas, J. Moberg and S. Siltanen, *Wavelet-based reconstruction for limited angle X-ray tomography,* IEEE Transactions on Medical Imaging **25** (2006), 210–217.

[12] Lassas M, Saksman E and Siltanen S 2009, Discretization invariant Bayesian inversion and Besov space priors. Inverse Problems and Imaging 3(1), pp. 87-122.

[13] S. Siltanen, V. Kolehmainen, S. Järvenpää, J. P. Kaipio, J. Koistinen, M. Lassas, J. Pirttilä and E. Somersalo, *Statistical inversion for medical x-ray tomography with few radiographs: I. General theory*, Phys. Med. Biol., **48** (2003), 1437–1463.

[14] S. Vänskä, M. Lassas and S. Siltanen, *Statistical X-ray tomography using empirical Besov priors*, International Journal of Tomography & Statistics, **11** (2009), 3–32.

Structural inversion with level sets for microwave breast imaging

Oliver Dorn
(joint work with Natalia Irishina, Diego Álvarez and Miguel Moscoso)

Microwave imaging for breast screening is a promising new technology for the early detection of breast cancer. The breast is illuminated by electromagnetic waves in the range of 0.5 to 5 GHz, and the response of the breast tissue to this illumination is measured in surrounding microwave antennas. The goal is to detect any hidden small anomalies in the breast, and to characterize them as either benign or malignant.

Mathematically this problem amounts to an inverse problem for Maxwell's equations, or in its 2D form using a TM-wave geometry, to an inverse problem of the 2D Helmholtz equation.

Since the mathematical inverse problem is ill-posed, some form of regularization needs to be applied when processing the collected data for forming an image representing the breast. A standard approach would be to do a classical pixel-based inversion, applying for example Tikhonov Philips regularization, and then identify and characterize any small anomalies in the reconstructed image. However, with this technique typically small tumors of a certain contrast to the healthy background are represented in the reconstruction as smeared-out anomalies with a significantly smaller contrast, which makes it difficult to detect these small anomalies, or if detected, to characterize them as benign or malignant.

In the talk we present a novel level set based approach for tumor detection and characterization from microwave data [1]. The breast is assumed to be composed of four different tissue types, namely skin, fatty tissue, fibroglandular tissue and a possible tumor. These different regions are separated by sharp interfaces, modelled by a level set technique. Since more than two regions need to be described in this application, a generalization of the standard level set technique is employed, a so-called colour level set technique. Moreover, in order to address some very specific characteristics of our reconstruction algorithm, a variant of this colour level set technique is proposed which uses three different level set functions for representing four different regions (tissue types) in the breast.

Since also the possibly inhomogeneous interior profiles in each region are unknown a priori, a simultaneous evolution of four different profile functions and of three different level set functions is constructed which points into a descent direction of the data least squares cost. The result of this structural evolution is the final image which directly shows the tumor candidate(s), an estimate of their contrast to the background, and the different region interfaces and profiles in the breast. Numerical experiments in 2D are presented which demonstrate the performance of this novel technique for realistic situations of breast screening.

References

[1] N. Irishina, D. Álvarez, O. Dorn and M. Moscoso, *Structural level set inversion for microwave breast screening*, Inverse Problems **26** (2010), 035015.

Motion Correction on 3D Positron Emission Tomographic Data

Mohammad Dawood

1. Introduction

PET (Positron Emission Tomography) is one method of acquiring metabolic information in patient studies, e.g. to visualize and quantify glucose metabolism in the body. To achieve this, a radioactive substance is injected in the patient body prior to image acquisition. The radioactive isotope decays with time and emits radiation which can be detected in specially built scanners. The distribution of the radioactivity in the body can thus be visualized and gives information on the metabolism. In PET, β^+ radioactive molecules are used for this purpose. These molecules emit positrons which collide with electrons and produce two gamma quanta which fly away from each other in opposite directions. The gamma quanta can now be detected in the scintillation detectors of the PET scanner. Using specialized reconstruction methods the activity distribution can thus be reconstructed [7].

As this process of image acquisition requires a relatively long period of time, typically several minutes, the motion of the heart due to respiration and due to the cardiac contraction blurs the images. Image blur may cause wrong staging, inaccurate localization and wrong quantification of lesions. Thus PET studies have to take this into account.

This problem is compounded further if computed tomography (CT) data is used for attenuation correction, as in the case of modern PET/CT scanners. The CT data represents a snapshot in comparison to the PET images and therefore, the PET data is not always in spatial correspondence with the CT data.

One method of avoiding this problem is to use respiratory and cardiac signals from the patient to divide the PET data into phases with respect to either or both signals[3]. This is called gating. Different methods of gating are known [5]. However, gating always leads to reduction of the amount of information per phase and thus to a lesser signal to noise ratio.

2. Optical Flow

2.1. **Brightness Consistency Based Optical Flow.** Optical flow methods estimate the motion between two image frames. As a voxel with intensity $I(x, y, z, t)$ moves between the two frames, its intensity is assumed to remain constant. Assuming the movement to be small enough and with Taylor expansion we get:

$$\begin{aligned} I_x u + I_y v + I_z w &= -I_t \text{ or} \\ \nabla I \cdot \mathbf{u} &= -I_t \end{aligned}$$

with u, v, w for the x,y and z components of the velocity or optical flow $\mathbf{u}$, and I_x,I_y,I_z,I_t for the derivatives of the intensity image I in corresponding directions, respectively time.

To find the optical flow from this equation with three unknowns, smoothness in flow is used as additional condition. The optical flow is found by minimizing an energy functional whihc is given as:

$$f = \min \int ((\nabla I \cdot \mathbf{u} + I_t)^2 + \alpha(|\nabla u|^2 + |\nabla v|^2 + |\nabla w|^2))\mathrm{d}x\mathrm{d}y\mathrm{d}z$$

where larger values of α lead to a smoother flow. The minimization can be achieved by calculating the corresponding Euler-Lagrange equations.

Such methods have been applied to the problem of respiratory motion on 3D PET/CT data successfully [2].

2.2. **Mass Conservation Based Optical Flow.** The optical flow estimation presented in the previous section is applicable to data where the intensity of the objects remains constant. However, in some cases this constraint does not hold true. Cardiac PET studies are one such example.

The here presented method is based upon the continuity equation, more precisely upon the conservation of mass. This law can be written as:

$$\frac{\partial I}{\partial t} + div(I\mathbf{u}) = 0$$

Deviations from this eqution can be penalized by the following functional:

$$\int_V (\nabla I \cdot \mathbf{u} + I_t + I div(\mathbf{u}))^2 dV$$

This is again an under-determined system and therefore a smoothing term can be added to solve it. The resulting optical flow functional is thus:

$$f \quad = \quad \mathrm{argmin}\left[\int_V (div(I\mathbf{u}) + I_t)^2 dV + \alpha \int_V (|\nabla u|^2 + |\nabla v|^2 + |\nabla w|^2) dV\right]$$

References

[1] A Bruhn, J Weickert, and C Schnörr. *Lucas/Kanade meets Horn/Schunck: Combining local and global optic flow methods*, International Journal of Computer Vision, **61** (2005), 211–231.

[2] M Dawood, N Lang, X Jiang, and KP Schäfers. *Lung motion correction on respiratory gated 3-D PET/CT images*, IEEE Trans Med Imaging, **25** (2006), 476–485.

[3] M Dawood, F Büther, N Lang, O Schober, and KP Schäfers. *Respiratory gating in positron emission tomography: A quantitative comparision of different gating schemes*, Medical Physics, **34** (2007), 3067–3076.

[4] M Dawood, F Büther, X Jiang, and KP Schäfers. *Respiratory Motion Correction in 3D PET Data with Advanced Optical Flow Algorithms*, IEEE Trans Med Imaging, **27** (2008), 1164-75.

[5] M Dawood, F Bther, L Stegger, X Jiang, O Schober, M Schfers, KP Schfers. *Optimal number of respiratory gates in positron emission tomography: A cardiac patient study*, Med Phys, **36**, (2009), 1775-1784.

[6] B Horn, and B Schunck. *Determining optical flow*, Artificial Intelligence, **17** (1981), 185–203.

[7] S Vandenberghe, Y D'Asseler, R Van de Walle, T Kauppinen, M Koole, L Bouwens, K Van Laere, I Lemahieu, and RA Dierckx. *Iterative reconstruction algorithms in nuclear medicine*, Comput Med Imaging Graph, **25** (2001), 105–111.

Accurate image reconstruction involving all redundant data in helical cone-beam CT

Frederic Noo
(joint work with Harald Schöndube)

We discuss the problem of performing an accurate reconstruction in helical cone-beam (CB) tomography while making efficacious use of all measured data. Efficient theoretically-exact and stable formulas have been suggested for helical CB imaging in the last decade, but none can handle the redundant data obtained with the arbitrary helix pitch that is commonly used. We first review an algorithm that we recently published that can handle redundant data at maximum pitch. Then, we extend this algorithm to arbitrary pitch, by showing how the issue of interrupted illumination that appears in this case can be solved. Encouraging preliminary results are shown, highlighting the need for further work on the selection of the weights involved in the data combination procedure of the method.

Electron Microscope Tomography over Curves

Eric Todd Quinto
(joint work with Hans Rullgård)

We define a general curvilinear Radon transform in $\mathbb{R}^3$, and we develop the microlocal properties of this transform. There are no inversion formulas for this transform, in general, and we give a local reconstruction method that recovers singularities of the object that are stably visible from the data. This is a type of regularization since we do not recover the function itself but singularities of the function that are stably reconstructed in a Sobolev sense. Our method is motivated by Lambda tomography, and it is a filtered back projection algorithm with a derivative filter. We characterize the singularities this algorithm reconstructs, and we show that some singularities are added to the reconstruction. Added singularities are inherent in any standard backprojection algorithm for this problem by the nature of the backprojection. Using our characterization of added singularities, we choose a derivative filter that will de-emphasize some of the added singularities. These results, their proofs, and reconstructions will appear in [3].

In *single object electron tomography (ET)*, images are taken of a single object over a finite number of rotations (called tilts) of the object in the electron beam. The standard model for single object ET assumes that electrons travel over lines and that the electron count at the detector is affected by the electrostatic potential f of the object. A more complete model will include the optics of the electron microscope, and information about the complete model is given in [1], as discussed in the talk of H. Kohr at this conference.

The theoretical work we describe here is motivated by practical work of Albert Lawrence, *et al.*, that shows when imaging larger objects using broader electron beams, the electrons farther from the center beam travel in helix-like curves. They

have developed a reconstruction algorithm, TxBR [2], that uses gold markers in the projections to find the curves that the electrons travel over.

We now describe our general microlocal theory of a curvilinear Radon transform in $\mathbb{R}^3$. For each $\theta \in]a,b[$ (representing a tilt angle) and each $\boldsymbol{y} \in \mathbb{R}^2$ (representing a point on the detector plane for tilt θ), a smooth projection $\boldsymbol{p}_\theta : \mathbb{R}^3 \to \mathbb{R}^2$ defines the curves, which are given for $(\theta, \boldsymbol{y}) \in Y =]a,b[\times \mathbb{R}^2$ by

$$\gamma_{\theta,\boldsymbol{y}} := {\boldsymbol{p}_\theta}^{-1}(\{\boldsymbol{y}\}).$$

The *Curvilinear X-ray Transform* is given by

$$\mathcal{P}_{\boldsymbol{p}} f(\theta, \boldsymbol{y}) := \int_{\boldsymbol{x} \in \gamma_{\theta,\boldsymbol{y}}} f(x) ds.$$

The *backprojection operator* is given by

$$\mathcal{P}^*_{\boldsymbol{p}} g(\boldsymbol{x}) := \int_{\theta \in]a,b[} \varphi(\theta) g\left(\theta, \boldsymbol{p}_\theta(\boldsymbol{x})\right) d\theta$$

where φ is a cutoff function on $]a,b[$ that is equal to one on most of $]a,b[$ and is in $C_c^\infty(\,]a,b[\,)$. Since $\boldsymbol{x} \in \gamma_{\theta,\boldsymbol{p}_\theta(\boldsymbol{x})}$, $\mathcal{P}^*_{\boldsymbol{p}} g(\boldsymbol{x})$ is just an integral of g over all curves through $\boldsymbol{x}$.

Finally, our *singularity detection operator* is

$$\mathcal{L}(f) := \mathcal{P}^*_{\boldsymbol{p}} D \mathcal{P}_{\boldsymbol{p}} f$$

where D is a second order differential operator in $\boldsymbol{y}$ that is chosen to de-emphasize certain added singularities that we will describe below.

Clearly some conditions on the curves are necessary, and we will now describe our conditions and what they mean geometrically. We will let ∂_θ be the derivative in the theta direction, and $\partial_{\boldsymbol{x}}$ will be the gradient in $\boldsymbol{x}$.

(1) *For each $\theta \in]a,b[$, the curves $\gamma_{\theta,\boldsymbol{y}}$ are smooth, unbounded, and don't intersect.* Precisely, we assume that $(\boldsymbol{x}, \theta) \mapsto \boldsymbol{p}_\theta(\boldsymbol{x}) \in \mathbb{R}^2$ is a C^∞ map. Fixing θ, $\boldsymbol{p}_\theta$ is a fiber map in $\boldsymbol{x}$ with fibers diffeomorphic to lines. This assumption will imply that $\partial_{\boldsymbol{x}} \boldsymbol{p}_\theta(\boldsymbol{x})$ has maximal rank (two).

(2) *The curves $\gamma_{\theta,\boldsymbol{y}}$ are different for different $(\theta, \boldsymbol{y}) \in Y$.*

(3) *Curves move differently at different points as θ changes.* The precise assumption is that for all $(\theta, \boldsymbol{y}) \in Y$ and for any two distinct points $\boldsymbol{x}_0$ and $\boldsymbol{x}_1$ in $\gamma_{\theta,\boldsymbol{y}}$, the derivatives $\partial_\theta \boldsymbol{p}_\theta(\boldsymbol{x_0})$ and $\partial_\theta \boldsymbol{p}_\theta(\boldsymbol{x}_1)$ are not equal.

(4) *The curves wiggle enough as θ changes.* Precisely, The 4×3 matrix $\begin{pmatrix} \partial_{\boldsymbol{x}} \boldsymbol{p}_\theta(\boldsymbol{x}) \\ \partial_\theta \partial_{\boldsymbol{x}} \boldsymbol{p}_\theta(\boldsymbol{x}) \end{pmatrix}$ has maximal rank (three). One can show this means that the normal plane to $\gamma_{\theta,\boldsymbol{y}}$ at $\boldsymbol{x} \in \gamma_{\theta,\boldsymbol{y}}$ changes as θ changes infinitesimally.

We now understand in an elementary way how our algorithm detects singularities. Let $\boldsymbol{x} \in \mathbb{R}^3$. Note that for each $\theta \in]a,b[$, $\boldsymbol{x} \in \gamma_{\theta,\boldsymbol{p}_\theta(\boldsymbol{x})}$. Therefore, the union of all curves in Y through $\boldsymbol{x}$ is

$$\Sigma_{\boldsymbol{x}} := \bigcup_{\theta \in]a,b[} \gamma_{\theta,\boldsymbol{p}_\theta(\boldsymbol{x})}$$

By assumption (3), $\Sigma_{\boldsymbol{x}}$ is smooth immersed surface except at $\boldsymbol{x}$, where it comes to a point [3].

For $\boldsymbol{x} \in \mathbb{R}^3$ and f a function of compact support $\mathcal{P}_{\boldsymbol{p}}^*\mathcal{P}_{\boldsymbol{p}}f(\boldsymbol{x})$ first integrates f over each curve through $\boldsymbol{x}$ and then averages over the curves through $\boldsymbol{x}$. Therefore,

$$\mathcal{P}_{\boldsymbol{p}}^*\mathcal{P}_{\boldsymbol{p}}f(\boldsymbol{x}) = \int_{\boldsymbol{z}\in\Sigma_{\boldsymbol{x}}} f(\boldsymbol{z})\, W(\boldsymbol{z},\boldsymbol{x})\, dA$$

where $W(\boldsymbol{z},\boldsymbol{x})$ is a smooth weight on $\Sigma_{\boldsymbol{x}} \setminus \{\boldsymbol{x}\}$. So, $\mathcal{P}_{\boldsymbol{p}}^*\mathcal{P}_{\boldsymbol{p}}f(\boldsymbol{x})$ is an integral of f over the surface $\Sigma_{\boldsymbol{x}}$. Since $\mathcal{L}$ is essentially $\mathcal{P}_{\boldsymbol{p}}^*\mathcal{P}_{\boldsymbol{p}}$ with a differential operator in the middle, $\mathcal{L}f$ detects singularities in essentially the same way as $\mathcal{P}_{\boldsymbol{p}}^*\mathcal{P}_{\boldsymbol{p}}$.

We use this idea to explain intuitively how $\mathcal{L}$ detects singularities. Let $\boldsymbol{x_0} \in \mathbb{R}^3$. If a singularity of f at $\boldsymbol{x_0}$ is conormal to some curve $\gamma_{\theta,\boldsymbol{p_\theta}(\boldsymbol{x})}$ then it should be detected by $\mathcal{P}_{\boldsymbol{p}}f$ [3]. To see this, let's do a thought experiment in which f is a characteristic function of a ball, B, and $\gamma_{\theta,\boldsymbol{p_\theta}(\boldsymbol{x_0})}$ is tangent to the ball at $\boldsymbol{x_0}$. Then, $\mathcal{P}_{\boldsymbol{p}}f$ will not be smooth near $(\theta, \boldsymbol{p}_\theta(\boldsymbol{x_0}))$ since $\mathcal{P}_{\boldsymbol{p}}f$ will go from 0 to nonzero as the curve moves in and out of the ball. Such singularities (which are called "visible") will be detected by $\mathcal{L}$ (see [3] for a precise statement).

However, singularities from far away on $\Sigma_{\boldsymbol{x}_0}$ can also affect the reconstruction at $\boldsymbol{x_0}$. Imagine that $\Sigma_{\boldsymbol{x}_0}$ is tangent to the support of f, B at a point besides $\boldsymbol{x_0}$. Then, the integral $\mathcal{P}_{\boldsymbol{p}}^*\mathcal{P}_{\boldsymbol{p}}f$ will not be smooth at $\boldsymbol{x_0}$ since it will go from being zero to nonzero in a non-smooth way as $\boldsymbol{x}$ moves so that $\Sigma_{\boldsymbol{x}}$ moves in and out of the ball B. This adds singularities to the reconstruction at $\boldsymbol{x_0}$.

Precisely, in [3], we prove that $\mathcal{P}_{\boldsymbol{p}}$ is a Fourier integral operator associated with Lagrangian manifold $\Gamma = N^*Z \setminus 0$ where Z is the *incidence relation*

$$Z := \{(\theta, \boldsymbol{y}, \boldsymbol{x}) \in Y \times \mathbb{R}^3 \,\big|\, \boldsymbol{x} \in \gamma_{\theta,\boldsymbol{y}}\}$$

and N^*Z is its conormal bundle. Then $\mathcal{L}$ is a singular operator associated to the canonical relation $\Gamma^t \circ \Gamma$ and this relation above $\boldsymbol{x_0}$ is basically the visible directions (those conormal to curves through $\boldsymbol{x_0}$) $\times\, N^*(\Sigma_{\boldsymbol{x}_0}) \setminus 0$. So, singularities of f conormal at $\boldsymbol{x_0}$ to curves in the data set (visible singularities) will be detected by $\mathcal{L}f$ at $\boldsymbol{x_0}$, and singularities conormal to $\Sigma_{\boldsymbol{x}_0}$ at other points will be *added* to the reconstruction at $\boldsymbol{x_0}$. This is illustrated by our thought experiments above and is proven in [3].

In [3], we use our microlocal characterization of the added singularities to choose a differential operator D for $\mathcal{L}$ that will de-emphasize added singularities that are near to the reconstruction, and we show the algorithm works well to de-emphasize the added singularities.

Acknowledgements: The speaker thanks the Mathematisches Institut Oberwolfach for its great hospitality both during the conference and afterwards, as he waited for a flight home as an Icelandic volcano spewed ash over Europe. The MFO provided invaluable hospitality to several stranded foreigners during this time, and we are all grateful for their generosity.

This material is based upon work supported by the National Science Foundation under Grant No. 0908015. The speaker is also supported by the Tufts University FRAC, and the Wenner Gren Stiftelserna.

References

[1] D. Fanelli and O. Öktem. Electron tomography: A short overview with an emphasis on the absorption potential model for the forward problem. *Inverse Problems*, 24(1):013001, 2008.

[2] S. Phan, J. Bouwer, J. Lanman, M. Terada, and A. Lawrence. Non-Linear Bundle Adjustment for Electron Tomography. In *Proceedings CSIE09, March 31-April 1, 2009, Los Angeles, IEEE Computer Society*, 2009. to appear.

[3] E.T. Quinto and H. Rullgård, Local Singularity Reconstruction from Integrals over Curves in $\mathbb{R}^3$. preprint, 2010.

Reporter: Jahn Müller

Participants

Prof. Dr. Gaik Ambartsoumian
Department of Mathematics
University of Texas at Arlington
P. O. Box 19408
Arlington , TX 76019-0408
USA

Prof. Dr. Guillaume Bal
Department of Applied Physics and
Applied Mathematics
Columbia University
New York , NY 10027
USA

Prof. Dr. Jan Boman
Department of Mathematics
Stockholm University
S-10691 Stockholm

Prof. Dr. Martin Burger
Institut für Numerische und
Angewandte Mathematik
Universität Münster
Einsteinstr. 62
48149 Münster

Prof. Dr. Rolf Clackdoyle
Lab. Hubert Curien
CNRS UMR 5516
Campus Pole Opt. et Vision-Bat. F
18, rue Prof. Benoit Lauras
F-42000 St. Etienne

Dr. Mohammad Dawood
European Institute for Molecular
Imaging
Mendelstr. 11
48149 Münster

Prof. Dr. Laurent Desbat
TIMC - IMAG
Grenoble University
Faculte de Medicine
F-38706 La Tronche Cedex

Dr. Oliver Dorn
School of Mathematics
The University of Manchester
Oxford Road
GB-Manchester M13 9PL

Prof. Dr. Bernd Fischer
Institut für Mathematik
Universität zu Lübeck
Wallstr. 40
23560 Lübeck

Bernadette Hahn
FR 6.1 - Mathematik
Universität des Saarlandes
Postfach 15 11 50
66041 Saarbrücken

Prof. Dr. Martin Hanke-Bourgeois
Fachbereich Mathematik/Informatik
Johannes-Gutenberg-Universität
55099 Mainz

Prof. Dr. Bastian von Harrach
Fakultät für Mathematik
Technische Universität München
Boltzmannstr. 3
85748 Garching bei München

Prof. Dr. Maarten de Hoop
Department of Mathematics
Purdue University
West Lafayette , IN 47907-1395
USA

Prof. Dr. Ming Jiang
School of Mathematical Sciences
Peking University
Beijing 100871
P.R. CHINA

Dr. Ivana Jovanovic
EPFL
School of Computer & Communication Sc.
Station 14
CH-1015 Lausanne

Prof. Dr. Barbara Kaltenbacher
Institut für Mathematik
Karl-Franzens-Universität Graz
Heinrichstr. 36
A-8010 Graz

Prof. Dr. Alexander Katsevich
Department of Mathematics
University of Central Florida
Orlando , FL 32816-1364
USA

Dr. Esther Klann
Johann Radon Institute for Comput. and Applied Mathematics (RICAM)
Austrian Academy of Sciences
Altenbergerstr. 69
A-4040 Linz

Dipl. Math. Holger Kohr
Institut für Angewandte Mathematik
Universität des Saarlandes
Postfach 151150
66041 Saarbrücken

Prof. Dr. Leonid Kunyansky
Department of Mathematics
University of Arizona
617 N. Santa Rita
Tucson AZ 85721-0089
USA

Dr. Aref Lakhal
Institut für Angewandte Mathematik
Universität des Saarlandes
Postfach 151150
66041 Saarbrücken

Prof. Dr. Dirk Lorenz
Institut für Algebra u. Analysis
TU Braunschweig
38092 Braunschweig

Prof. Dr. Alfred K. Louis
FR 6.1 - Mathematik
Universität des Saarlandes
Postfach 15 11 50
66041 Saarbrücken

Prof. Dr. Peter Maaß
Universität Bremen
FB 3 Mathematik & Informatik
28344 Bremen

Prof. Dr. Bernard A. Mair
Department of Mathematics
University of Florida
358 Little Hall
P.O.Box 118105
Gainesville , FL 32611-8105
USA

Prof. Dr. Joyce R. McLaughlin
Dept. of Mathematical Sciences
Rensselaer Polytechnic Institute
110 8th Street
Troy NY 12180-3590
USA

Jahn Müller
Institut für Numerische und Angewandte Mathematik
Universität Münster
Einsteinstr. 62
48149 Münster

Prof. Dr. Dr.h.c. Frank Natterer
Institut für Numerische und
Angewandte Mathematik
Universität Münster
Einsteinstr. 62
48149 Münster

Linh Nguyen
Department of Mathematics
Texas A & M University
College Station , TX 77843-3368
USA

Prof. Dr. Frederic Noo
CAMT
729 Arapeen Drive
Salt Lake City , UT 84108-1218
USA

Steven Oeckl
Fraunhofer Institut IIS
Projektgruppe Ultrafeinfokus
Röntgentechnologie
Dr.-Mack-Str. 81
90762 Fürth

Prof. Dr. Victor P. Palamodov
School of Mathematical Sciences
Tel Aviv University
Ramat Aviv
Tel Aviv 69978
ISRAEL

Prof. Dr. Eric Todd Quinto
Department of Mathematics
Tufts University
503 Boston Ave.
Medford , MA 02155
USA

Prof. Dr. Ronny Ramlau
Johann Radon Institute for Comput.
and Applied Mathematics (RICAM)
Austrian Academy of Sciences
Altenbergerstr. 69
A-4040 Linz

Prof. Dr. Andreas Rieder
Karlsruher Institut f. Technologie (KIT)
Inst. f. Angew. & Numerische Mathematik
76128 Karlsruhe

Prof. Dr. Wolfgang Ring
Institut für Mathematik
Karl-Franzens-Universität Graz
Heinrichstr. 36
A-8010 Graz

Martin Riplinger
FR 6.1 - Mathematik
Universität des Saarlandes
Postfach 15 11 50
66041 Saarbrücken

Prof. Dr. Pierre C. Sabatier
Laboratoire de Physique Theorique
and Astroparticules
Universite de Montpellier II
Pl. E. Bataillon - Case 70
F-34095 Montpellier Cedex 05

Prof. Dr. Otmar Scherzer
Computational Science Center
Universität Wien
Nordbergstr. 15
A-1090 Wien

Prof. Dr. John C. Schotland
Department of Bioengineering
University of Pennsylvania
Philadelphia , PA 19104
USA

Prof. Dr. Thomas Schuster
Fakultät für Maschinenbau
Helmut-Schmidt-Universität
Holstenhofweg 85
22043 Hamburg

Prof. Dr. Samuli Siltanen
Dept. of Mathematics & Statistics
University of Helsinki
P.O.Box 68
FIN-00014 University of Helsinki

Malte Spiess
Fakultät für Mathematik und
Wirtschaftswissenschaften
Universität Ulm
Helmholtzstr. 18
89081 Ulm

Prof. Dr. Evgeny Spodarev
Institut für Stochastik
Universität Ulm
Helmholtzstr. 18
89081 Ulm

Dennis Trede
Zentrum für Technomathematik
FB 3, Universität Bremen
Postfach 330 440
28334 Bremen

Dr. Frank Wübbeling
Institut für Numerische und
Angewandte Mathematik
Universität Münster
Einsteinstr. 62
48149 Münster